ORGANIC LIGHT-EMITTING DIODES AND RELATED HYBRID LIGHT-EMITTING DEVICES

By

DONG WOO SONG

A DISSERTATION PRESENTED TO THE GRADUATE SCHOOL
OF THE UNIVERSITY OF FLORIDA IN PARTIAL FULFILLMENT
OF THE REQUIREMENTS FOR THE DEGREE OF
DOCTOR OF PHILOSOPHY

UNIVERSITY OF FLORIDA

2011

© 2011 Dong Woo Song

To my family

ACKNOWLEDGMENTS

First of all, I would like to appreciate my advisor, Dr. Franky So for guiding me during full period of my Ph.D. cource. His plenty of advices have stimulated me to widen my sight, especially for industrial perspective. I am also thankful to Dr. Jiangeng Xue, Dr. Stephen Pearton, Dr. David Norton, Dr. Brent Gila and Dr. Andrew Rinzler for agreeing to serve on my supervisory committee and/or for sharing their time.

I thank my colleagues in Dr. So's group: Kaushik Roy Chouhury, Jiyon Song, Subbiah Jegadesan, Chi Hang Cheung, Lei Qian, Wonhoe Koo, Sai-Wing Tsang, Jaewon Lee, Neetu Chopra, Galileo Sarasqueta, Jong Hyuk Yoon, Alok Gupta, Cephas Small, Michael Hartel, Song Chen, Pieter de Somer, Verena Giese, Jae Woong Lee, Wooram Youn, Chaoyu Xiang, Jesse Manders, Fred Steffy, Nikhil Bhandari, Francisco Delgado, Tzung-Han Lai, Chieh-Chun Chaing, Shuyi Liu and Jiho Ryu. I would like to express my special thanks to Do Young Kim as not only a colleague but also a mentor during my obscure Ph.D. course.

I acknowledge the contribution of the following colleagues on my research works: Wooram Youn, Chaoyu Xiang and Cephas Small for OLED works, Kaushik Roy Choudhury for hybrid NIR-LED works, and Do Young Kim, Kaushik Roy Choudhury, Jae Woong Lee, Galileo Sarasqueta for up-conversion device works.

I also acknowledge the financial support of Department of Energy Solid State Lighting program, Defense Advanced Research Projects Agency Extreme Light Sources program and Nanoholdings for my research activities.

I also thank my Korean friends in MSE: Sanghyun Eom, Kangtaek Lee, Byungwook Lee, Sangjoon Lee, Jinwoo Kwak, Sungwon Choi, Hyoungjun Park, Jaeseok Lee, Seungyong Son, Wantae Lim, Junghoon Jang, Chanwoo Lee, Dongjo Oh,

Myounghwan Oh, Donghyun Kim, Jihoon Choi, Minki Hong, Jungbae Lee, Sungwook Min, Jinhyung Lee, Seunghwan Yeo, Chinsung Park, Hyuksoo Han and Kwangwon Lee. I would like to express my special thanks to Seonhoo Kim, Kyeongwon Kim and Inkook Jun with sincere friendship for long years.

I appreciate Korean Buddhist Association members for sharing in religious view and leisure time: Sooyeon Kim, Chunghwan Sung, Youngjae Song, Sangeun Oh, Hyeongjeen Jeen, Yoojung Park, Yoonjung Lim, Jaejin Lee and Kyungpyo Hong.

I would like to express my best gratitude and love to my family. My parents have supported me physically and spiritually. They lead me to walk on the right path during my whole life. My sister has taken the lead of me as a scientist and a mentor as well, and thus I started to be a scientist. I truly appreciate my parents-in-law for giving me a great deal of support and sincere cheers. I am genuinely grateful to my lovely wife, Sora Lee. After I met her, my life was changed and filled with joy and love. I would like to express my love to my baby son, Yoohyun Henry Song.

No one can live alone. I get indebted by *the Fourfold Grace of Heaven and Earth, Parents, Fellow Beings and Laws* and I shall enshrine *Il-Won-Sang* as my object of faith and my model of practice.

TABLE OF CONTENTS

page

ACKNOWLEDGMENTS 4

LIST OF TABLES 9

LIST OF FIGURES 10

LIST OF ABBREVIATIONS 14

ABSTRACT 16

CHAPTER

1 INTRODUCTION 18

1.1 Organic Light-Emitting Diodes 18
1.1.1 Advantages and Disadvantages of Organic Materials 18
1.1.2 Applications of OLEDs 19
1.1.2.1 Display applications 20
1.1.2.2 Lighting applications 21
1.1.3 Basic Concepts for OLED Lighting 22
1.1.3.1 Basics in colorimetry 22
1.1.3.2 Basics in device measurements 25
1.1.4 Physics in Organic Light-Emitting Diodes 26
1.1.4.1 Electronic structures 26
1.1.4.2 Charge transport 27
1.1.4.3 Excitons and intermolecular exciton energy transfer 28
1.1.4.4 Fluorescence and phosphorescence 29
1.2 Colloidal Quantum Dot-Based Hybrid Light-Emitting Diodes 30
1.2.1 State of the Art Hybrid LEDs 30
1.2.1.1 Visible-emitting hybrid LEDs 30
1.2.1.2 Infrared-emitting hybrid LEDs 32
1.2.2 Colloidal Quantum Dots 33
1.2.2.1 Synthesis of colloidal quantum dots 33
1.2.2.2 Optical properties of colloidal quantum dots 34
1.3 Organic and Hybrid Photodetectors and Organic Up-Conversion Devices 34
1.3.1 Visible Organic Photodetectors 34
1.3.2 Infrared Organic Photodetectors 35
1.3.3 Colloidal Quantum Dot Based Hybrid Photodetectors 36
1.3.4 Organic Up-Conversion Devices 38
1.4 Dissertation Organization 39

2 WHITE PHOSPHORESCENT ORGANIC LIGHT-EMITTING DIODES 47

2.1 Background and Motivation 47

2.2 Experimental Details 48
2.3 Results and Discussion 49
2.3.1 Red-Blue Double Emissive Layer White OLEDs 49
2.3.2 Red-Blue-Green Triple Emissive Layer and Red-Blue-Blue-Green Quadruple Emissive Layer White OLEDs 50
2.3.3 Emission Mechanism in Multiple Emissive Layer White OLEDs 52
2.4 Summary 55

3 GREEN PHOSPHORESCENT STACKED ORGANIC LIGHT-EMITTING DIODES 64

3.1 Background and Motivation 64
3.2 Experimental Details 64
3.3 Results and Discussion 65
3.3.1 Study of Charge generation Units in Stacked Organic Light-Emitting Diodes 65
3.3.2 Single and Double Stacked Organic Light-Emitting Diodes 68
3.4. Summary 71

4 POLYMER-COLLOIDAL QUANTUM DOT HYBRID NEAR INFRARED LIGHT-EMITTING DEVICES 80

4.1 Background and Motivation 80
4.2 Experimental Details 80
4.2.1 Synthesis and Processing of PbSe Colloidal Quantum Dots 80
4.2.2. Device Fabrication 81
4.2.3. Characterization of PbSe Colloidal Quantum Dots and Hybrid Light-Emitting Devices 81
4.3 Results and Discussion 82
4.3.1 PbSe Colloidal Quantum Dots 82
4.3.2 Hybrid Multilayer QD LEDs 82
4.3.3 Hybrid Polymer-QD LEDs 84
4.3.3.1 Effect of QD concentration 85
4.3.3.2 Effect of active layer thickness 87
4.4 Summary 88

5 NEAR INFRARED-TO-GREEN ORGANIC UP-CONVERSION DEVICES 97

5.1 Background and Motivation 97
5.2 Experimental Details 98
5.3 Results and Discussion 99
5.3.1 Control Up-Conversion Device 99
5.3.2 Effect of Hole Blocking Layer 100
5.3.3 Effect of Electron Injection Layer 102
5.3.4 Dependence of Optical Power Density 103
5.4 Summary 104

6 QUANTUM DOT BASED NEAR INFRARED-TO-GREEN HYBRID UP-CONVERSION DEVICES 112

6.1. Background and Motivation 112
6.2. Experimental Details 113
6.3. Results and Discussion 115
6.4. Summary 120

7 CONCLUSION 127

APPENDIX : MOLECULAR STRUCTURES OF ORGANIC MATERIALS USED IN THIS DISSERTATION 129

LIST OF REFERENCES 133

BIOGRAPHICAL SKETCH 138

LIST OF TABLES

Table page

5-1 Materials used in this work for hole blocking layers with their respective HOMO and LUMO energies. 105

5-2 Dark-current-induced turn-on voltage and maximum operating photon-to-photon conversion efficiency with various hole injection structures. 105

LIST OF FIGURES

Figure page

1-1 Various display applications with OLEDs 40

1-2 Forecast of AMOLED capacity and year-by-year growth rate 40

1-3 Comparison of the key-performance parameters of WOLEDs relative to incandescent lamps, fluorescent tubes and inorganic white LEDs. 41

1-4 Various luminaires with OLEDs panels demonstrated by OLED lighting companies 42

1-5 Comparison of eye sensitivity functions for the photopic and scotopic vision regime 42

1-6 CIE (1931) and CIE (1978) xyz color matching functions (CMFs). Note that the CIE 1931 CMF is the currently valid official standard. 43

1-7 CIE 1931 (x, y) chromaticity diagram. White light is located in the center. Also shown are the regions of distinct colors..... 43

1-8 Schematic drawing of electronic states of organic semiconductors..... 44

1-9 Schematic drawing of non-radiative inter-molecular energy transfer processes. 44

1-10 Schematic illustration of Jablonski energy diagram 45

1-11 Schematic illustration of the preparation of monodisperse QDs based on La Mer model 45

1-12 Schematic comparison of quantization of density of states 46

2-1 Energy level diagram of materials used in this study. 56

2-2 Device structure and electroluminescence spectra of R-B double emissive layer white OLEDs: A) schematic diagram of the device structure and B) EL spectra of double emissive layer white OLEDs..... 56

2-3 L-I-V characteristics and efficiencies of double emissive layer white OLEDs 57

2-4 Device structure and electroluminescence spectra of R-B-G triple emissive layer white OLEDs. 58

2-5 Device structure and electroluminescence spectra of R-B-B-G quadruple emissive layer white OLEDs 58

2-6 Electroluminescence spectra of monochromatic and white OLEDs and efficiencies of white OLEDs 59

2-7 Device structure and electroluminescence spectra of devices for the investigation of emission mechanism 60

2-8 Schematic illustration of emission mechanism in R-B-B-G quadruple emissive layer WOLEDs. 61

2-9 Comparison of I-V characteristics and efficiencies of double and triple emissive layer OLEDs 62

2-10 Device structure, EL spectra and efficiencies of R-B-G triple emissive layer white OLEDs with balanced emission 63

3-1 Schematic energy diagram of charge generation devices with different presence of the interconnecting unit 72

3-2 Device structure and I-V characteristics of devices with different presence of interconnecting units 73

3-3 Proposed schematic energy band diagram of the charge generation interconnecting unit. 74

3-4 Current densities of charge generation devices as a function of voltage with various Cs_2CO_3 doping concentration in a BPhen electron transporting layer.... 74

3-5 Current densities of charge generation devices as a function of voltage with and without a thin Al interlayer 75

3-6 Luminance plots as a function of voltage of double stacked green phosphorescent OLEDs with different charge generation interfaces. 75

3-7 Current density plots as a function of voltage of NPB and TAPC hole only devices 76

3-8 Schematic device structures of double stacked phosphorescent OLEDs. 77

3-9 L-I-V characteristics and efficiencies of single and double stacked green phosphorescent OLEDs 78

3-10 L-I-V characteristics and efficiencies of single and double stacked green phosphorescent OLEDs with the modified device structure 79

4-1 Schmatic drawing of the PbSe quantum dot synthesis and PbSe quantum dots capped with oleic acid ligands 90

4-2 Optical properties of colloidal PbSe QDs 90

4-3 Photocurrent densities, current densities (insets) and efficiencies of multilayer hybrid LEDs 91

4-4 AFM images of different surface treatment on CuPc layer 92

4-5 Schematic illustration of phase segregation technique and AFM images of QDs on an organic layer 92

4-6 L-I-V chracteristics and efficiencies of multilayer hybrid LEDs by phase segregation method and AFM images of QDs on an organic layer 93

4-7 Schematic diagram of polymer-QD device structure and energy levels. 94

4-8 L-I-V characteristics and electroluminescence spectra 94

4-9 L-I-V characteristics and efficiencies of hybrid LEDs. 95

4-10 External quantum efficiency plot of hybrid LEDs containing 6wt. % PbSe QDs as a function of active layer thickness. 96

5-1 Schematic drawing and L-I-V characteristics of the up-conversion device and infrared absorption of SnPc and SnPc:C_{60} mixed layer 106

5-2 Schematic energy band diagrams of the up-conversion device under applied voltage 107

5-3 Luminance plots of up-conversion devices with various hole injection properties 108

5-4 Luminance plots and efficiencies of up-conversion devices with various electron injection layers 109

5-5 L-I-V characteristics and maximum operating photon-to-photon conversion efficiencies measured with different incident optical power 110

5-6 Images of device operation for up-conversion devices with different device sizes 111

6-1 Schematic drawing of the process of BDT treatment on QD films 121

6-2 Absorption spectra of PbSe QDs with various sizes. 121

6-3 Device structure and L-I-V characteristics of PbSe QD up-conversion device without a hole blocking layer 122

6-4 Device structure and L-I-V characteristics of PbSe QD up-conversion device with a hole blocking layer. 123

6-5 Luminance at 13 V with a linear dependence on the NIR power densities. 124

6-6 P-P conversion efficiency as a function of voltage with schematic drawing of up-conversion operation and P-E and E-P conversion efficiencies 125

6-7 Spectral photon-to-photon conversion efficiency of PbSe QD up-conversion device as a function of wavelength under different applied voltages. 126

6-8 Images of an up-conversion device with (left) and without (right) 1.3 mm NIR illumination under 15 V. 126

LIST OF ABBREVIATIONS

3TPYMB	tris[3-(3-pyridyl)mesityl]borane
Alq_3	tris(8-hydroxy-quinolinato)aluminium
BCP	bathocuproine
BPhen	bathophenanthroline
CBP	4,4'-bis(carbazol-9-yl)biphenyl
CBM	conduction band minimum
CuPc	copper phthalcyanine
EAL	electron accepting layer
EQE	external quantum efficiency
ETL	electron transporting layer
Firpic	iridium (III) bis[(4,6-difluorophenyl)pyridinato]picolinate
HAT-CN	1,4,5,8,9,11-hexaazatriphenylene-hexacarbonitrile
HBL	hole blocking layer
HTL	hole transporting layer
HOMO	highest occupied molecular orbital
IQE	internal quantum efficiency
$Ir(MDQ)_2(acac)$	bis(2-methyl-dibenzo[f,h]quinoxaline)(acetylacetonate)iridium (III)
$Ir(ppy)_3$	tris(2-phenylpyridine)iridium(III)
ITO	indium tin oxide
LUMO	lowest unoccupied molecular orbital
mCP	1,3-bis(carbazol-9-yl)benzene
MEH-PPV	poly[2-methoxy-5-(2'-ethyl-hexyloxy)-1,4-phenylene vinylene]
NPB	N,N'-bis(naphthalen-1-yl)-N,N'-bis(phenyl)-benzidine
NTCDA	1,4,5,8-naphthalenetetracarboxylic dianhydride

OLED	organic light-emitting diode
PEDOT:PSS	poly(3,4-ethylenedioxythiophene)-poly(styrenesulfonate)
PhOLED	phosphorescent organic light-emitting diode
PLED	polymer light-emitting diode
QD	quantum dot
SnPc	tin (II) phthalocyanine
TAPC	di-[4-(N,N-ditolyl-amino)-phenyl]cyclohexane
TAZ	3-(4-biphenyl)-4-phenyl-5-tert-butylphenyl-1,2,4-triazole
TPBi	2,2’,2’’-(1,3,5-benzinetriyl)-tris(1-phenyl-1-H-benzemidazole)
UGH2	1,4-bis(triphenylsilyl)benzene
VBM	valence band maximum
WOLED	white organic light-emitting diode

Abstract of Dissertation Presented to the Graduate School
of the University of Florida in Partial Fulfillment of the
Requirements for the Degree of Doctor of Philosophy

ORGANIC LIGHT-EMITTING DIODES AND RELATED HYBRID LIGHT-EMITTING DEVICES

By

Dong Woo Song

December 2011

Chair: Franky So
Major: Materials Science and Engineering

Organic optoelectronic devices have attracted a great deal of attention due to their compatibility with flexible substrates, low cost process and large area applications. In this work, we have fabricated various organic and quantum dot (QD) based light-emitting devices and studied the basics in the devices.

First, we study on the emission mechanism in white organic light-emitting diodes (WOLEDs). The emission mechanism in double, triple and quadruple emissive layer WOLEDs was studied from simple EL measurements with changing device configurations. The understanding of the emission mechanism helps us to design efficient WOLEDs with the peak power efficiency of 30 lm/W and high CRI of 82.5.

Next, we studied the charge generation mechanism in stacked OLEDs. We found that overall current generated from the charge generation units is significantly dependent on the electron flow through steep energy barrier of n-doped ETL, which is affected by doping concentration, if efficient electron accepting materials are used. We fabricated green phosphorescent stacked OLEDs, and found that efficient electron accepting materials and trap-free hole transporting materials like NPB are needed to obtain effective charge generation.

We also demonstrated hybrid infrared LEDs based on PbSe colloidal QDs and MEH-PPV polymer. Through the study and optimization of the devices, we obtained the maximum external quantum efficiency of 0.83 % at the peak wavelength of 1280 nm. This work exhibited a significant enhancement in device efficiencies compared to previously reported QD based IR LEDs.

We demonstrated NIR-to-green organic up-conversion devices with various hole blocking structures. Both to thicken IR sensitizing layer and to insert hole blocking layer enabled the enhanced on/off characteristics due to the suppression of hole injection from the anode. The maximum operating photon-to-photon conversion efficiency is 2.54 %.

Lastly, we have demonstrated low-cost hybrid up-conversion devices with infrared sensitivity to 1.5 μm by incorporating a colloidal PbSe QD NIR sensitizing layer with green phosphorescent OLEDs. To keep the device off in the absence of IR excitation, a ZnO nanoparticle hole blocking layer is incorporated in the OLEDs. The maximum photon-to-photon conversion efficiency of an optimized device at peak wavelength of 1.3 μm is 1.3 %.

CHAPTER 1
INTRODUCTION

1.1 Organic Light-Emitting Diodes

1.1.1 Advantages and Disadvantages of Organic Materials

Organic semiconductors have many advantages over inorganic semiconductors. First, these materials are suitable for low cost and large area manufacturing processes. Vacuum thermal evaporation (VTE) of small molecules is quite simple compared to thin film processes of inorganic semiconductors such as pulsed laser deposition (PLD), plasma enhanced chemical vapor deposition (PECVD), metal-organic chemical vapor deposition (MOCVD) and molecular beam epitaxy (MBE). Solution processing of polymer thin films such as spin coating and inkjet printing requires even lower cost of processing. Also, roll-to-roll processing of polymers is potentially suitable for high throughput, low cost and large scale manufacturing.

In addition, organic materials are capable to control their electronic and optical properties by chemical modification. For example, emission spectrum of the organic molecules in OLEDs can be tuned by tailoring their molecular structures. Change in absorption wavelengths and absorption coefficients in organic photovoltaics (OPVs) can also be achieved with a variety of molecular structures of these organic materials.

Also, organic materials are compatible with flexible substrate due to soft nature of these materials. In addition, since extremely thin layers of organic materials (~100 nm) are required to realize optoelectronic devices, the organic semiconductors can be the best choice for the flexible display applications.

On the other hand, organic materials have some disadvantages for the application of electronic and optoelectronic devices. Organic semiconductors are bonded with van

der Waals force, which is significantly weaker than covalent bond in inorganic semiconductors. As a result of the weak intermolecular interactions, these materials show much lower carrier mobilities, typically less than 1 cm^2/V sec than inorganic semiconductors. The charge carrier density is also low in organic semiconductors, resulting in lower electrical conductivity.

Another problem of these materials is the high trap density due to the impurities and structural defects. Purification of the organic materials is difficult, so the purity levels are generally lower than those in inorganic semiconductors. Moreover, most organic devices exhibit degradation in ambient condition, and thus the lifetime of the devices is a big issue. Hence, there have extensive research works on encapsulation have been conducted for the commercialization.

1.1.2 Applications of OLEDs

An organic light-emitting diode (OLED) is a light-emitting diode in which the emissive electroluminescent layer consists of a thin film of organic semiconductors. The OLED is the most mature technology among the device technologies based on organic semiconductors. In 1987, researchers at Eastman Kodak released reports on light-emitting devices using organic small molecules. Although the first devices were only close to 1 % of external quantum efficiency [1], the potential of this technology has initiated extensive research over a few decades to achieve efficient and stable OLEDs. There are two main areas in OLED applications. One is the display application, and the other is the lighting application. In both areas, OLEDs containing unique characteristics of organic semiconductors are competing with other technologies and expanding their markets.

1.1.2.1 Display applications

The liquid crystal display (LCD) is the most prevalent display type until now, but the OLED has clear advantages over LCD. Short radiative lifetime of organic materials enables OLEDs to achieve much faster response time. Thus, the OLED can be a better display for watching sports or movies, and even for 3D. Wide viewing angle, high contrast and low power consumption are also advantages of OLEDs. The flexibility of organic materials and the thin film thickness make OLEDs appropriate to flexible display applications.

Various efforts have been conducted to realize highly efficient red, green and blue OLEDs in both passive matrix (PM) and active matrix (AM) displays. Since first commercialized 11'' OLED display was introduced by Sony in 2007, many types of products with small OLED displays such as mobile phones (Figure 1-1A), A/V players and digital cameras have been widely introduced for the consumer market. The growth in size and volume of AMOLED manufacturing is becoming a reality, as Samsung started producing AMOLED panels in their new 5.5-Gen (1,300 mm X 1,500 mm) fab (Figure 1-2) [2]. Up to now, however, most of the new AMOLED manufacturing lines are optimized for small or medium display production.

On the contrary, for large panel displays like TVs and monitors, commercially available OLEDs are still very limited whereas a few prototypes have been introduced (Figure 1-1B). Since several companies such as Sony, LG Display and Samsung are working on large OLED panel displays, OLED TVs or monitors are expected to be available in consumer markets in a few years.

Because of the unique properties of organic materials, next generation devices such as flexible or transparent displays have been demonstrated in the Consumer

Electronic Show (CES) (Figure 1-1C and D). These types of displays are expected to widen the OLED applications in consumer markets in the near future.

1.1.2.2 Lighting applications

As energy consumption is steadily growing every year, energy resource problem is now globally accepted as a serious issue and there have been numerous efforts to harvest energy from alternative energy sources such as sunlight, water and wind. Also, a lot of efforts have been conducted for electronic devices with low electrical power consumption to alleviate the energy issue.

Based on a report from Department of Energy in 2002 [3], about 22 % of the total electricity generated in the United States is consumed by lighting. It is obvious that increasing the efficiency of lighting can lead to significant energy savings. Until now, dominant types of general lighting are incandescent lamp and fluorescent lamp. Since incandescent lamp is a blackbody radiator, approximately 90 % of power is dissipated as heat, leading to low efficiency of nearly 15 lm/W. As a result, phasing out the use of incandescent light bulbs has started or plans to start globally to use more efficient light sources. Fluorescent lamp shows relatively high efficiency up to 100 lm/W, but it provokes environmental and health concerns due to its inclusion of mercury. Therefore, solid state lighting has been gaining interest in recent years. While inorganic light-emitting diodes are leading the recent approach for solid state lighting, OLED lighting is expected to expand its area in the markets. OLEDs are unique light sources which can be applied as flexible and large-area illumination. OLEDs can be also cost effective as luminaires due to their low cost processing. Figure 1-3 shows the brief comparison of white OLEDs to existing lighting technologies [4].

Drastic improvements to the materials, the device architecture and the light extraction techniques have enabled a significant enhancement in WOLED efficiency. Since Kido et al. introduced the first WOLED with the efficiency of below 1 lm/W [5], the commercial prototypes recently surpassed 100 lm/W. A drastic advance with 60 lm/W was reached in 2006 by Kido's group [6], and researchers at Universal Display Corporation announced that they achieved a WOLED with the efficiency in excess of 100 lm/W under laboratory conditions [7]. More recently, Reineke et al. reported WOLEDs with the efficiency of over 120 lm/W under laboratory conditions. This efficiency is higher than that of most commercial fluorescent tubes [8].

A lot of OLED lighting products have been introduced by Philips, Osram, GE and LG Chem. These companies have been focused not only on achieving highly efficient white light sources, but also on building lamps with appealing design. The market of the OLED lighting is still not as big as display, but it is growing quite fast. The requirement of the white light source for lighting is different from that for display. It requires higher luminance of 1000 cd/m^2, good CRI of over 70, similar CIE coordinates to a blackbody radiator, and a CCT of a range of 2500 to 6000 K.

1.1.3 Basic Concepts for OLED Lighting

1.1.3.1 Basics in colorimetry

Photopic and scotopic response. Human eyes detect light through cone and rod cells, and nerves transmit the information to the brain. In relatively bright environment (>3 cd/m^2), a human eye follows the photopic response or daylight vision mediated by the cones. There are three types of cone cells sensitive in the red, green and blue spectral range. Their sensitivities overlap to provide vision over the whole visible spectrum. The maximum luminous efficacy is 683 lm/W at a wavelength of 555 nm.

On the contrary, in relatively dark condition (<0.01 cd/m^2), a human eye follows the scotopic response or night vision mediated by the rods. Rod cells are more light sensitive than cone cells, and sensitive through the entire visible spectrum. As the sense of color is lost in the scotopic vision regime and objects appear with gray levels, the following discussion in colorimetry relates to the photopic vision regime.

Luminous intensity, luminous flux and luminance. The optical properties such as the number of photons, photon energy and optical power are characterized by radiometric units. However, the human eye can detect only the range of visible spectrum (400-700 nm) and the eye sensitivity varies significantly within the spectral range. Therefore, for quantifying the brightness and the color perception by the human eye, different types of units are needed. These parameters are expressed by photometric units.

Luminous intensity represents the light intensity of a light source as perceived by the human eye. The unit of luminous intensity is candela (cd). 1 cd is defined as the luminous intensity of a monochromatic light at 555 nm with an optical power of 1/683 W into a solid angle of 1 steradian (sr).

Luminous flux represents the light power of a light source as detected by the human eye. The unit of luminous flux is lumen (lm). 1 lm is defined as the luminous flux of a monochromatic light at 555 nm with an optical power of 1/683 W. Generally, it can be obtained using the equation.

$$\Phi = 683\frac{lm}{W}\int_{\lambda} V(\lambda)P(\lambda)d\lambda$$

Based on the definitions of candela and lumen, 1 cd equals 1 lm/sr. Hence, an isotropic light source with a luminous intensity of 1 cd corresponds to a luminous flux of 4π lm.

The luminance of a device is the ratio of the luminous intensity (in units of cd) per the projected area of the device in a certain direction (in units of m^2). The unit is commonly expressed as cd/m^2 or nit.

CIE color coordinates. CIE color coordinates are used to indicate the chromaticity of any light source. This system was originally recommended in 1931 by International Commission on Illumination (CIE). The CIE is defined by giving the amounts of three imaginary colors of X, Y, and Z. The tristimulus values of a color are calculated as a summation of the spectral compositions of the radiant power of the light source times the spectral tristimulus values or color matching functions for an equal power source.

$$X = \int_{\lambda} \bar{x}(\lambda) P(\lambda) d\lambda$$

$$Y = \int_{\lambda} \bar{y}(\lambda) P(\lambda) d\lambda$$

$$Z = \int_{\lambda} \bar{z}(\lambda) P(\lambda) d\lambda$$

Chromaticity coordinates (x, y, z) can be calculated by:

$$x = \frac{X}{X + Y + Z}$$

$$y = \frac{Y}{X + Y + Z}$$

$$z = \frac{Z}{X + Y + Z}$$

Since z = 1 – x – y, the color coordinates is expressed in terms of x and y.

Color rendering index (CRI) and correlated color temperature (CCT). The CRI and the CCT are very useful parameters to indicate the quality of white illumination sources. The CRI is a quantitative measure of the ability of a light source to represent the colors of various objects compared to an ideal light source or Planck's blackbody spectrum. The CRI is determined on a scale of 0 (monochromatic spectrum) to 100 (blackbody-like spectrum). Light sources with a CRI value of above 80 are considered as high quality lighting sources.

The CCT is used to describe the color difference of white light source by comparing its chromaticity with that of blackbody radiator. The CCT is the temperature at which the blackbody radiator matches the color of the light source. Higher color (>5000 K) temperature refers to cool color and lower color temperature (2700 – 3000 K) matches with warm color.

1.1.3.2 Basics in device measurements

Current efficiency and external quantum efficiency (EQE). Current efficiency, also called luminous efficiency is the ratio of luminance to the injected current to the device. It is measured in units of cd/A. It can be calculated by measuring L (luminance)-J (current density)-V (voltage) characteristics of the device.

$$\eta_L(cd/A) = \frac{L(cd/m^2)}{J(mA/cm^2)\times 10}$$

External quantum efficiency (η_{EQE}) expressed with %, is defined as the ratio of the number of photons emitted in the forward direction to the number of charge carriers injected into the device. The current efficiency can be converted from the EQE when we take into account the photopic response of the eye from EQE, and vice versa.

$$\eta_{EQE}(\%) = \frac{\int \frac{I(\lambda)}{hc/\lambda} d\lambda}{I_{OLED}/q} \times 100$$

The EQE is the product of the internal quantum efficiency (IQE or η_{IQE}) and the extraction efficiency ($\eta_{extraction}$). The internal quantum efficiency is defined as the ratio of the number of photons emitted inside the active region to the number of charge carriers injected into the device, and the extraction efficiency is defined the ratio of the number of photons emitted into free space to the number of photons emitted inside the active region. Thus, there are two pathways to increase the EQE: increasing the IQE and increasing the extraction efficiency. Although the extraction efficiency plays an important role in the EQE, we focus on the maximization of the IQE in this dissertation.

Power efficiency. The power efficiency is the ratio of the luminous power emitted in the forward direction to the electrical power required to drive the device. It is expressed in units of lm/W.

$$\eta_P(lm/W) = \frac{\Phi(lm)}{I(amp)V(volt)}$$

In all measurements of the OLEDs in this dissertation, we calculate the efficiency only in the forward direction. The photocurrent in the forward direction is measured by a photodiode and converted to the number of photons and luminance.

1.1.4 Physics in Organic Light-Emitting Diodes

1.1.4.1 Electronic structures

Most organic materials are carbon-based compounds incorporating with other atoms such as hydrogen, nitrogen and oxygen. Organic materials used in OLEDs are mostly conjugated molecules. Strong covalent bonding between conjugated carbons forms sp^2 hybrid orbitals with σ-bonds and p_z orbitals perpendicular to the plane

containing all carbon atoms. The overlap between the neighboring p_z electrons forms the π-bonds. The π-electrons of carbon in the conjugated molecule are delocalized within the molecule, and the delocalized π-electrons enable charge transport in organic materials. Similar to the valence band (VB) and the conduction band (CB) for inorganic semiconductors, the overlap of π-orbitals creates a degeneracy, leading to the formation of filled and unfilled bands with the edges of the highest occupied molecular orbital (HOMO) and the lowest unoccupied molecular orbital (LUMO), respectively. Interactions between the π-electrons and the σ-electrons within the molecules determine the gap between the HOMO and LUMO levels, where the optical properties of organic semiconductors are determined by π-π^* transition.

1.1.4.2 Charge transport

The charge carrier transport in organic semiconductors remains a topic for theoretical and experimental study. There are two types of charge transport mechanism in organic materials, band transport model and polaron hopping transport model.

The band transport model. The band transport is usually observed in highly crystalline organic solids. For delocalized charged carriers in organic semiconductors, the bands are analogous to those in crystalline inorganic semiconductors. Consequently, the mobility in molecular crystals such as pentacene reaches up to $1\text{-}10^{-2}$ cm^2/V sec.

The hopping transport model. The hopping transport is observed in amorphous organic solids. The weak van der Waals intermolecular force in amorphous organic materials leads to the formation of localized and narrow bands. Hence, the intermolecular hopping mechanism is dominant instead of band transport. The typical

charge carrier mobility of amorphous organic solids is in the range of 10^{-3} – 10^{-10} cm^2/V sec.

1.1.4.3 Excitons and intermolecular exciton energy transfer

The exciton is defined as a bound electron-hole pair by coulombic force. It can diffuse inside solids and transfer energy without transporting net charge. Excitons play an important role in optoelectronic properties in organic materials. Because of the strong tendency of localization of charge carriers, excitation in organic materials is considered to create excitons instead of free electrons and holes.

The intermolecular energy transfer is a nonradiative process between molecules, and it can be classified into two main types of exciton energy transfer, Förster transfer and Dexter transfer.

Förster transfer. The Förster energy transfer originates from the dipole-dipole interaction, typically in singlet-singlet transitions with very fast rate. This resonant energy transfer requires the overlap between the emission spectrum of the donor and the absorption spectrum of the acceptor. Förster energy transfer occurs in relatively long range (~ 10 nm), as the transfer rate is proportional to the r^{-6}, where r is the distance between donor and acceptor.

Dexter transfer. The Dexter energy transfer occurs when electrons are exchanged between molecules, so electron wave function must be overlapped with very short separation length (~ 1nm) between donor and acceptor molecules. The transfer rate is exponentially reduced ($\propto$ exp(-2r/L)) with longer distance between donor and acceptor. This dipole-dipole coupling can happen in triplet exciton energy transfer. For this mechanism, the spin conservation rule is obeyed.

1.1.4.4 Fluorescence and phosphorescence

There are four spin states in an exciton. The total wave function of a two-electron system must be anti-symmetric based on the Pauli's principle. The symmetric and anti-symmetric wave functions can be expressed as follows,

$$\Psi_S = \frac{1}{\sqrt{2}}\{\left|\uparrow(1)\downarrow(2)\right\rangle + \left|\uparrow(1)\downarrow(2)\right\rangle\}$$

$$\Psi_S = \left|\uparrow(1)\uparrow(2)\right\rangle$$

$$\Psi_S = \left|\downarrow(1)\downarrow(2)\right\rangle$$

$$\Psi_A = \frac{1}{\sqrt{2}}\{\left|\uparrow(1)\downarrow(2)\right\rangle - \left|\uparrow(1)\downarrow(2)\right\rangle\}$$

The symmetric spin state is called as the triplet state, and the anti-symmetric spin state is called as the singlet state. Based on the degeneracy of the spin states, the ratio of the number of singlet state to the number of triplet states is statistically determined as 1:3. The radiative singlet decay is called as fluorescence, and the radiative triplet decay is called as phosphorescence.

Fluorescence. Fluorescence is the spontaneous emission of radiation within a few nanoseconds of excitation of the molecule. Once the molecule is excited by optical absorption or electrical transport, the relaxation of the excitation occurs, and then is followed by radiative decay via fluorescence.

Phosphorescence. Phosphorescence is the spontaneous emission of radiation for long period of times of excitation of the molecule. In nature, phosphorescence very rare occurs except in materials with strong singlet-triplet mixing. Organometallic compounds containing heavy metals such as iridium, platinum, osmium and rhthenium exhibit strong spin-orbit coupling. Strong spin-orbit coupling enables effective mixing of singlet and triplet states. Hence, 100 % of internal quantum efficiency is theoretically

possible by converting all singlet and triplet excitons into phosphorescence with the presence of organometallic compounds as emitters.

1.2 Colloidal Quantum Dot-Based Hybrid Light-Emitting Diodes

1.2.1 State of the Art Hybrid LEDs

A quantum dot (QD) is defined as a nanoscale material whose excitons are confined in all three spatial dimensions. It is also referred as a nanocrystal or a nanodot. These QDs can be utilized for a lot of optoelectronic and electronic devices such as light-emitting diodes, photodetectors, solar cells, field-effect transistors and memory devices. In contrast to OLEDs, colloidal QD devices have not reached to the commercial market, but there have been a lot of research works on the QD devices. In this work, we summarize the previous works on hybrid LEDs in Chapter 1.2 and hybrid photodetectors in Chapter 1.3.

1.2.1.1 Visible-emitting hybrid LEDs

The advantage of the mature OLED technology can be combined with the properties of QDs, whose emission spectrum and energy levels can be controlled by tailoring QD size. Since first hybrid LEDs employing CdSe colloidal quantum dots was reported by Colvin et al. in 1994 [10], drastic improvement has been achieved in QD-LED efficiencies.

In the first QD-LEDs, Colvin et al. used poly(p-phenylenevinylene) (PPV) as hole transporting layer and TOPO-capped CdSe QD layer as emitting and electron transporting layer [10]. The luminance of around 100 cd/m^2 was obtained. However, the emission from QDs were overlapped with that from polymer, and the EQEs were quite low of 0.001 – 0.01 %.

Mattoussi et al. and Schlamp et al. demonstrated similar QD-LEDs based on CdSe/ZnS core/shell QDs and CdSe/CdS core/shell QDs, respectively [11]. The emission was almost exclusively from the QDs, but the EQEs were still low of 0.1 – 0.22 %.

Drastic improvement has been achieved by Bulovic and Bawendi groups [12]. The devices were fabricated by phase separation of the QDs and a hole transporting material (TPD). The thin layer of luminescent CdSe/ZnS core/shell QDs was sandwiched between hole transporting and electron transporting layers. The EQE was measured as over 2 %.

Sun et al. reported QD-LEDs with saturated red, orange, yellow and green emission [13]. The CdSe/ZnS core/shell QD layer was coated on poly-TPD hole transporting layer. Based on the narrow EL bandwidth and longer operation times at high luminance (300 hours of LT_{50} at >1,100 cd/m^2), QD-LEDs can be promising in large-area displays.

QD-LEDs have also been studied for the application of lighting sources. Anikeeva et al. demonstrated white QD-LEDs with the emitting layer of mixture of red, green and blue emitting QDs [14]. These mixed-monolayer QD-LEDs exhibited white emission with CIE coordinates of (0.35, 0.41) at 9 V. The peak EQE was reported as 0.36 % at operating voltage of 5 V.

After a few decades of research efforts, QD-LEDs are now competing with OLEDs, next generation display and solid-state lighting. However, to penetrate the consumer markets, there are some issues on the QD-LEDs to be solved. First, the performance, lifetime and cost should be competitive with OLEDs. Also, most of QD-LEDs contain

toxic elements such as cadmium, and thus Cd-containing QDs should be replaced with QDs with other non-toxic elements.

1.2.1.2 Infrared-emitting hybrid LEDs

There is another promising area to apply QD-LEDs is the near infrared (NIR) emitting devices. Although most of works on semiconductor QDs have been carried out in the visible spectral range, interest in infrared-emitting QDs has grown rapidly in a decade due to their potential applications for telecommunications, biological sensors and electroluminescent devices.

NIR-emitting hybrid LEDs are based on narrow bandgap semiconductor QDs such as InAs, PbSe, PbS and HeTe. The first report on IR hybrid LEDs was based on polymer-QD blend devices [15]. They consist of mixed films of core/shell InAs/ZnSe QDs and poly(2-methoxy-5-(2-ethylhexyloxy)-1,4-phenylenevinylene) (MEH-PPV) or poly(9,9-dehexylfluorenyl-2,7-diyl)-co-(1,4-{benzo-(2,1',3)thiadiazole}) (F6BT) conducting polymer. The devices exhibited broad emission near 1.3 μm and a remarkably high external quantum efficiency of roughly 0.5 % at high voltages of over 25 V.

Another work on polymer-QD blend devices was reported [16]. The devices were based on the blend of methyl-substituted ladder-type poly(para-phenylene) (MeLPPP) and HeTe QDs. The emission from HeTe QDs was observed in the range of 900 to 2000 nm, but the blue-green emission was also shown from MeLPPP. The EQE was measured as around 0.001 %.

Trilayer NIR-emitting hybrid LEDs based on small molecules and PbSe QDs have been reported [17]. The device fabrication method was similar to the visible CdSe/ZnS

QD based LEDs. A PbSe QD monolayer was formed by phase segregation from TPD or NPD, followed by vacuum deposition of Alq_3 and/or BCP. The IR emission was observed from 1.33 to 1.56 μm with a low EQE of about 0.001 %.

1.2.2 Colloidal Quantum Dots

1.2.2.1 Synthesis of colloidal quantum dots

Colloidal compound semiconductor quantum dots can be synthesized by a hot solution process [18]. Figure 1-11B depicts the schematic drawing of the QD synthetic apparatus. Supersaturated precursors are prepared in a vigorously stirred flask containing a hot coordinating solvent. Next, rapid injection of organometallic precursors initiates the nucleation and subsequent growth of quantum dots. According to the classic researches by La Mer and Dinegar [19], monodisperse colloidal quantum dots can be realized with a temporally discrete nucleation followed by slower controlled growth on the nuclei, as shown in Figure 1-11A. Rapid injection of reagents to the reaction flask increases the precursor concentration over the nucleation threshold. As long as the consumption of the precursors by the growth of quantum dots is not exceed by the injection rate of the precursors, no new nuclei are formed. In this step, as the growth rate of quantum dots are similar each other, the initial size distribution is narrow if the portion of quantum dot growth is small enough during the nucleation period.

Many systems exhibit a second step of growth called Ostwald ripening. In this step, the dissolution of small quantum dots with high surface energy is favored, and the materials are redeposited on the larger quantum dots, resulting in the larger overall quantum dot size over time. Since it leads to wide size distribution of the quantum dots, Ostwald ripening should be limited to achieve monodisperse colloidal quantum dots.

1.2.2.2 Optical properties of colloidal quantum dots

Quantum dots have been theoretically even before they were able to be synthesized. When semiconductor crystals are small enough, the nanocrystals exhibit drastic deviation in their optical, electronic, magnetic and chemical properties from bulk crystals. As the size of the nanocrystals is reduced into nano-scale dimensions, the energy levels start to separate because of the quantum confinement effects. Quantum confinement is the condition under which the electrons and holes are confined in a limited volume and dimension. Figure 1-12 shows the quantum dot confinement in various dimensional nanoscale structures. In case of bulk materials, the average separation between an electron and a hole, known as exciton Bohr radius, is much smaller than the dimensions of the materials, and thus they can freely move, leading to the continuous density of states. On the other hand, the exciton Bohr radius is comparable and larger than the dimensions of the materials in a quantum confined structure. As a result, the charge carriers are forced to be confined within restricted paths, and the density of states is discrete for quantum dots. Consequently, the optical band gap of the QDs becomes different from that of bulk materials.

Optical properties of the quantum dots can be tuned by changing material and controlling size. The sample absorb at wavelengths shorter than a certain wavelength, corresponding to the bandgap of the QDs. The emission peak is quite narrow due to the narrow size distribution.

1.3 Organic and Hybrid Photodetectors and Organic Up-Conversion Devices

1.3.1 Visible Organic Photodetectors

Organic thin film photodetectors have attracted a great deal of attention due to their compatibility with flexible substrates, low cost processes and large area

applications. Organic photodetectors with high quantum efficiency of over 70 % at 10 V have been reported by employing a multilayer method of copper phthalocyanine (CuPc)-3,4,9,10-perylenetetracarboxylic bisbenzimidazole (PTCBI) as a donor and an acceptor, respectively [20]. However, the organic photodetectors using multilayers of CuPc and PTCBI exhibited low EQEs of below 10 % at low applied voltage (at less than 1 V), showing strong field dependence. This strong field dependence is attributed to the short exciton diffusion length of PTCBI, preventing the efficient dissociation of photogenerated excitons [21]. Meanwhile, the small molecule OPVs with twice power conversion efficiency were reported by substituting a C_{60} acceptor with longer exciton diffusion length of around 77 A for a PTCBI acceptor with excition diffusion length of about 30 A [22]. Thus, organic photodetectors can be expected to obtain higher EQEs by replacing PTCBI with C_{60}.

1.3.2 Infrared Organic Photodetectors

There are a lot of applications for detecting photons in infrared range wavelengths: night vision, bioimaging, optical communications, spectroscopy and chemical analysis. In spite of a great attention in organic photodetectors, most reported organic photodetectors were limited in photosensitivity in visible range wavelengths, and only a few works were reported for infrared organic photodetectors due to the lack of IR sensitive organic materials.

Gong et al. reported infrared polymer photodetectors based on poly(5,7-bis(4-decanyl-2-thienyl)-thieno (3,4-b)diathiazole-thiophene-2,5) PDDTT:(6,6)-phenyl-C_{61}-butyric acid methyl ester (PCBM) bulk heterojunction photoactive layer [23]. The devices exhibited broad spectral response in the range of 300 to 1450 nm. The

detectivities were in the order of 10^{12} – 10^{13} Jones (or cm $Hz^{1/2}$/W), which are comparable to or better than those from inorganic semiconductor photodetectors.

Zimmerman et al. reported infrared small molecule photodetectors with porphyrin-tape compounds/C_{60} donor/acceptor layer [24]. The Zn-phophyrin-tape included the additives such as PCBM and 4,4'-bipyridyl (Bipy). The devices showed the detectivities of 8.8 X 10^{11} Jones at 1130 nm and 8.2 X 10^{10} Jones at 1400 nm.

1.3.3 Colloidal Quantum Dot Based Hybrid Photodetectors

There are various photon detection systems in the visible range, such as silicon detectors, photomultiplier tubes and charge-coupled device (CCD) cameras. On the contrary, infrared detection systems, especially array-based systems are quite complicated. It is because CCD arrays based on single crystal silicon cannot detect beyond 1.1 μm, and other material systems exhibit high noise levels or have high processing costs. Hence, new materials with high detectivity and reasonable cost are needed.

For application for light absorption in the NIR region, narrow bandgap inorganic quantum dots, such as PbSe, PbS, PbTe, HgTe, InAs and InSb are good candidates. Their bandgaps can be easily tuned from the visible spectral range up to 3.5 μm by exploiting the size of the QDs.

In 2006, Konstantatos et al. reported IR sensitive photodetectors based on PbS QDs [25]. Devices were fabricated by spin-casting of butylamine-treated PbS QDs on the prepatterned electrode structure. They showed high detectivity of 2X10^{13} Jones at the modulation frequency of 30 Hz, which is higher than that of commercial InGaAs

photodetectors. High photoconductive gain of 10^2 ~ 10^4 was resulted from the existence of long-living electron traps formed during chemical treatment on the QD surface.

Sargent group studied the nature of long-living traps in PbS QDs and the effect of surface sites on the response time of PbS detectors [26-28]. The treatment of QD films with different molecules can control the surface states and consequently response time. They fabricated a device with the shortest time constant of 33 ms and detectivity in excess of 10^{12} Jones by treating the films with ethanethiol in acetonitrile.

A photodiode can be operated with significantly higher response speed than a photoconductor. Sargent group reported fast and IR sensitive photodiodes based on the PbS QD film sandwiched between ITO and Al contacts [29, 30]. The operation of the device was determined by the Schottky barrier at the QD-metal interface. Since the carrier velocity in the depletion region is much higher than that in the diffusion layer, the optimal device with fast response time was obtained by adjusting the QD film thickness to form no diffusion layer. Fast operation with 3 dB bandwidth of up to 35 kHz was obtained with similar detectivities of around 10^{12} Jones to those for photoconductive detectors.

There have been several reports of photodetectors using blend of QDs with organic materials. The hybrid organic-QD devices were designed to utilize light harvesting of IR sensitive QDs and charge transport of conjugated polymers. Szendrei et al. reported IR sensitive photodetectors based on the blend of PbS QDs and PCBM polymer [31]. Compared with the poor photoresponse of oleic acid capped PbS QD films, the composite solids of 1:1 PbS QD/PCBM showed $2.5X10^{10}$ Jones. The spectral response of the devices followed the absorption spectrum of PbS QDs and the efficient

electron transfer from PbS QDs to PCBM was confirmed by time-resolved luminescence and transient absorption. The blends of oleic acid capped PbSe QDs and PVK with the EQE of 3 % [32] and the blends of PbS QDs and MEH-PPV with the IQE of 10^{-5} [33] were reported by other research groups.

1.3.4 Organic Up-Conversion Devices

Up-conversion devices are optoelectronic devices which convert low energy photons to high energy photons. Generally, these devices consist of a sensitizing part for absorbing low energy light and a light-emitting part for emitting high energy light. Since IR sensing devices have been widely researched for various applications such as night vision and security. Most IR-to-visible up-conversion devices are based on the inorganic semiconductors. Liu et al. reported an inorganic NIR-to-visible up-conversion device consisting of a light-emitting diode integrated with a photodetector, and demonstrated an inorganic/organic hybrid up-conversion device integrating an InGaAs/InP photodetector with an organic light-emitting diode. For both devices, the photon-to-photon conversion efficiencies were about 0.3 %. In addition to low efficiencies, these inorganic and hybrid up-conversion devices require complex fabrication process and high material cost.

On the contrary, organic optoelectronic devices have attracted a great deal of attention due to their compatibility with flexible substrates, low cost process and large area applications. Therefore, organic up-conversion devices have tremendous potentials as low cost IR imaging sensors. Yase et al. reported the first NIR-to-blue organic up-conversion device integrating a fluorescent OLED with titanium oxide phthalocyanine (TiOPc) photosensitive hole injection layer. However, the photon-to-photon efficiency was quite low as 0.05 % due to the inefficient charge dissociation and

radiative recombination. In our group, we demonstrated a NIR-to-green up-conversion device using a tin phthalocyanine (SnPc):C_{60} mixed layer as a NIR sensitizer and an $Ir(ppy)_3$-based OLED as a phosphorescent emitter.

1.4 Dissertation Organization

This dissertation covers topics on organic light-emitting diodes, hybrid light-emitting diodes and organic up-conversion devices.

The work on OLEDs is covered in Chapter 2 and Chapter 3. Chapter 2 focuses on the white OLEDs with red, green and blue phosphorescent dopants and their emission mechanism. Chapter 3 focuses on the $Ir(ppy)_3$-based green-emitting stacked phosphorescent OLEDs and their charge generation mechanism. The work on hybrid LEDs is covered in Chapter 4. Chapter 4 focuses on the synthesis of PbSe colloidal quantum dots and multilayer hybrid LEDs and blend hybrid LEDs employing the PbSe quantum dots and a MEH-PPV polymer. The work on infrared-to-visible up-conversion devices is covered in Chapter 5 and Chapter 6. Chapter 5 focuses SnPc:C_{60}-based organic up-conversion devices and their charge injection properties. Chapter 6 focuses PbSe QD-based hybrid up-conversion devices and their operating mechanism. Finally, the conclusion will be presented in Chapter 7.

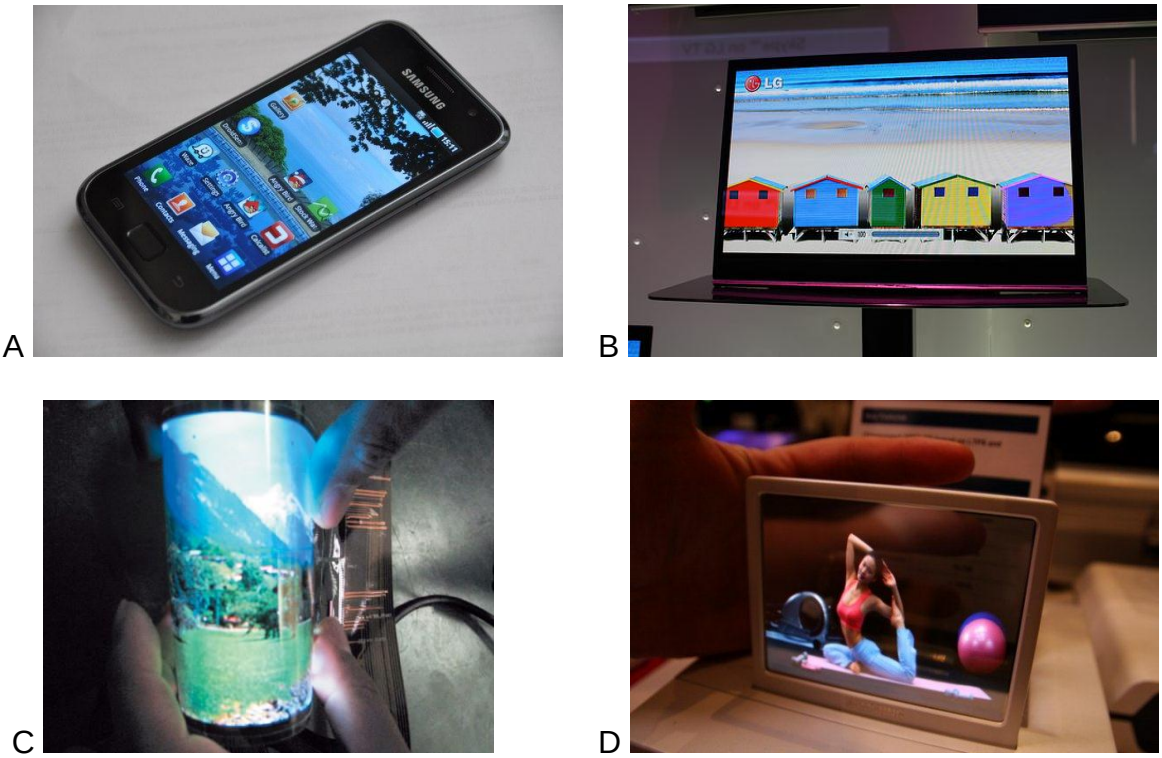

Figure 1-1. Various display applications with OLEDs: A) mobile phone (Samsung Galaxy S), B) 15'' OLED TV (LG EL9500), C) flexible display prototype (Samsung) and D) transparent display prototype (Samsung) (Adapted from http://www.oled-info.com and http://www.oled-display.net)

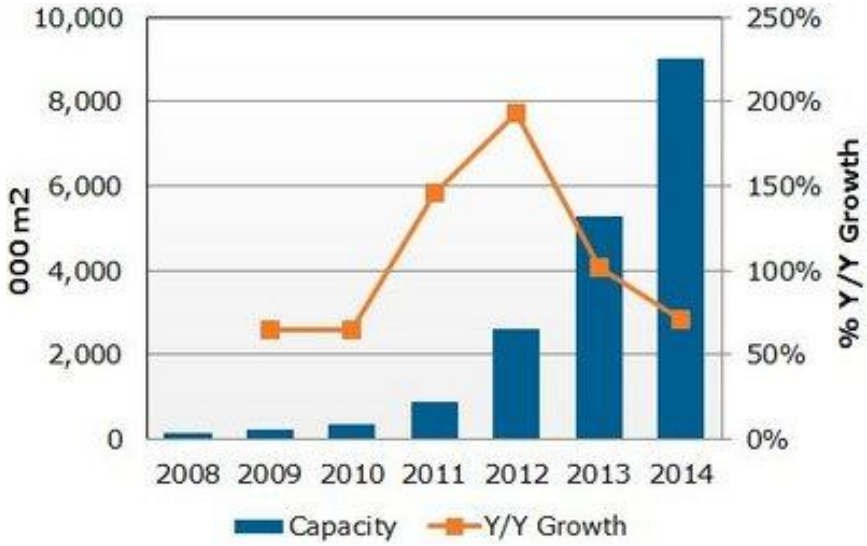

Figure 1-2. Forecast of AMOLED capacity and year-by-year growth rate (Adapted from http://www.displaysearch.com)

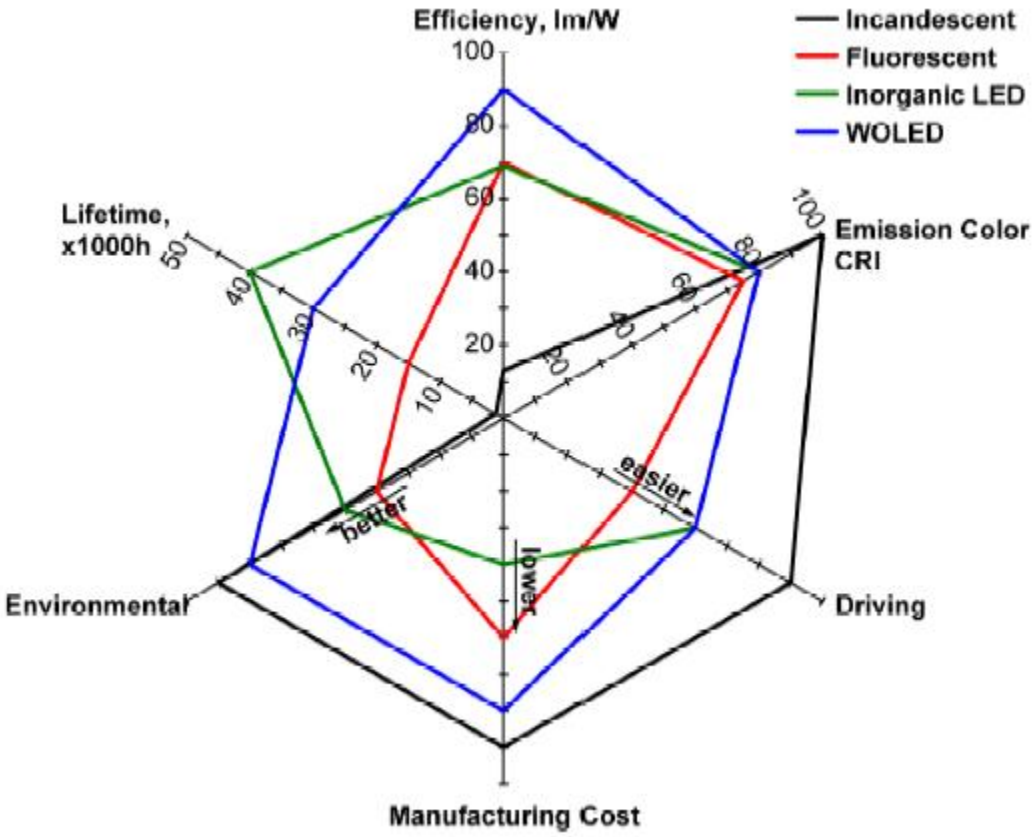

Figure 1-3. Comparison of the key-performance parameters of WOLEDs relative to incandescent lamps, fluorescent tubes and inorganic white LEDs. Data for incandescent lamps, fluorescent tubes and inorganic white LEDs is representative for commercially available light sources. WOLED parameters reflect data from different literature reports. The number for the WOLED lifetime assumes an initial luminance of 5000 cd/m^2 which generates a luminous flux equivalent to that of a 40 W incandescent light bulb (approximately 750 lm) if a WOLED with a size of 22X22 cm^2 is used. (Adapted from [4])

Figure 1-4. Various luminaires with OLEDs panels demonstrated by OLED lighting companies: A) Philips, B) Osram, C) General Electric and Konica Minolta, D) Novaled and E) LG Chem. (Adapted from http://www.oled-info.com)

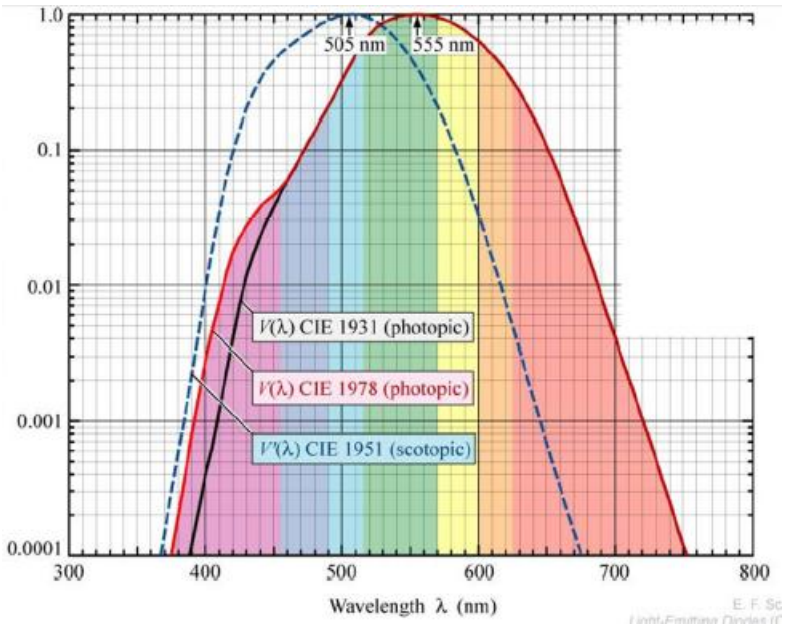

Figure 1-5. Comparison of eye sensitivity functions for the photopic and scotopic vision regime. (Adapted from [9])

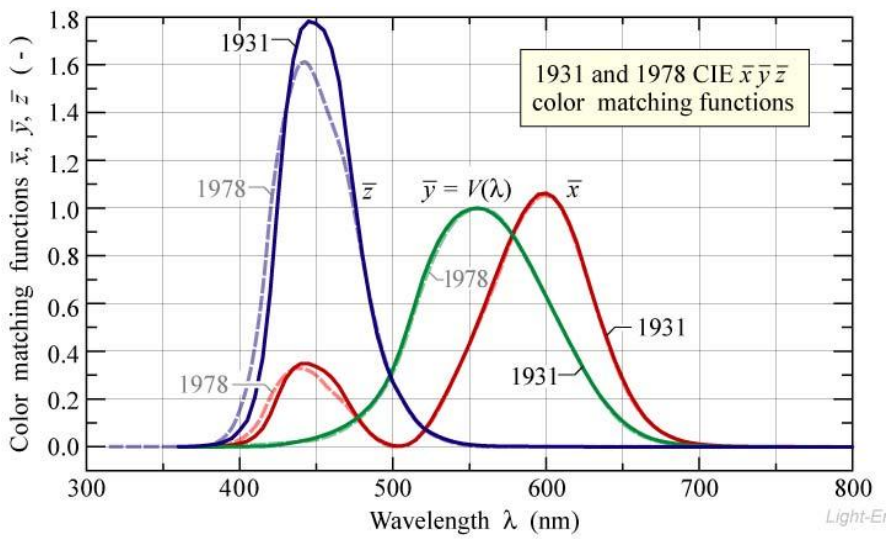

Figure 1-6. CIE (1931) and CIE (1978) xyz color matching functions (CMFs). Note that the CIE 1931 CMF is the currently valid official standard. (Adapted from [9])

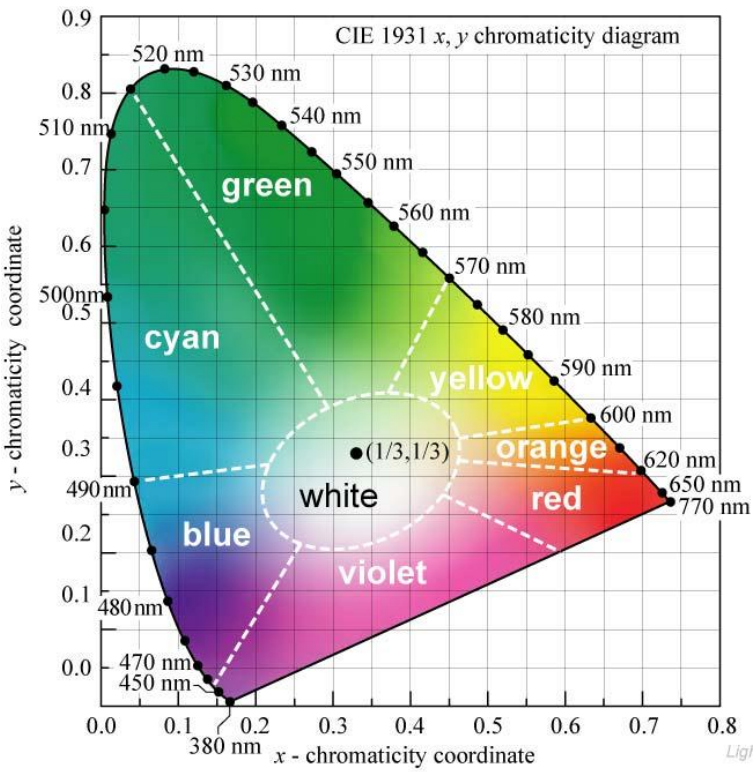

Figure 1-7. CIE 1931 (x, y) chromaticity diagram. White light is located in the center. Also shown are the regions of distinct colors. (Adapted from [9])

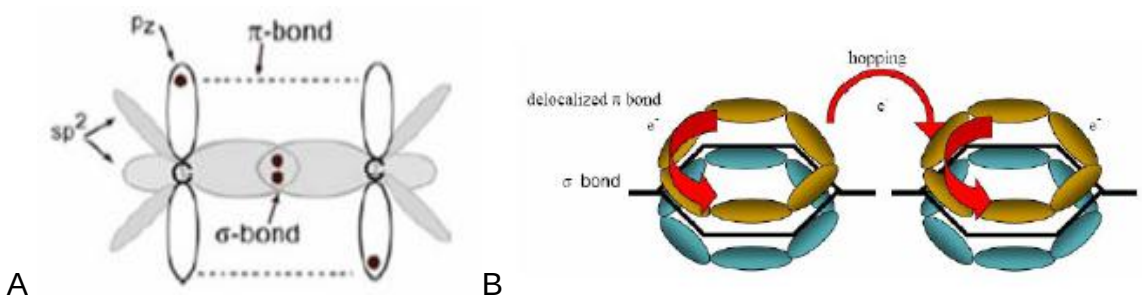

Figure 1-8. Schematic drawing of electronic states of organic semiconductors: A) strong σ-bond between sp^2 hybridazation and weak π-bond between p_z orbitals, and B) hopping process for intermolecular electron transporting in conjugated organic molecules.

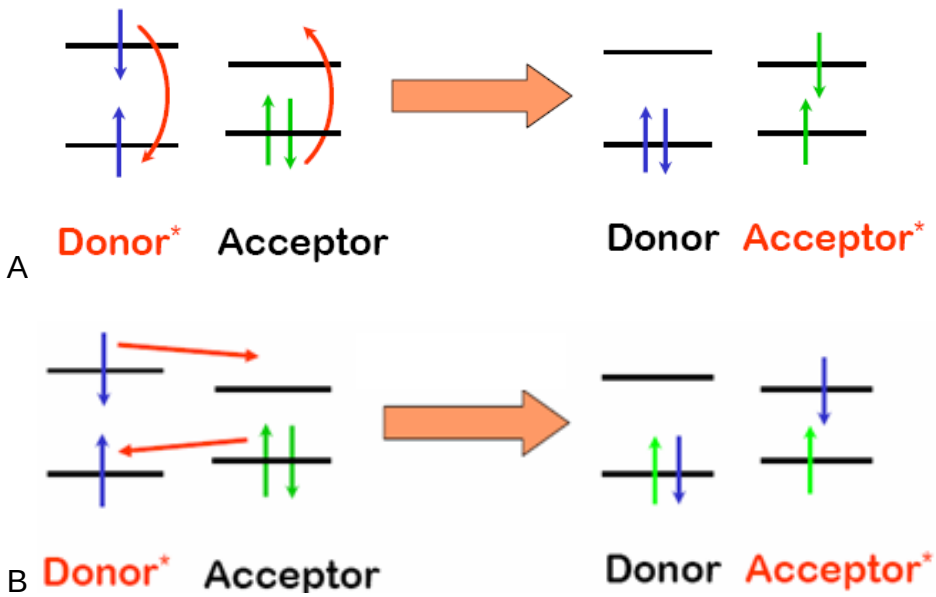

Figure 1-9. Schematic drawing of non-radiative inter-molecular energy transfer processes: A) Förster energy transfer with long range transition and B) Dexter energy transfer with short range transition.

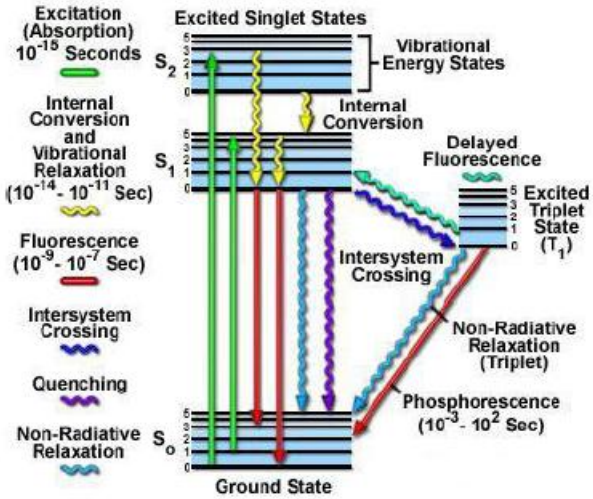

Figure 1-10. Schematic illustration of Jablonski energy diagram (Adapted from http://micro.magnet.fsu.edu/optics/timeline/people/jablonski.html). The absorption process is represented from the ground state (S_o) to the excited state ($S_{1\ or\ 2}$), and radiative transitions are represented as fluorescence (S_1 to S_o) and phosphorescence (T_1 to S_o). Nonradiative transitions such as internal conversion, vibrational relaxation, quenching, and intersystem crossing are also represented.

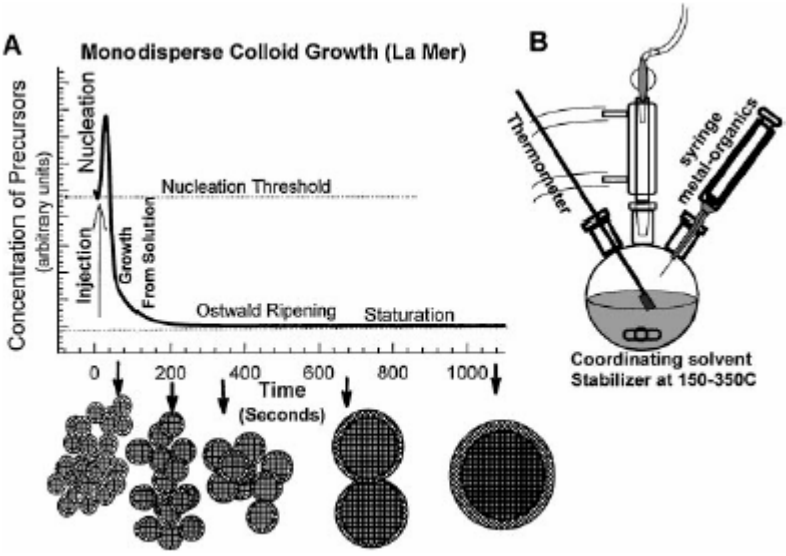

Figure 1-11. Schematic illustration of the preparation of monodisperse QDs based on La Mer model: A) Schematic diagram of the nucleation and growth of QDs. As QDs grow with time, a series of QDs with different sizes can be isolated by removing aliquots from the reaction vessel. B) Schematic drawing of the QD synthetic apparatus. (Adapted from [18])

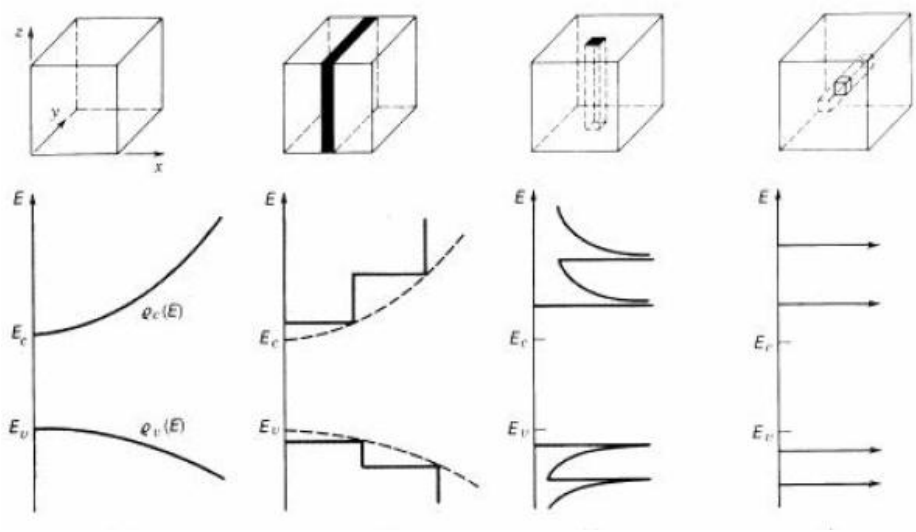

A B C D

Figure 1-12. Schematic comparison of quantization of density of states: A) bulk, B) quantum well, C) quantum wire and D) quantum dot. (Adapted from [34])

CHAPTER 2
WHITE PHOSPHORESCENT ORGANIC LIGHT-EMITTING DIODES

2.1 Background and Motivation

The need for new types of general lighting is globally accepted due to low efficiency of incandescent bulbs and pollution issue of fluorescent lamps. Therefore, tremendous research activities on solid state lighting such as light-emitting diodes (LEDs) and organic light-emitting diodes (OLEDs) have been performed. In order to compete with the high efficiency of semiconductor LEDs, the improvement on the efficiency of white organic light-emitting diodes (WOLEDs) should be preceded. For designing the efficient white OLEDs, the thorough understanding of the emission mechanism in the devices is crucial. Although there are a lot of works on high efficiency WOLEDs in both academia and industry [6-8], studies on emission mechanism of WOLEDs are much fewer than the device works. While OLEDs are commonly characterized by simple L-I-V measurement and spectrum measurement, previous studies on emission mechanism in white OLEDs were mainly based on more complex characterization methods, such as time-resolved or temperature-dependent spectroscopy measurements [8, 35].

In this work, we designed and demonstrated a series of multiple emissive layer white OLEDs. Emission mechanism in the devices was analyzed based on the data characterized by L-I-V measurement and EL measurement. Also, according to the understanding of the emission mechanism, an efficient white OLED with reduced energy losses and high color rendering index (CRI) was designed.

2.2 Experimental Details

The white phosphorescent organic light-emitting diodes were fabricated on glass substrates precoated with ITO transparent conducting electrode with a sheet resistance of 20 Ω per square. The substrates were cleaned with acetone and isopropanol in an ultrasonic cleaner and subsequently rinsed with de-ionized water, blown dry with N_2 gas, and treated with UV-ozone. All organic layers and a LiF/Al cathode layer in the devices were thermally evaporated at a pressure of around $1*10^{-6}$ torr. Energy levels of all the materials in this study were summarized in Figure 2-1. Di-[4-(N,N-ditolyl-amino)-phenyl]cyclohexane (TAPC) and tris[3-(3-pyridyl)mesityl]borane (3TPYMB) were used as a hole and an electron transporting layer, respectively. 1,3-bis(carbazol-9-yl)benzene (mCP) and 2,2',2''-(1,3,5-benzinetriyl)-tris(1-phenyl-1-H-benzemidazole) (TPBi) were used as a hole and an electron transporting host, and they were doped with phosphorescent emitting dopants of bis(2-methyl-dibenzo[f,h]quinoxaline)(acetylacetonate)iridium (III) ($Ir(MQD)_2(acac)$), tris(2-phenylpyridine)iridium(III) ($Ir(ppy)_3$), and iridium (III) bis[(4,6-difluorophenyl)pyridinato]picolinate (Firpic). The active area of the device is 2X2 mm^2.

Luminance-current-voltage (L-I-V) characteristics of the OLEDs were measured using a Keithley 2400 source meter for current voltage measurements coupled with a Keithley 6485 picoammeter connected to a calibrated Si photodiode for photocurrent measurements. The data was acquired using LabView interface, and the photocurrents are converted to cd/m^2 using calibrated conversion factors. The measurements were carried out at room temperature under an ambient atmosphere. The EL spectra were

collected using an Ocean Optics HR4000 high-resolution spectrometer. All EL spectra were measured and compared at 1 mA/cm^2 unless otherwise noticed.

2.3 Results and Discussion

2.3.1 Red-Blue Double Emissive Layer White OLEDs

Instead of using pure red and blue emitting dopants, orange emitting $Ir(MDQ)_2(acac)$ and sky-blue emitting Firpic were chosen as emitting dopants due to the advantage for lighting application [8]. The spectra of the monochromatic devices with $Ir(MDQ)_2(acac)$ and Firpic were shown in Figure 2-6. However, to simplify the expression of the device architecture, we will name $Ir(MDQ)_2(acac)$ and Firpic as a red and a blue dopant, respectively. Figure 2-2B shows the electroluminescence spectra of the white OLEDs with various concentrations of $Ir(MDQ)_2(acac)$. Firpic was doped with 20 wt. % in mCP for all devices. Significant change in EL spectra was observed with varying the red doping concentrations. As the doping concentration of red dopants increased, the relative intensity of red emission increased. With 5 wt. % of $Ir(MDQ)_2(acac)$ doping, the spectrum from blue and red emission was well balanced and showed the maximum value of CRI of 67.7 among those devices. This CRI value is still low for general lighting application (>80) and low CRI is attributed to the lack of the emission of green light.

Figure 2-3A and B show current density and luminance as a function of voltage with various $Ir(MDQ)_2(acac)$ doping concentrations. At the range of 3 to 10 wt. % of doping concentrations, the difference in current densities between the devices is not significant. However, clear difference of the EL efficiencies is observed, shown in Figure 2-3C. At low current densities, the peak power efficiency increases as the concentration of the red dopants is decreased from 10 to 5 wt. %, and reduces with further decrease

in doping concentration to 3 wt. %. On the other hand, at high current densities, the power efficiency increases with decreasing the doping concentration. More significant difference in current efficiencies is observed with various doping concentrations. The current efficiency increases with decreasing the doping concentrations. The peak EQE also increases from 17.2 % to 18.7 %, as the doping concentration is decreased, indicating better charge balance in the devices with lower $Ir(MDQ)_2(acac)$ concentration. This implies that the presence of $Ir(MDQ)_2(acac)$ can affect the transport of charged carriers and the possible mechanism will be discussed in Chapter 2.3.3.

2.3.2 Red-Blue-Green Triple Emissive Layer and Red-Blue-Blue-Green Quadruple Emissive Layer White OLEDs

Low CRI from double emissive layer WOLEDs without green emitters were shown in Chapter 2.3.1. In order to improve the CRI value, we fabricated triple emissive layer white OLEDs consisting of red, blue and green emitting dopants. $Ir(ppy)_3$ was used as a green dopants. Figure 2-4A shows the schematic drawing of the device architecture. For the doping concentrations of dopants, 10 wt. % of $Ir(MDQ)_2(acac)$, 20 wt. % of Firpic and 5 wt. % of $Ir(ppy)_3$ were used.

First, the triple emissive layer white OLEDs with red, blue and green sequence (R-B-G WOLEDs) were used. Due to the hole transporting property of mCP and electron transporting property of TPBi, both charge carriers are accumulate at the interface between blue emitting layer consisting of mCP:Firpic and TPBi, resulting in the formation of excitons. Figure 2-4B shows the EL spectra of triple emissive of R-B-G WOLEDs. The device with a 2 nm thick mCP interlayer between red and blue emitting layers, only green emission is dominant. It is attributed to the significant energy/charge transfer to green dopants due to small distance between the main exciton generation

interface and the green emitting layer. The device without mCP interlayer between red and blue emitting layers, red emission is enhanced, but green emission is still dominant and blue emission is drastically suppressed. CRI is 59.3 at 1 mA/cm^2 due to the dominant green emission. In order to achieve better balanced emission from three colors, green emission should be suppressed and blue emission should be enhanced.

To suppress green emission and enhance blue and/or red emission, quadruple emissive layer white OLEDs with red, blue, blue and green sequence (R-B-B-G WOLEDs) were designed. Figure 2-5A shows the schematic drawing of the quadruple WOLEDs. If the distance is increased between the main exciton generation interface to the emitting layer, emission is expected to be reduced due to the suppressed the energy/charge transfer. Figure 2-5B shows the EL spectra of the quadruple WOLEDs. First, 6 wt. % of $Ir(MDQ)_2(acac)$, 20 wt. % of Firpic and 3 wt. % of $Ir(ppy)_3$ were used as doping concentrations in hosts materials. 2 nm thick of mCP was inserted between red and blue emission layer, and 2 nm thick of TPBi was inserted between blue and green emission layer. Since Firpic dopants were deposited with a hole transporting host mCP in the first blue emitting layer and were deposited with an electron transporting host TPBi in the second blue emitting layer, the main exciton generation interface was positioned within the two blue emitting layers, resulting in the increased portion of blue emission. Also, since the distance between the main exciton generation interface and the green emitting layer is increased, reduced green emission can be achieved from the device architecture as expected. However, the ratio of red emission to green emission is still low with 6 wt. % doping concentration of $Ir(MDQ)_2(acac)$.

Hence, we increased the doping concentration of $Ir(MDQ)_2(acac)$ from 6 to 10 wt. % to obtain more red emission. As shown in Figure 2-5B, the relative increment in red emission is not significant as the doping concentration increased. On the contrary, green emission is still dominant regardless of doping concentration of red dopants, although same thickness of interlayer was used for each side. It implies that the emission mechanism and charge/energy transfer from high energy emission (blue) to low energy emission (red or green) for red emission and green emission might be different.

2.3.3 Emission Mechanism in Multiple Emissive Layer White OLEDs

To study the emission mechanism of multiple emissive layer WOLEDs further, a series of devices were designed. Figure 2-7A shows the schematic drawing of the device structures for the study. As a control device, a quadruple emissive layer white OLED with red, blue, blue and green sequence (R-B-B-G WOLEDs) was fabricated. In order to study the charge/energy transfer between dopants, we made the devices with blue doping in merely a single carrier transport host, also shown in Figure 2-7A. Figure 2-6A-D shows the electroluminescence spectra of blue, green, red, and white control OLEDs, respectively.

The triplet excited states of the phosphorescent dopants in OLEDs can be generated through three routes: direct charge trapping of carriers, Förster energy transfer followed by intersystem crossing and Dexter energy transfer. Apart from other two routes, generation of triplet excited states through direct charge trapping of carriers changes the overall current level in the device, and thus it can be distinguished by analyzing I-V characteristics. As the main exciton generation interface lies within the blue emitting layer, blue emission is likely to follow the well-known host-to-guest energy

transfer. On the contrary, red and green emission from the control white OLED should be followed by direct charge trapping or intermolecular exciton energy transfer, but it cannot be distinguished by analyzing the device behavior of only a single control white OLED.

First, to investigate the charge/energy transfer between red and blue dopants, we remove the blue doping in mCP layer. Without Firpic doping in mCP, significant reduction in red emission was observed. Both direct charge trapping and two types of exciton energy transfer from the blue dopant to the red dopant can be affected by the presence of Firpic in mCP host. Dexter energy transfer seems negligible in the control white OLED because it is short range order transfer (~1 nm) and there is 2 nm mCP interlayer between blue emitting layer and red emitting layer. Förster energy transfer is also unlikely to be dominant because the spectral overlap between Firpic emission and $Ir(MDQ)_2(acac)$ absorption is insignificant. Therefore, red emission is attributed to direct exciton generation from trapped holes in $Ir(MDQ)_2(acac)$ and transported electrons through Firpic in mCP. As illustrated in Figure 2-8, based on the LUMO levels of TPBi and Firpic and HOMO levels of TAPC and $Ir(MDQ)_2(acac)$, electron trapping and transfer through Firpic and hole trapping and transfer through $Ir(MDQ)_2(acac)$ is preferable, rather than through mCP host.

In order to examine the charge/energy transfer between blue and green dopants, we remove the blue doping in TPBi layer. Direct trapping or two types of exciton energy transfer from Firpic to $Ir(ppy)_3$ should be affected by the presence of the Firpic in TPBi host, since Firpic in TPBi can form hopping sites for holes and shorted distance between blue and green dopants. However, without Firpic doping in TPBi, no change in

the ratio of blue to green emission was observed. It means that Firpic doped in TPBi does not significantly contribute to the charge/energy transfer to the green dopants. In other words, the direct energy transfer or direct charge trapping from Firpic dopants in TPBi layer to the $Ir(ppy)_3$ emission is negligible, and the generated excitons at the main exciton generation interface diffuse through the TPBi host to the green emission layer. The triplet exciton states can be formed by energy transfer from TPBi host to $Ir(ppy)_3$ guest, followed by the green emission due to the charge recombination.

In order to see the effect of red and green dopants on the exciton harvesting, we compared the current density and EQE of the R-B-B-G WOLED with those of the devices without one color dopant. Significant changes in current density with the presence of the red dopant were observed. With the red dopant, hole injection into the emitting layers is enhanced through $Ir(MDQ)_2(acac)$ molecules. As we discussed earlier, direct charge trapping affect the device I-V characteristics, and thus it can be also the evidence that red emission is mainly attributed to the direct charge trapping. The increase in EQE in a triple emissive layer device was observed, compared with double emissive layer devices. Thus, exciton loss is reduced by harvesting excitons by red and green dopants.

Based on the understanding for the emission mechanism in multiple emissive layer white OLEDs, we designed a device structure for good color balance. Figure 2-10A shows the schematic device structure of the WOLED. We put 2 nm TPBi between red and blue emission layer to flow more electrons into the red emitting layer, leading to the increase in red emission and reduction in blue and green emission relatively. The

device shows warm white with CRI value of 82.5 and CCT of 2650. The peak current and power efficiency were observed as 40 cd/A and 30 lm/W, respectively.

2.4 Summary

In summary, we study on the emission mechanism in white OLEDs. We fabricated double, triple, and quadruple emissive layer WOLEDs, focusing the color balance by controlling the doping concentrations and the distance between the emissive layer and main exciton generation interface. The emission mechanism in WOLEDs was studied from simple EL measurements with changing device configurations. In the triple emissive layer white OLEDs, we found that red emission is attributed to direct exciton generation from hole trapping on the red dopant and electron transporting through Firpic in mCP, and green emission is attributed to energy transfer from TPBi host to $Ir(ppy)_3$ guest. The understanding of the emission mechanism helps us to design efficient WOLEDs with the peak power efficiency of 30 lm/W and high CRI of 82.

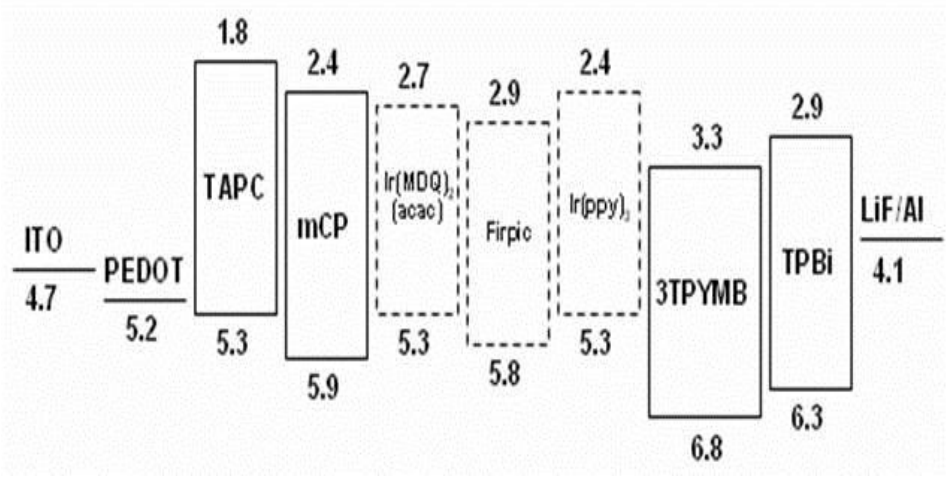

Figure 2-1. Energy level diagram of materials used in this study. (solid boxes : hosts or transporting layers, dashed box : dopants)

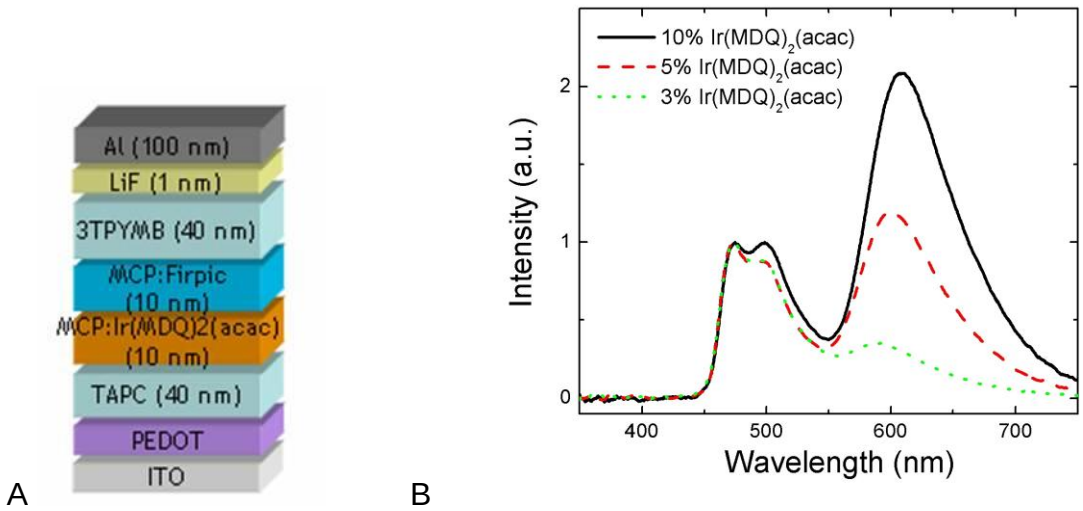

Figure 2-2. Device structure and electroluminescence spectra of R-B double emissive layer white OLEDs: A) schematic diagram of the device structure and B) EL spectra of double emissive layer white OLEDs.

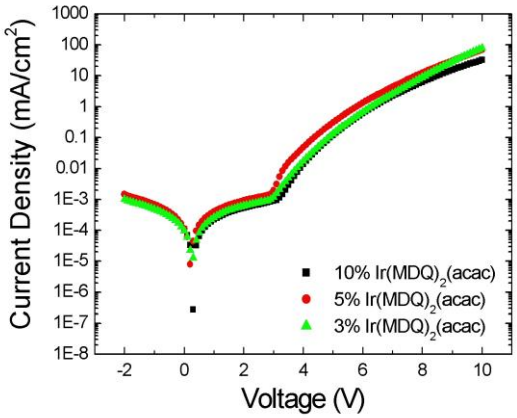

A

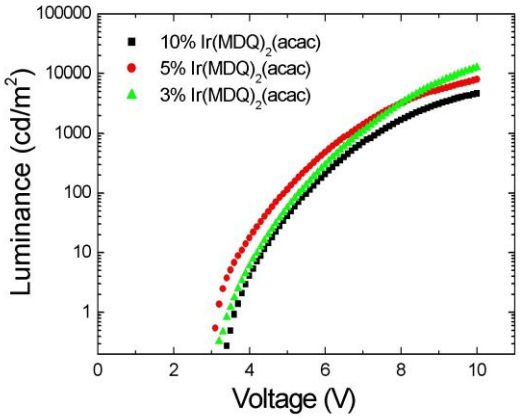

B

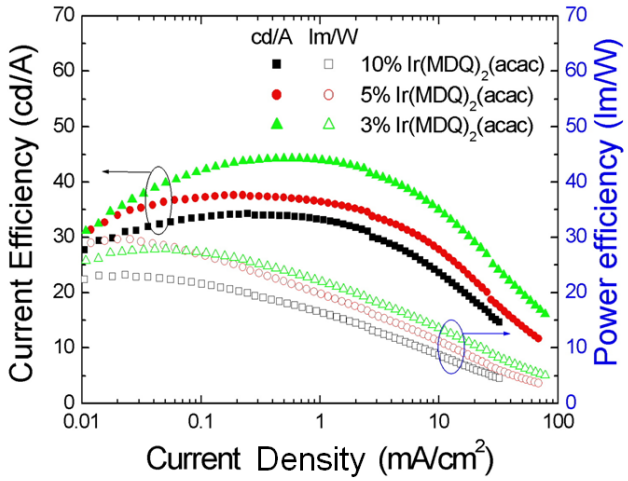

C

Figure 2-3. L-I-V characteristics and efficiencies of double emissive layer white OLEDs: A) Current density plots and B) luminance plots as a function of voltage and C) EL efficiencies as a function of current density of double emissive layer white OLEDs.

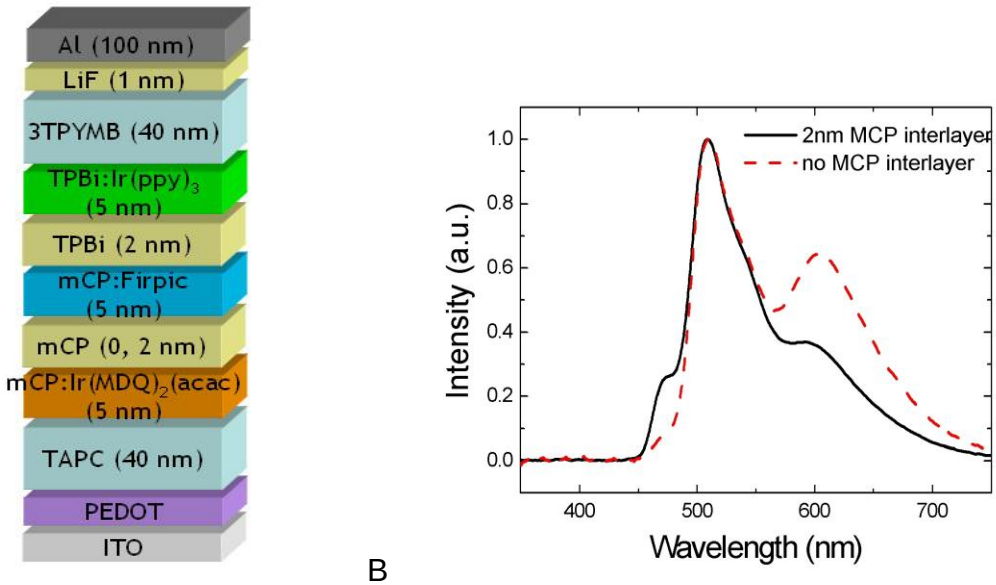

A B

Figure 2-4. Device structure and electroluminescence spectra of R-B-G triple emissive layer white OLEDs: A) schematic diagram of the device structure and B) EL spectra of triple emissive layer white OLEDs with different presence of mCP interlayer.

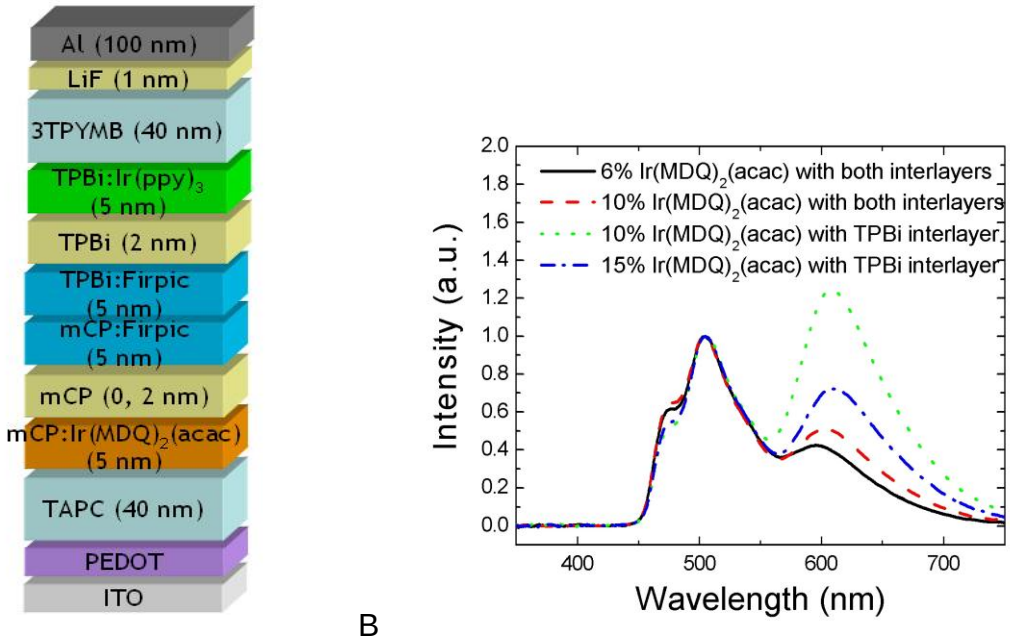

A B

Figure 2-5. Device structure and electroluminescence spectra of R-B-B-G quadruple emissive layer white OLEDs: A) schematic diagram of the device structure and B) EL spectra of quadruple emissive layer white OLEDs with various $Ir(MDQ)_2(acac)$ doping concentrations and different presence of interlayers.

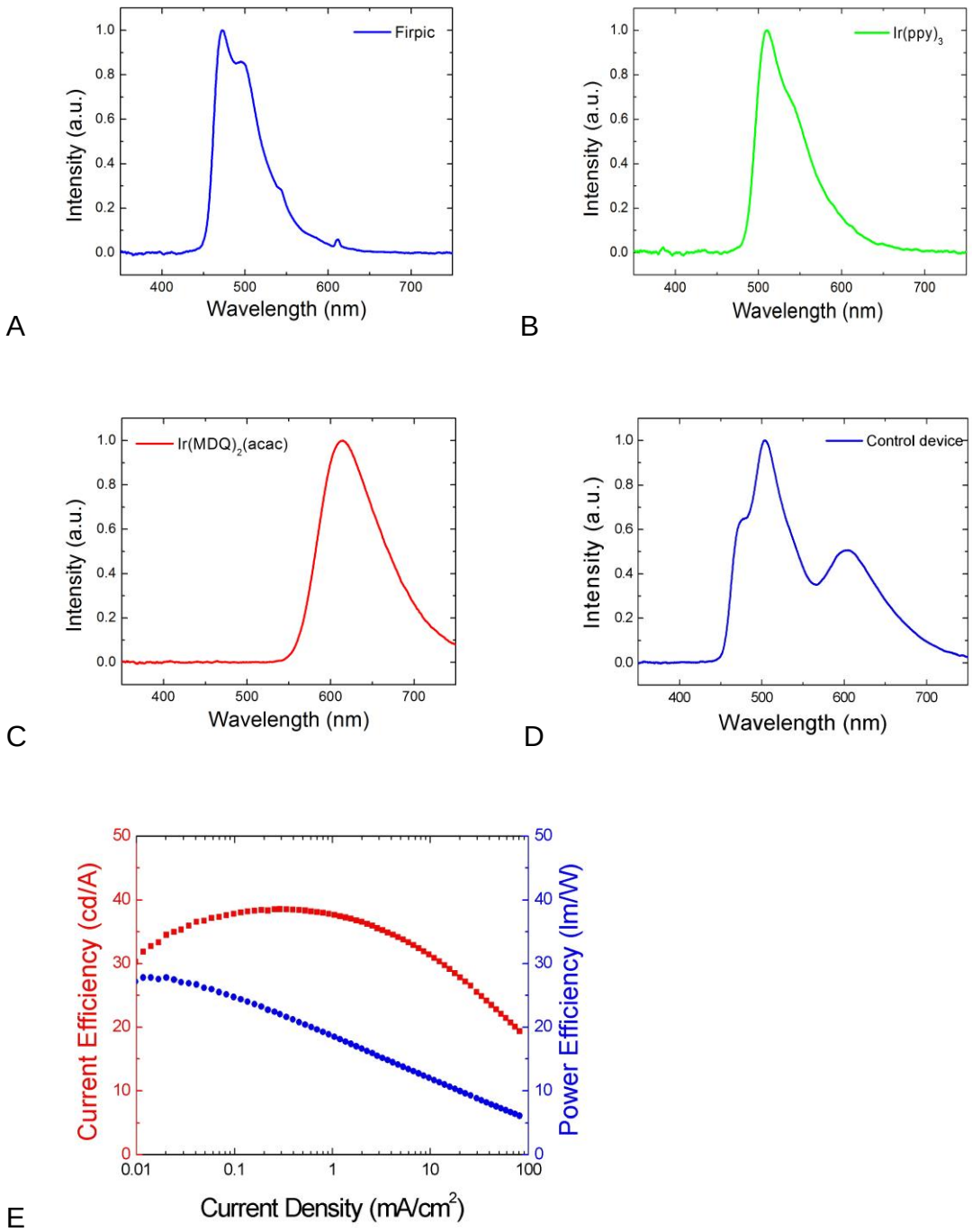

Figure 2-6. Electroluminescence spectra of monochromatic and white OLEDs and efficiencies of white OLEDs: A), B), C), D) EL spectra of blue, green, red and control white OLEDs, respectively, and E) current efficiency and power efficiency plots of the control white OLED as a function of current density.

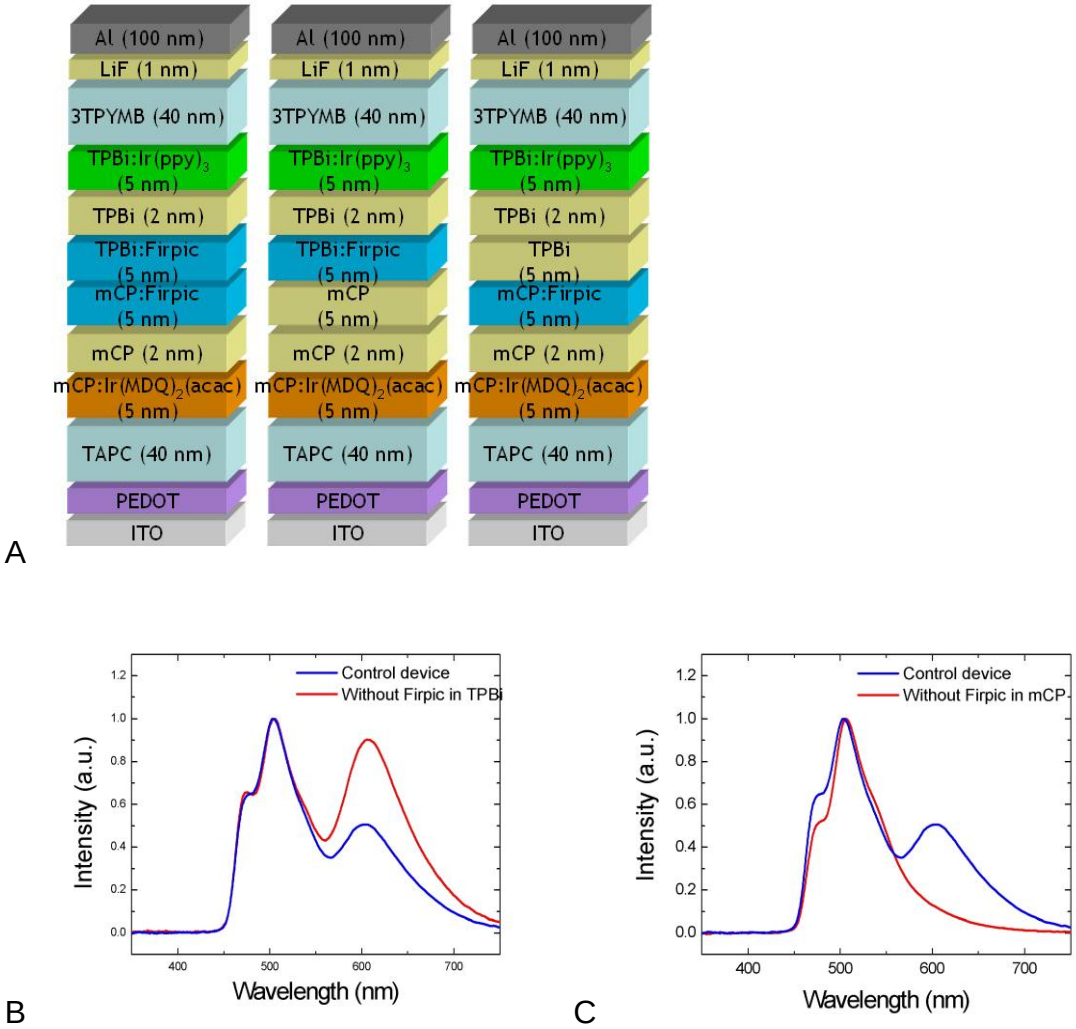

Figure 2-7. Device structure and electroluminescence spectra of devices for the investigation of emission mechanism: A) schematic diagram of the device structures, B) EL spectrum of triple emissive layer OLEDs with Firpic doping in electron-transporting side only and C) EL spectrum of triple emissive layer OLEDs with Firpic doping in hole-transporting side only, comparing with the control white OLED.

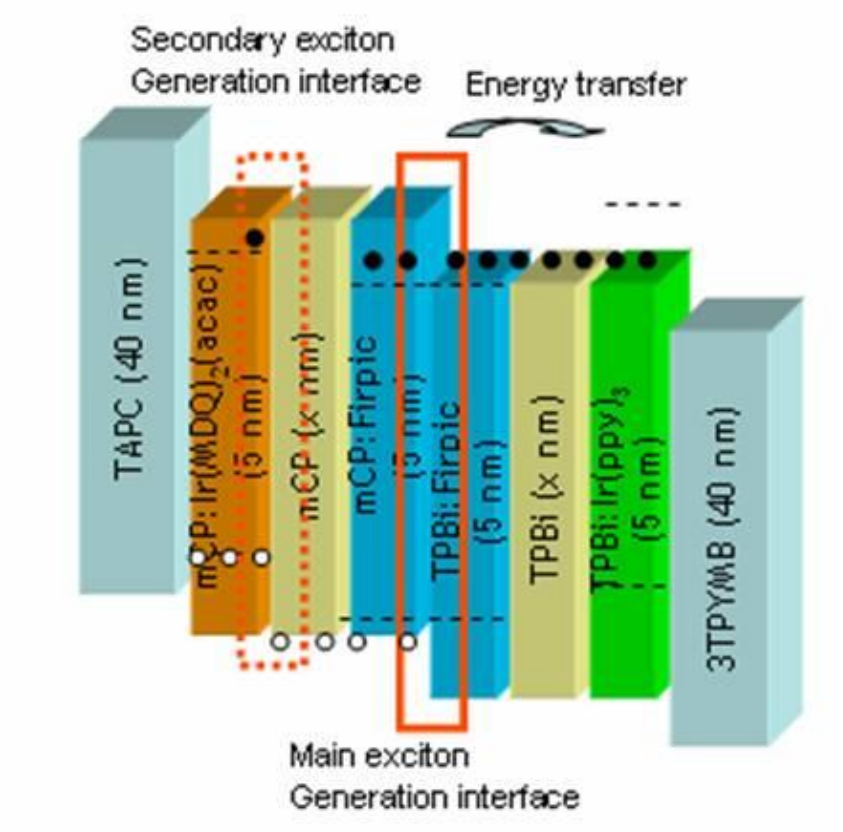

Figure 2-8. Schematic illustration of emission mechanism in R-B-B-G quadruple emissive layer WOLEDs.

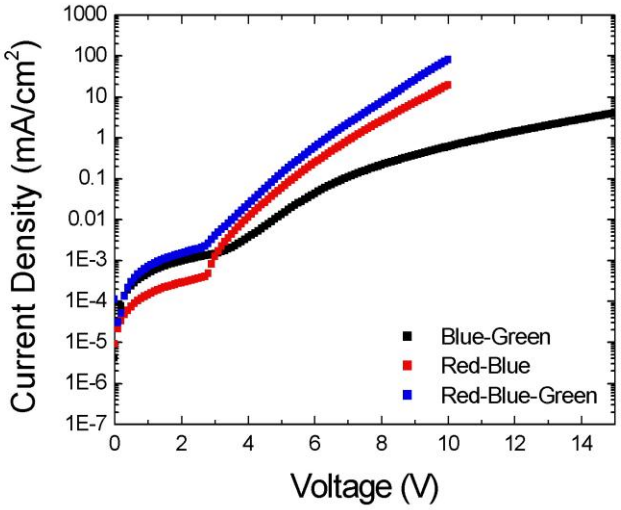

A

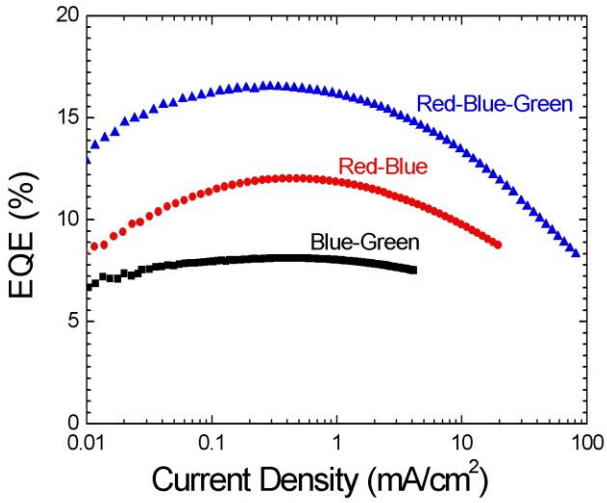

B

Figure 2-9. Comparison of I-V characteristics and efficiencies of double and triple emissive layer OLEDs: A) Current density plots as a function of voltage and B) external quantum efficiency plots as a function of current density of double emitting layer OLEDs and a triple emitting layer OLED.

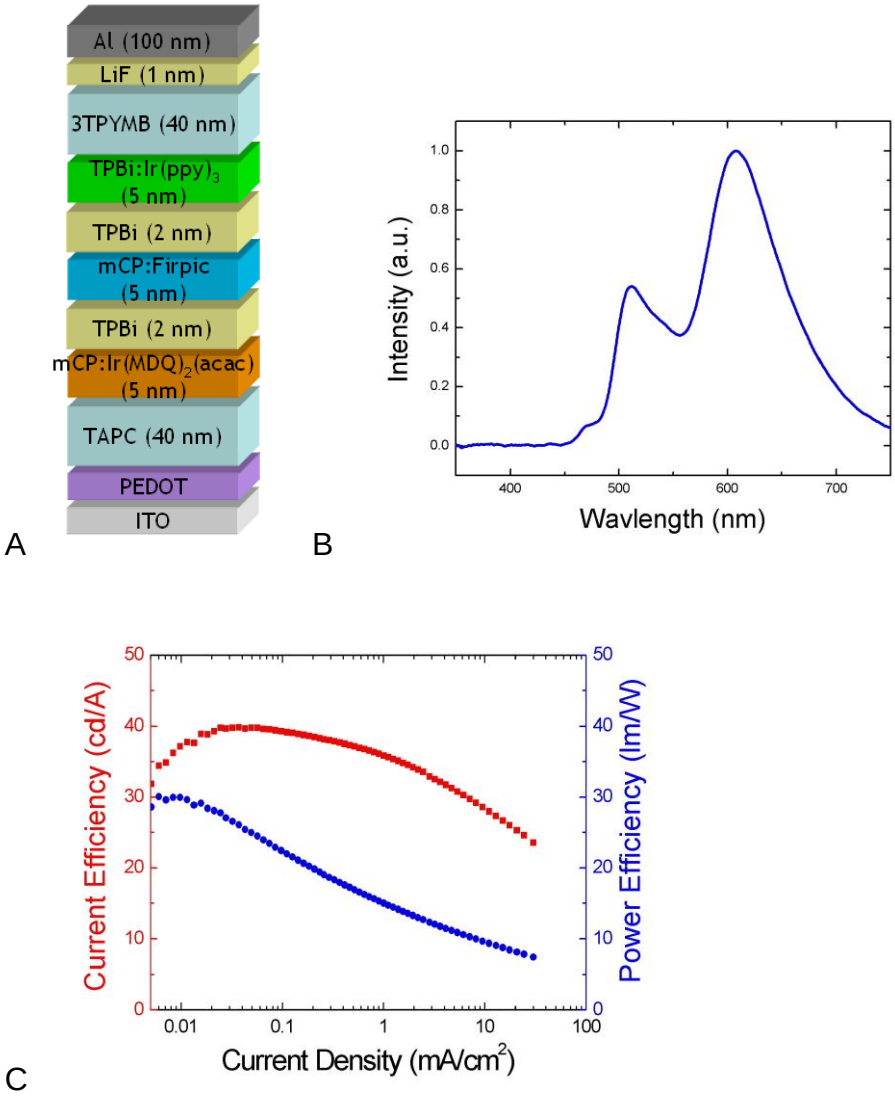

Figure 2-10. Device structure, EL spectra and efficiencies of R-B-G triple emissive layer white OLEDs with balanced emission: A) schematic diagram of the device structure, B) EL spectra and C) current efficiency and power efficiency plots as a function of current density of triple emissive layer white OLEDs

CHAPTER 3
GREEN PHOSPHORESCENT STACKED ORGANIC LIGHT-EMITTING DIODES

3.1 Background and Motivation

In recent years, stacked or tandem OLEDs have been widely researched for providing high luminance with enhanced current efficiency or for controlling the emission spectra of devices with stacked units emitting different colors [36, 37]. Stacked OLEDs consist of two or more emitting units, connected by charge generating interconnecting units. In order to achieve efficient stacked OLEDs, proper design of the charge generation layers is crucial based on the understanding of the charge generation mechanism. Among various charge generation units, two types of charge generation interconnecting layers are widely accepted in stacked OLEDs. One consists of the connection of p-doping organic layer and n-doping organic layer [37-40], and the other is n-doping organic layer connected to highly electron accepting layers such as metal oxides [41-43] or 1,4,5,8,9,11-hexaazatriphenylene-hexacarbonitrile (HAT-CN) [44, 45]. However, although there have been a lot of works on stacked OLEDs, there are only a few studies on the charge generation in stacked OLEDs [39, 40, 46].

In this work, we systematically studied the charge generation in charge generation units. First, a series of devices were designed to study charge generation operation in charge generation units and compared each other. Next, based on the charge generation study, a series of stacked OLEDs were fabricated and analyzed.

3.2 Experimental Details

The green phosphorescent stacked organic light-emitting diodes were fabricated on glass substrates precoated with ITO transparent conducting electrode with a sheet resistance of 20 Ω per square. The substrates were cleaned with acetone and

isopropanol in an ultrasonic cleaner and subsequently rinsed with de-ionized water, blown dry with N_2 gas, and treated with UV-ozone. All organic layers, interconnecting units and a LiF/Al cathode layer in the devices were thermally evaporated at a pressure of around $1*10^{-6}$ torr. N,N'-bis(naphthalen-1-yl)-N,N'-bis(phenyl)-benzidine (NPB) and TAPC were used as hole transporting layers, and 3TPYMB and bathophenanthroline (BPhen) were used as electron transporting layers. CBP was used as a host material for a green emitting layer, and it was doped with a phosphorescent emitting dopant of $Ir(ppy)_3$. The interconnecting unit consists of Cs_2CO_3 doped BPhen/Al/1,4,5,8,9,11-hexaazatriphenylene-hexacarbonitrile (HAT-CN) or MoO_3/NPB or TAPC. The active area of the device is 2X2 mm^2.

Luminance-current-voltage (L-I-V) characteristics of the OLEDs were measured using a Keithley 2400 source meter for current voltage measurements coupled with a Keithley 6485 picoammeter connected to a calibrated Si photodiode for photocurrent measurements. The data was acquired using LabView interface, and the photocurrents are converted to cd/m^2 using calibrated conversion factors. The measurements were carried out at room temperature under an ambient atmosphere. The EL spectra were collected using an Ocean Optics HR4000 high-resolution spectrometer.

3.3 Results and Discussion

3.3.1 Study of Charge generation Units in Stacked Organic Light-Emitting Diodes

In order to assess the operation of charge generation units in stacked OLEDs, we designed a series of charge generation devices. Figure 3-1A and B show the schematic device structures for the charge generation study, and their device operation with forward bias. To prevent the charge injection from both electrodes at forward bias, we put 3TPYMB as an electron transporting layer with deep HOMO level on ITO anode and

Al cathode on TAPC as a hole transporting layer with shallow LUMO level. Without any charge generation units in the device, current level remains very low due to the prevented charge injection from the electrodes. On the contrary, the devices with a charge generation unit show significant current generation in the device.

In order to assess the efficiency of the charge generation for the charge generation units further, a series of devices with various charge generation units were compared. MoO_3 and HAT-CN were used as n-type electron accepting layers and TAPC was used as a hole transporting and electron donating layer. For the efficient charge generation in the charge generating interface, small energetic barrier between HOMO level of the hole transporting layer and LUMO level or CBM of the electron accepting layer. As shown in Figure 3-2, the charge generation occurs from around 3 V for both devices with MoO_3 and HAT-CN electron accepting layers, while the device with HAT-CN showed a little higher than that with MoO_3. MoO_3 and HAT-CN are known as efficient electron acceptors due to their deep CBM or LUMO level. The energy level diagram of the charge generation interconnecting layers, similar to our structure, consisting of n-doped electron transporting layer/metal oxide electron accepting layer/hole transporting layer was proposed [47, 48]. Thus, the charge generation is efficient enough with both electron accepting materials and the overall current from the charge generation is dependent on the effectiveness of electron tunneling through the Cs_2CO_3 doped BPhen layer, as illustrated in Figure 3-3.

In order to investigate the dependence of doping concentration of Cs_2CO_3 in BPhen on the current density in the charge generation devices, we changed the doping concentration of Cs_2CO_3 in BPhen. Figure 3-4 shows the current density as a function of

voltage with various doping concentration of Cs_2CO_3. As the doping concentration of Cs_2CO_3 increased from 2 vol. % to 4 vol. %, the current density started to decrease. Even with 10 vol. % of Cs_2CO_3 doping, the current density decreased by around 3 orders of magnitude. To understand the origin of the strong dependence of current density on the doping concentration, we should study the energy band structure in the interconnecting unit.

Figure 3-3 shows the schematic energy band diagram of the interconnecting unit. Electrons formed at the interface between an electron accepting layer and a hole transporting layer flow toward the anode with forward bias, and they can penetrate through steep energy barrier by tunneling. It means the overall current flow is dependent how effectively electrons can penetrate this tunneling barrier, assuming charge generation is efficient. The steep energy barrier is caused by the depletion of the extrinsic free electrons due to the strong electron affinity of the adjacent electron accepting material. In other words, the tunneling depth of the BPhen layer is strongly dependent on the effectiveness of extrinsic electron flow, if sufficient electrons are supplied by doping. It is reported that higher molar concentration of Cs_2CO_3 in BPhen up to 10 % molar concentration exhibits the increase in doping effect, but it starts to saturate more than around 10 mol. % [49]. Due to lower density of BPhen (1.21 g/cm^3) transporting material than Cs_2CO_3 dopant (4.07 g/cm^3) with similar molecular weights (332.4 g/mol for BPhen and 325.8 g/mol for Cs_2CO_3), 2, 4 and 10 vol. % of Cs_2CO_3, corresponds to 6.5, 12.5 and 27.6 mol. % of Cs_2CO_3, respectively. Within this range of Cs_2CO_3 concentrations, band shift in BPhen should be less than 0.5 eV, and thus the

direct effect of Cs_2CO_3 doping concentration on the band bending should not be significant.

It should be noted that we inserted very thin (~1 nm) Al interlayer between n-doped electron transporting layer and electron accepting layer to improve the electrical conductivity and to facilitate the electron tunneling. However, since Cs_2CO_3 is not elemental metal, anions of Cs_2CO_3, such as CO_3^{2-} and O^{2-}, are likely to react with Al, and to form insulating compounds. With excessive doing of Cs_2CO_3, more insulating byproducts prevent the efficient electron tunneling through narrow energy barrier and lower the current density. Therefore, optimal doping concentration of 2 to 4 vol. % or around 10 mol. % would provide sufficient extrinsic charged carriers and minimize the formation of insulating compounds.

We also checked the effect of the thin Al layer on the efficiency of the charge generation. Figure 3-4 shows the current density as a function of voltage with and without a thin Al layer. Without 1 nm think Al layer, the current densities were drastically decreased by around two orders of magnitude and the onset voltage of charge generation was increased by 2 V. This thin Al interlayer between n-doped BPhen electron transporting layer and HAT-CN electron accepting layer facilitates the current flow through the depletion region in n-doped BPhen. However, the role of the Al interlayer is not clearly unveiled, and further studies should be done.

3.3.2 Single and Double Stacked Organic Light-Emitting Diodes

Based on the study of charge generation, we designed the double stacked OLEDs. First, we made double stacked OLEDs with same charge generation units for the charge generation study. TAPC was used as a hole transporting layer in the stacked OLEDs. Figure 3-6 shows the current density and luminance as a function of voltage for

the single and double stacked OLEDs. When we have well-operating charge generation units in the devices, the turn-on voltage should be doubled in the double stacked OLEDs (around 6 V). However, the double stacked OLEDs with TAPC hole transporting layers exhibits higher turn-on voltage than 6 V with both HAT-CN and MoO_3 electron accepting layer. TAPC is known to as a hole transporting materials with poor operating stability due to its high trap densities. TAPC is one of the representative materials with several different types of relatively weak bonds, and the dissociated π-radicals are likely to have singly occupied molecular orbital (SOMO) levels, resulting in the formation of deep level [50]. Figure 3-3 shows the schematic energy band structure in the interconnecting unit. Electron-hole pairs can be generated with applied forward bias in stacked OLEDs due to the small difference between HOMO levels of hole transporting materials and LUMO levels of electron accepting materials. In the presence of the deep traps of the TAPC layer, however, electrons are easily trapped in the deep level, resulting in higher barrier for charge generation and limited charge generation at the interface.

To validate the rationale for the relationship between the energy barrier of charge generation and the presence of traps in hole transporting materials, we fabricated hole only devices and compared the J-V characteristics. The onset of the charge generation is dependent on the energy barrier height, and thus the higher onset voltage of current injection through the device means the higher energy barrier for the charge generation. As shown in Figure 3-7, higher onset voltages of current injection were observed for the device the TAPC hole transporting layer with both MoOx and HAT-CN electron accepting layer. With HAT-CN electron accepting layer, the onset voltage difference

was bigger as nearly 1 V than that with MoOx. It is believed that the presence of deep traps affect more on the charge generation with more efficient electron accepting material of HAT-CN.

Based on the previous study of charge generation with various hole transporting materials and electron accepting materials, we used NPB as a hole transporting material with less traps and HAT-CN as an efficient electron accepting material as a in the double stacked OLEDs. Figure 3-9A and B show the current density and luminance as a function of voltage for the single and double stacked OLEDs with a NPB hole transporting layer. The double stacked OLED was turned on at around twice of the turn-on voltage of the single stacked OLED, indicating that the operation of the charge generation unit works effectively. However, this double stacked OLED with NPB hole transporting layers shows the steep roll-off on the current efficiency with increasing the current density or applied voltage, shown in Figure 3-9C. It is attributed to the increased luminance quenching due to the lower triplet energy of NPB than that of TAPC. Also, the electron leakage through NPB hole transporting layer due to insufficient barrier between the LUMO energies of the CBP and NPB.

In order to achieve efficient charge generation in the charge generation units and minimize the luminance and charge carrier loss near the emitting layers, TAPC with high triplet energy and shallow LUMO level was used as a main hole transporting material and 10 nm thick NPB layer was inserted next to the HAT-CN electron accepting layer, as shown in Figure 3-8. Figure 3-10A and B show the current density and luminance as a function of voltage for the single and double stacked OLEDs with a NPB hole transporting layer. The operation of the charge generation unit in the double

stacked OLED is still effectively. This double stacked OLED with TAPC and NPB hole transporting layers exhibits little roll-off in the current efficiency, indicating that the luminance quenching and electron leakage were drastically suppressed.

3.4. Summary

In summary, we studied the charge generation mechanism in stacked OLEDs. For the first part, we found that overall current generated from the charge generation units is significantly dependent on the electron flow through steep energy barrier of n-doped ETL, which is affected by doping concentration, if efficient electron accepting materials are used. For the second part, we fabricated green phosphorescent stacked OLEDs, and found that efficient electron accepting materials and trap-free hole transporting materials like NPB are needed to obtain effective charge generation.

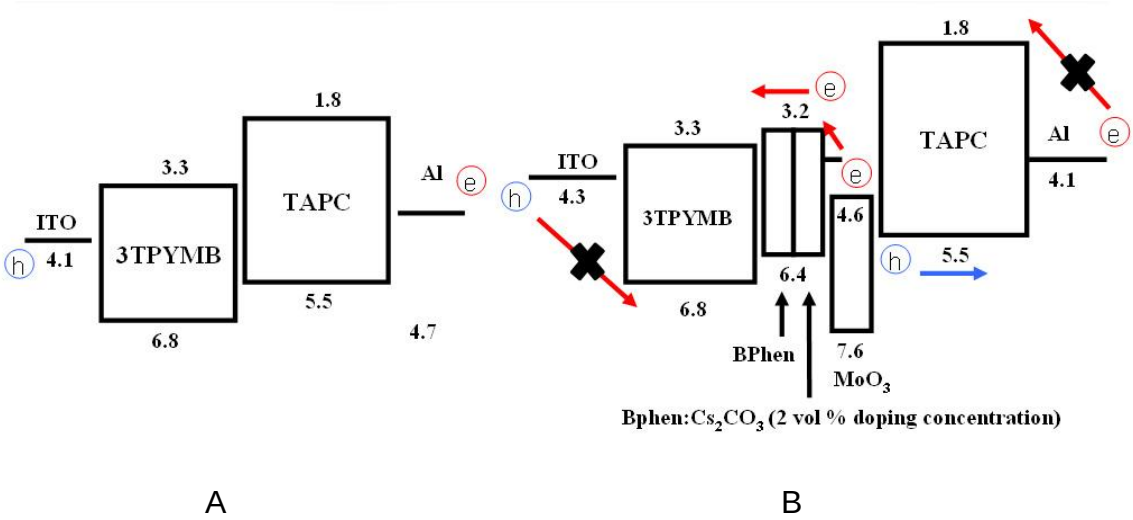

Figure 3-1. Schematic energy diagram of charge generation devices with different presence of the interconnecting unit: A) without and B) with an interconnecting unit under forward bias.

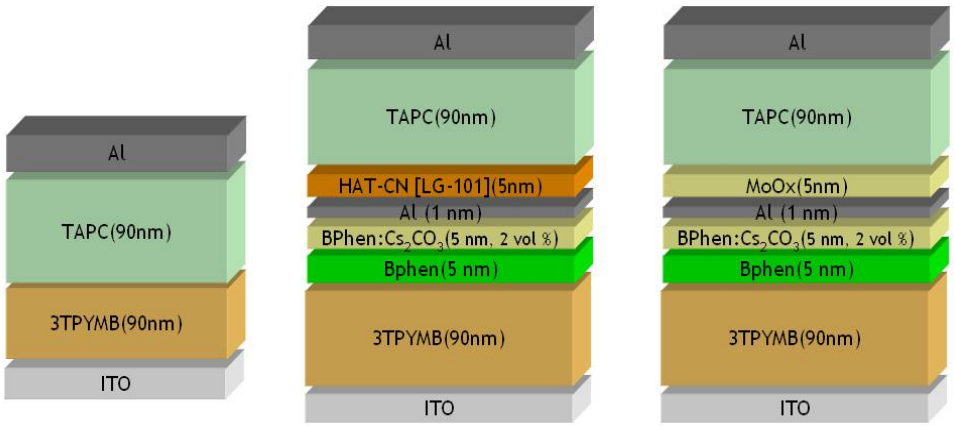

A

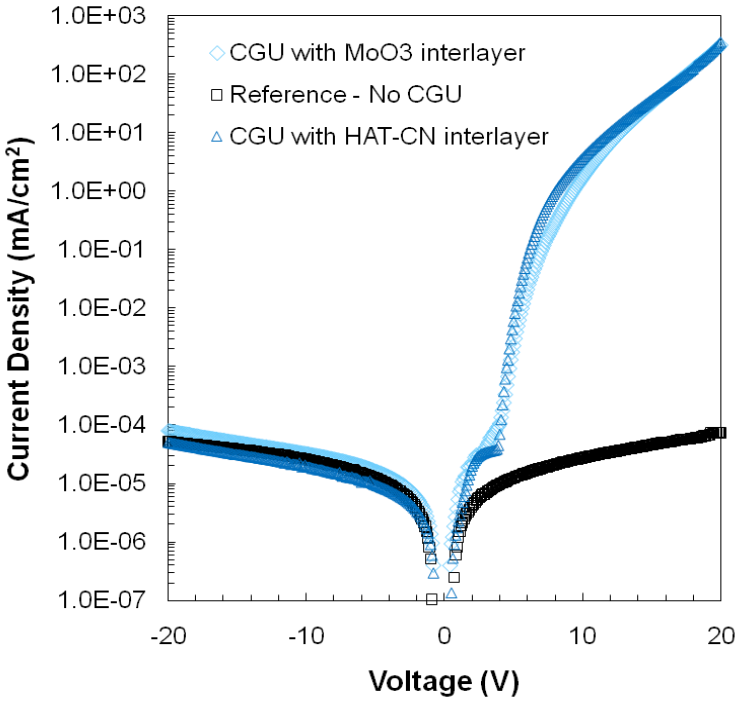

B

Figure 3-2. Device structure and I-V characteristics of devices with different presence of interconnecting units: A) schematic diagram of device structures for the comparison of charge generation of MoO_3 and HAT-CN n-type layer between TAPC hole transporting layer and B) current density plots of charge generation devices with MoO_3, HAT-CN and without the interconnecting units as a function of voltage.

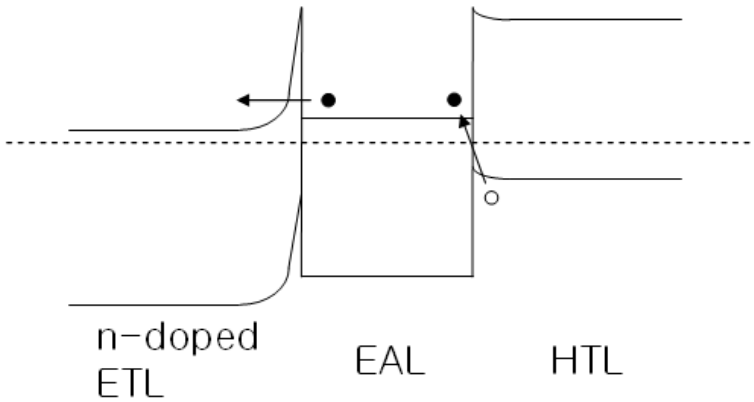

Figure 3-3. Proposed schematic energy band diagram of the charge generation interconnecting unit.

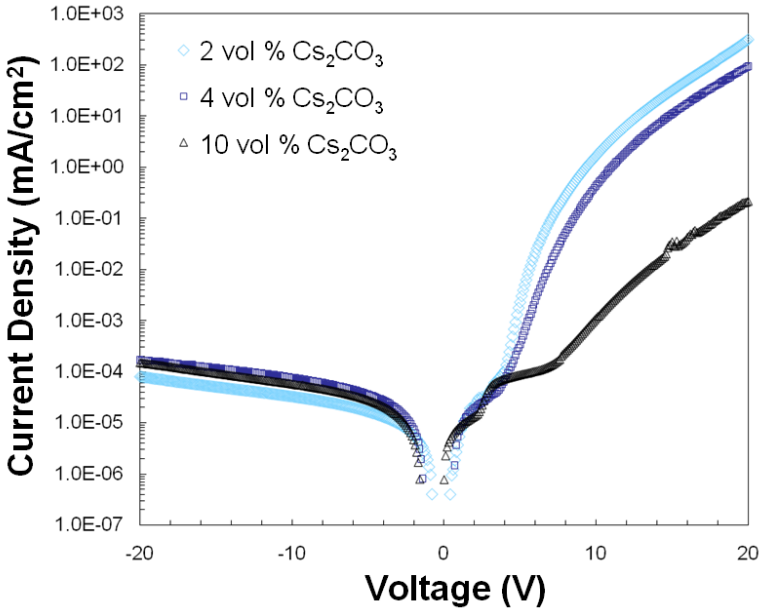

Figure 3-4. Current densities of charge generation devices as a function of voltage with various Cs_2CO_3 doping concentration in a BPhen electron transporting layer.

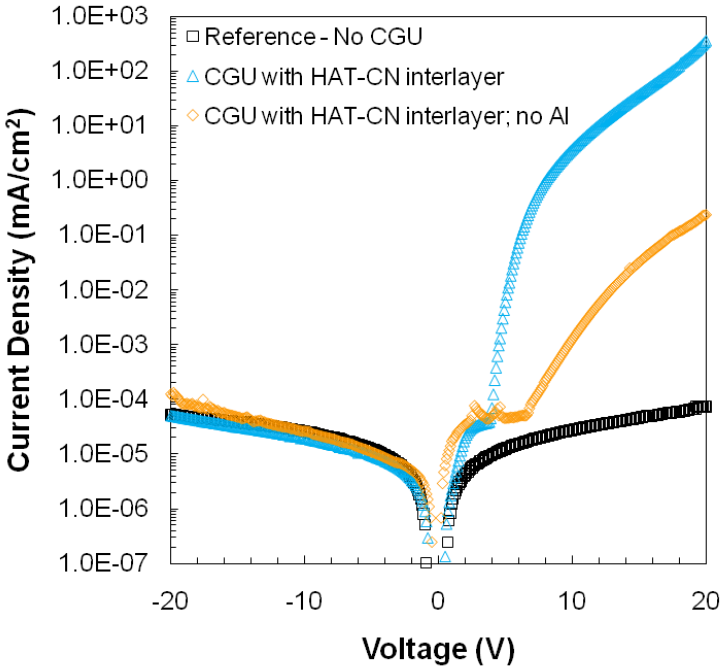

Figure 3-5. Current densities of charge generation devices as a function of voltage with and without a thin Al interlayer.

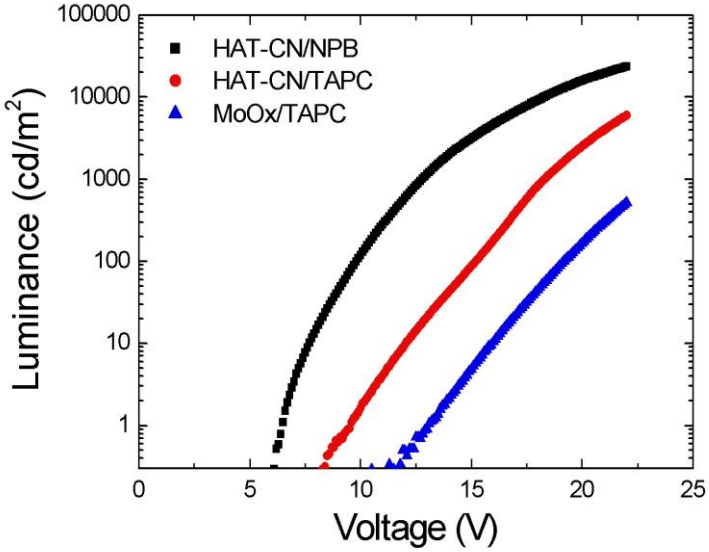

Figure 3-6. Luminance plots as a function of voltage of double stacked green phosphorescent OLEDs with different charge generation interfaces.

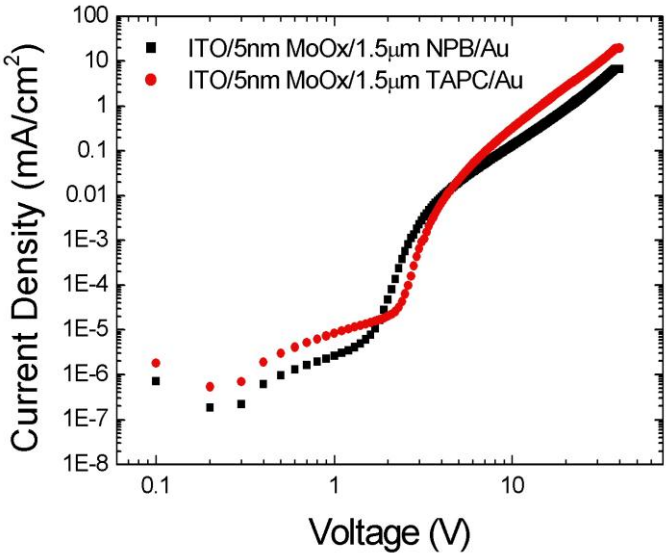

A

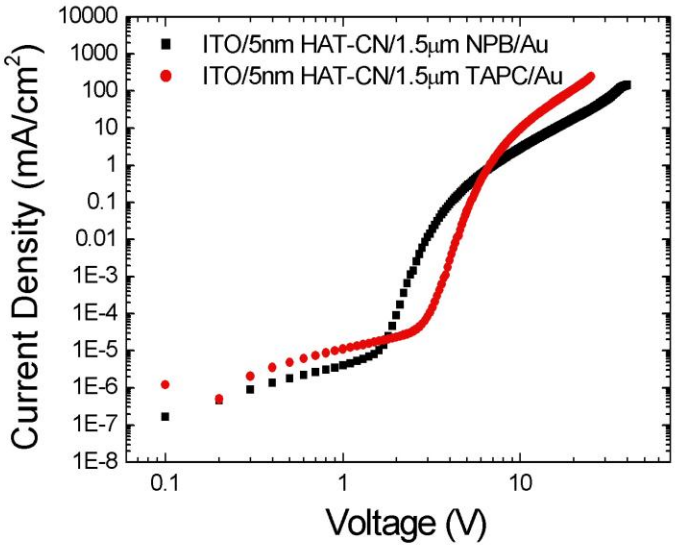

B

Figure 3-7. Current density plots as a function of voltage of NPB and TAPC hole only devices: A) with a 5 nm thick MoOx layer and B) with a 5 nm thick HAT-CN layer.

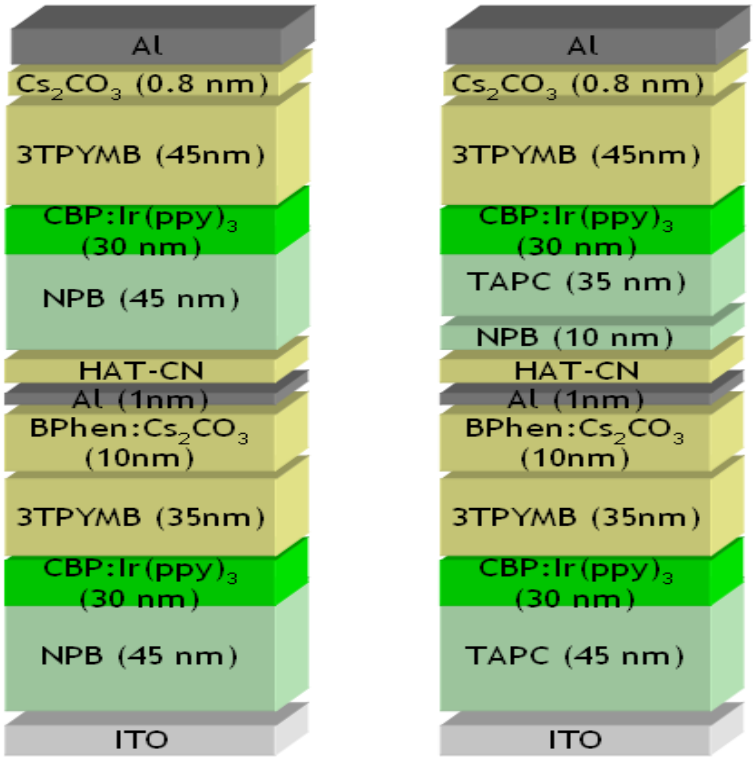

Figure 3-8. Schematic device structures of double stacked phosphorescent OLEDs.

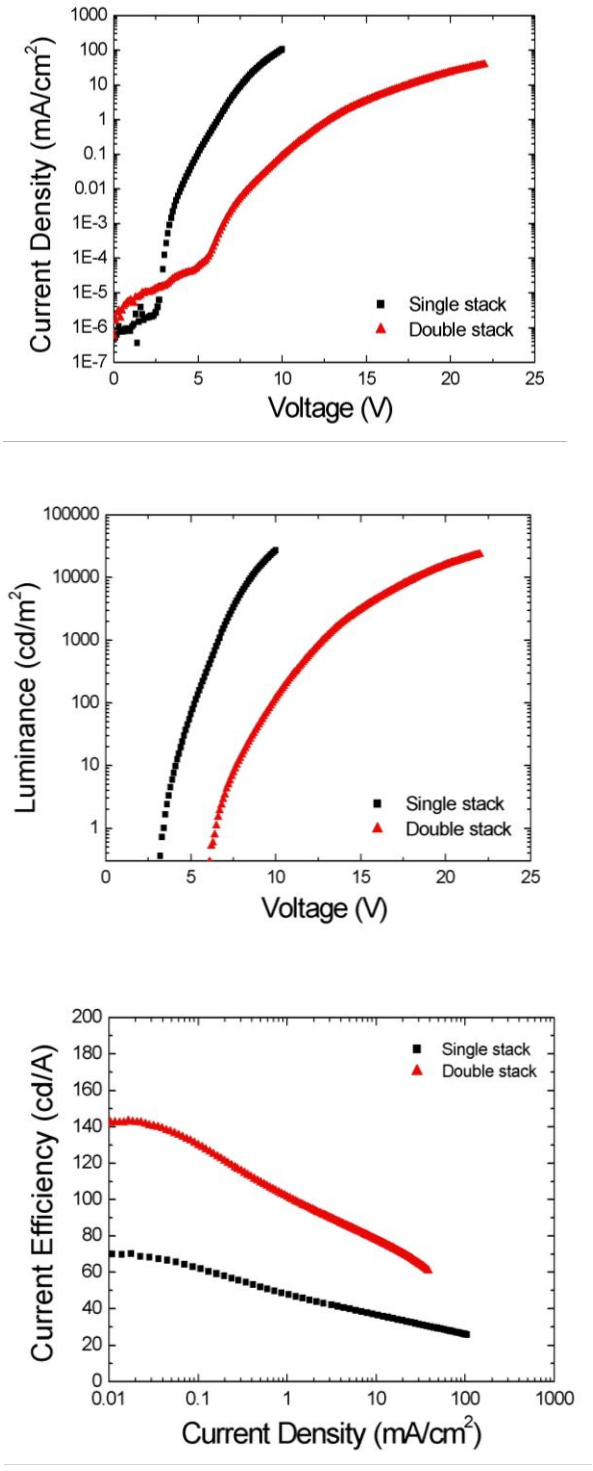

Figure 3-9. L-I-V characteristics and efficiencies of single and double stacked green phosphorescent OLEDs: A) Current density plots, B) luminance plots as a function of voltage and C) current efficiency plots as a function of current density of single and double stacked OLEDs with HAT-CN/NPB charge generation interface.

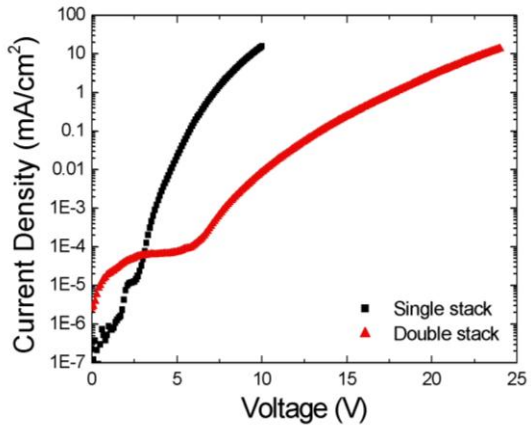

A

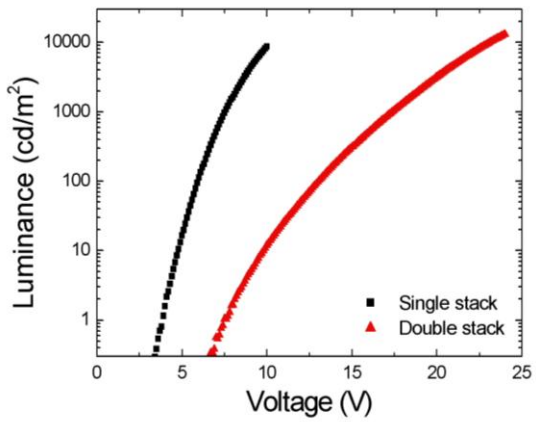

B

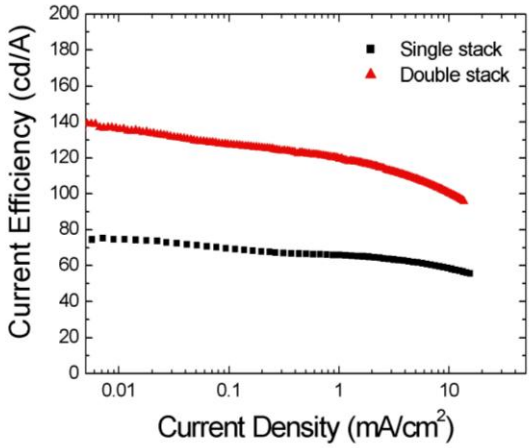

C

Figure 3-10. L-I-V characteristics and efficiencies of single and double stacked green phosphorescent OLEDs with the modified device structure: A) Current density plots, B) luminance plots as a function of voltage and C) current efficiency plots as a function of current density of single and double stacked OLEDs with HAT-CN/NPB charge generation interface and TAPC hole transporting layer.

CHAPTER 4
POLYMER-COLLOIDAL QUANTUM DOT HYBRID NEAR INFRARED LIGHT-EMITTING DEVICES

4.1 Background and Motivation

Colloidal quantum dots are an attractive choice for lumophores due to wide tunability in their band gap, high luminance efficiency, and narrow spectral emission. While early work in quantum dot hybrid LEDs are primarily focused on the emission at visible wavelengths, a few works have been done to achieve efficient IR emitting hybrid LEDs in spite of various applications such as night vision, chemical analysis and biomedical sensing.

In this work, we demonstrate solution processed hybrid LEDs incorporating PbSe colloidal quantum dots with enhanced efficiencies. Among II-VI semiconductors, a PbSe QD are a good candidate for the IR emitting lumophore since its optical properties can be easily modulated in the NIR region. Due to large Bohr radius of around 46 nm, quantum confinement effect is observed from relatively large PbSe nanoparticles. First, we fabricated hybrid multilayer LEDs based on QD films sandwiched between hole and electron transporting layers. We also fabricated hybrid LEDs based on the blend of QDs and MEH-PPV polymer [51].

4.2 Experimental Details

4.2.1 Synthesis and Processing of PbSe Colloidal Quantum Dots

Based on existing literature methods with appropriate variations [52], PbSe collidal quantum dots were synthesized. In a typical reaction, 4 mmol of PbO and 11 mmol of oleic acid were added to 35 ml of 1-octadecene. The mixture was stirred under heat and argon flow for 45 minutes. At the temperature of 155 ^{o}C, 12 mmol of 1 M trioctylphosphine (TOP)-Se and 0.11 ml of diphenyl phosphine (DPP) were rapidly

injected. The reacted quantum dots were withdrawn to two aliquots (after 30 and 60 seconds) and quenched with cold toluene. Subsequently the quantum dots were precipitated and extracted by adding acetone and ethanol by centrifugation. In order to achieve narrow quantum dot size distribution and eliminate excess organic residues and reaction byproducts, a three-step post synthesis washing of quantum dots was carried out [51]. Finally, the quantum dots were dried under argon and dissolved in chlorobenzene for device fabrication or in tetrachloroethylene (TCE) for optical characterization.

4.2.2. Device Fabrication

To fabricate the hybrid light-emitting devices, a 40 nm thick PEDOT:PSS layer was spin-coated as a hole injection layer on pre-cleaned ITO coated substrates and baked in air at 180 ^{o}C for 20 minutes. Monodispersed PbSe quantum dots and MEH-PPV were dissolved in chlorobenzene with various concentrations. This solution was then spin-coated as the active layer on the PEDOT:PSS coated substrates and annealed under nitrogen at 60 ^{o}C for 15 minutes. Subsequently, an 8 nm think BCP layer as the electron transporting and hole blocking layer and a LiF/Al cathode layer were deposited by thermal evaporation.

4.2.3. Characterization of PbSe Colloidal Quantum Dots and Hybrid Light-Emitting Devices

The absorption spectra of colloidal quantum dots in tetrachloroethylene were measured using a Varian Cary 500 UV-vis-near-IR spectrophotometer. A SPEX 270M spectrometer was used for photoluminescence measurements. Transmission electron micrograph images were acquired using a JEOL JEM-200CX microscope at an acceleration voltage of 200 kV.

The current-voltage-photocurrent measurements of the hybrid light-emitting devices were performed using a Keithley 2400 sourcemeter in conjunction with a Thorlabs InGaAs calibrated photodiode. A longpass filter with short wavelength cutoff at 830 nm was used to block any visible emission from the polymer. An Ocean Optics NIR256-2.1 near-IR spectrometer was used to measure electroluminescence spectra. External quantum efficiency in the infrared was determined by measuring the emission intensity in the forward direction and converting it to total external emission.

4.3 Results and Discussion

4.3.1 PbSe Colloidal Quantum Dots

Figure 4-2A shows typical near-IR absorption and photoluminescence spectra of ~ 4 nm diameter PbSe quantum dots and the TEM micrograph image (inset). The uniformly distributed 2-dimensional hcp lattice in the TEM image and the narrow full width at half maximum (FWHM) of the PL spectrum (~130 nm) confirm narrow size distribution of the PbSe quantum dots obtained without any post-synthetic size selective processing. Based on size-tunable absorption spectra with a wide range of infrared wavelengths of 1000 to 1900 nm, shown in Figure 4-2B, the application of these PbSe quantum dots for the solution-processed IR emitters is expected.

4.3.2 Hybrid Multilayer QD LEDs

For the first approach, we made hybrid multilayer QD LEDs, consisting a QD layer sandwiched by a hole transporting layer and an electron transporting layer. In order to fabricate multilayer devices with solution processing, the damage from the solvent to the underneath layer should be avoided. We took the stability test on several small molecule hole transporting materials such as NPB, TAPC and copper phthalocyanine (CuPc) by spin casting the organic solvents such as chloroform and chlorobenzene on

top of the layer. The NPB and TAPC film were totally washed out after the spin casting, but the CuPc film was visually remained due to the limited solubility of CuPc. Hence, we fabricated the QD LEDs on the CuPc hole transporting layer.

Figure 4-3 shows the current density and photocurrent density plots as a function of voltage. To block the hole leakage current into the tris(8-hydroxy-quinolinato)aluminium (Alq_3) electron transporting layer, hole blocking layers such as 3-(4-biphenyl)-4-phenyl-5-tert-butylphenyl-1,2,4-triazole (TAZ) and BCP were inserted between the QD layer and the Alq_3 layer. Without any hole blocking layer, the infrared light output was very low with a peak photocurrent density of $4*10^{-5}$ mA/cm^2 at around 13 V. On the contrary, with hole blocking layers, photocurrent densities were enhanced without significant change in current densities, leading to the increase in external quantum efficiencies of the devices by one order of magnitude. However, these EQE levels are quite low compared to previous reports on the visible hybrid LEDs. These low EQEs indicate that charged carriers from the carrier transport layers to the PbSe quantum dots are not effectively injected. As the energy barrier between the CuPc HOMO level and PbSe QD CBM level is small, electrons are likely to flow to the CuPc hole transporting layer, resulting in high electron leakage current. Moreover, we checked the surface morphology of the CuPc film after spin casting with chloroform. As shown in Figure 4-4, networks of pileup lines were observed. It seems that the subsequent spin casting of QD solution dissolves CuPc molecules on the surface and changes the surface morphology. This rough surface generates the pathway for current leakage and it leads to reduce the EQE.

Therefore, we tried different approaches to form the hybrid multilayer QD LEDs. Coe-Sullivan et al. demonstrated a method to form a QD monolayer on a small molecule hole transporting layer by phase segregation during spin coating of the solution of QD and TPD mixture [53]. Based on their processing technique, the aliphatic moiety of oleic acid ligands and the aromatic moiety of TPD hole transporting materials have a tendency to separate each other. As a result, when the mixture of QD and TPD is spun-coated, the PbSe QDs are segregated and floated from TPD, and the QD monolayers can be generated on the TPD layer.

Figure 4-5A and B show the device performance of these multilayer hybrid LEDs. The photocurrent density was increased by two orders of magnitude, and the EQE was enhanced to 0.026 %. Despite the big improvement of the efficiency, the EQE is much lower than that of reported visible hybrid LEDs. We checked the surface morphology of the QD layer on TPD, and we found that the QD coverage of the surface is quite low in spite of high concentration of the mixture. It indicates that most of QDs are still embedded in the TPD layer, and small portion of QDs is segregated. The limited coverage of QD layer on the TPD surface is the main reason for the low EQE.

4.3.3 Hybrid Polymer-QD LEDs

While hybrid LEDs with semiconductor quantum dots dispersed in a conjugated polymer have been reported, the efficiencies were usually low due to the unfavorable energy alignment of the wide bandgap quantum dots and the conjugated polymers and inefficient energy or charge transfer from the polymers to the quantum dots. On the other hand, the valence band maximum (VBM) and conduction band minimum (CBM) of narrow bandgap quantum dots such as PbSe are in proximity of the HOMO and LUMO energy of many conjugated polymers, and more efficient energy/charge transfer from

the polymer to the PbSe quantum dots is expected. Figure 4-3 shows the device architecture and the energy levels of the PbSe QD based LEDs. The HOMO energy of MEH-PPV matches the VBM of the quantum dots. The CBM of the quantum dots is positioned within the bandgap of MEH-PPV and efficient electron transfer from the polymer to the PbSe quantum dots is expected. It should be noted that these colloidal PbSe quantum dots are capped with a layer of oleate ligands to prevent aggregation and to passive their surfaces, and the excess amount of the capping ligands can impede efficient charge transfer due to their insulating characteristic [54]. Therefore, to obtain efficient EL from the QDs, a rigorous three-step post-synthesis washing was carried out to remove excess organics and reaction byproducts.

Figure 4-4A shows the current density-voltage-photocurrent characteristics of a hybrid LED with a polymer/QD blend containing 1 wt. % QDs. The device turns on at around 3 V, which is significantly lower than the previous PbSe QD based LEDs in the multilayer device structure [17]. The peak external quantum efficiency of the device is around 0.1 %. Figure 4-4B shows the EL spectrum of the device, showing the narrow IR emission at 1280 nm.

4.3.3.1 Effect of QD concentration

Figure 4-5A shows the current density-voltage characteristics of the hybrid LEDs with different compositions. The current density decreases with increasing the concentration of QDs in the layer at all operating voltages. To compare the device performances, data from a device with a neat MEH-PPV emitting layer of the same thickness as the hybrid LEDs are also plotted in the same figure. Figure 4-5 B shows the photocurrent-voltage characteristics of the hybrid LEDs. IR emission intensity increases as the concentration of QDs is increased from 1 wt. % to 3 wt. %, but it is

reduced with further increase in QD content. The turn-on voltage of the devices increases as the concentration of QDs in the layer is increased. While the device with a neat MEH-PPV emitting layer exhibits orange emission with the EQE of around 1 %, the EQE from MEH-PPV emission decreases by 90 % to about 0.1 % for the device containing 9 wt. % QDs. The NIR EQEs of the hybrid LEDs with varying the concentration of PbSe QDs are shown in Figure 4-5C. At low current densities, the EQE increases from the device containing 1 wt. % QDs to the device containing 3 wt. % QDs, but decreases for the devices with higher concentration of QDs. However, at current densities higher than 10 mA/cm^2, the device with 6 wt. % QDs shows the highest NIR EQE with the peak value of 0.65 %. Interestingly, the EQEs of the hybrid LEDs remain reasonably flat over a wide range of current densities without any significant roll-off, indicating the devices are in good charge balance.

The EQE of the hybrid LEDs strongly depends on the efficiency of excitation transfer to the emitting QDs. It has been suggested that possible routes of excitation to QDs in hybrid LEDs are neutral-excitation energy transfer (Förster energy transfer) due to dipole-dipole interactions and direct injection of carriers [15, 55]. Both mechanisms strongly depend on the distance separating the polymer and the QDs. As shown in Figure 4-5A, the increase in the concentration of QDs in the devices leads to the significant reduction in the device current, especially at low operating voltages. The decrease in current indicates that the PbSe QDs in the polymer act as charge trapping centers. The CBM of the PbSe QDs is well positioned within the bandgap of MEH-PPV and it favors strong electron trapping in the QDs. At the same time, due to small difference in the HOMO energy of MEH-PPV and the VBM of PbSe QDs and hole

transporting properties of MEH-PPV, the presence of QDs should not affect strongly in hole transport. Consequently the additions of QDs would further increase the hole dominance. The BCP layer acts as a hole blocking layer and its presence enhances the recombination of blocked holes with trapped electrons in the QDs, resulting in the increase in EQEs. Charge trapping due to lumophores leads to the enhancement in EL efficiency, whereas charge trapping due to defects leads to the decrease in EL efficiency. This charge trapping enhancing in EL has been observed in dye-dispersed polymer LEDs, where the driving voltage also increases with the dye-doping concentrations [56, 57]. The increase in the turn-on voltage with higher QD concentrations is also consistent with the presence of QD charge traps. Therefore, direct carrier injection into the QDs due to the charge trapping plays an important role in determining the recombination efficiency in the hybrid LEDs. Increased charge trapping with higher QD content is also evidenced by the significant suppression of MEH-PPV emission with increasing QD concentration in the emitting layer. In spite of the presence of long chain organic ligands, the conformation of single chain ligands on a high curvature QD surface leaves significant portions of the surface accessible for electronic contact by the surrounding polymer matrix [58]. It has been reported that the relatively long chain ligands do not impede the excitation transfer to a great extent [32, 59]. The aggregation of QDs should not be an issue because the shift in photoluminescence and electroluminescence spectra is insignificant.

4.3.3.2 Effect of active layer thickness

To investigate further the correlation in charge trapping mechanism and EL emission, the effect of the active layer thickness on the performance of the hybrid LEDs was studied. Figure 4-6 shows the peak EQEs of the devices containing 6 wt. % PbSe

QDs as a function of the emitting layer thickness. The EQE increases with increasing the device thicknesses and peaks at the value of 0.83 % in a hybrid LED with a 210 nm thick active layer. The device with an active layer thicker than 210 nm shows a drastic reduction in current density and EL efficiency. It should be noted that the peak efficiency shifts to higher current density as the device thickness increases, indicating that charge balance is improved at higher current density with a thicker active layer. As the charge carriers travel through longer distances across the devices with increased thickness, the probability of the carriers of being trapped by the PbSe QDs increases, resulting in the reduction in device current and increase in EL efficiency. Taking into account strong ITO absorption (~60 %) in the NIR wavelength, the maximum EQE of the hybrid LEDs can reach ~1.2 % if the ITO electrode is replaced by an electrode with no infrared absorption. Assuming that the device has a light extraction efficiency of ~20 % similar to OLEDs, the internal quantum efficiency can be ~6 %, which is significantly higher than previous reported results.

4.4 Summary

In summary, we fabricated multilayer PbSe QD hybrid infrared LEDs. Due to the damage on organic layer during spin casting or limited QD coverage fabricated by phase segregation, the maximum external quantum efficiency was very limited up to 0.026 % for the device by phase segregation.

We also demonstrated hybrid infrared LEDs based on PbSe colloidal quantum dots and MEH-PPV polymer. Through the study and optimization of the devices, we obtained the maximum external quantum efficiency of 0.83 % at the peak wavelength of 1280 nm. This work exhibited a significant enhancement in device efficiencies

compared to previously reported QD based IR LEDs. However, further improvement is expected with the optimization of materials and device architecture.

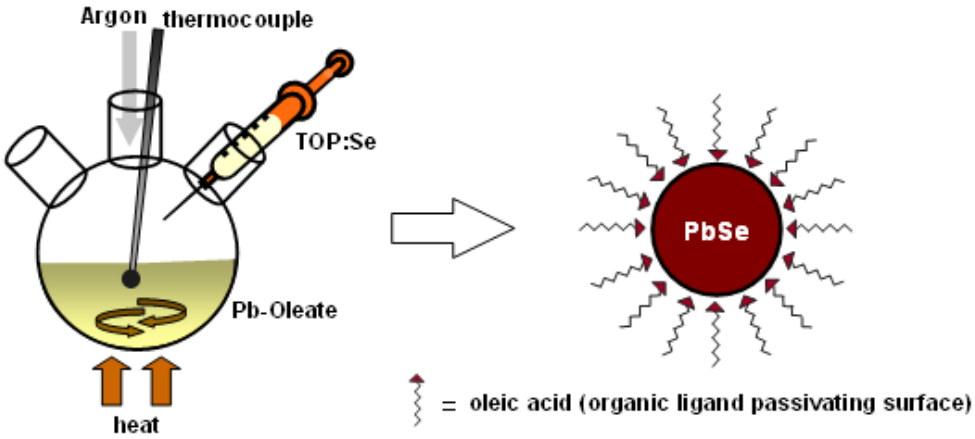

Figure 4-1. Schmatic drawing of the PbSe quantum dot synthesis and PbSe quantum dots capped with oleic acid ligands

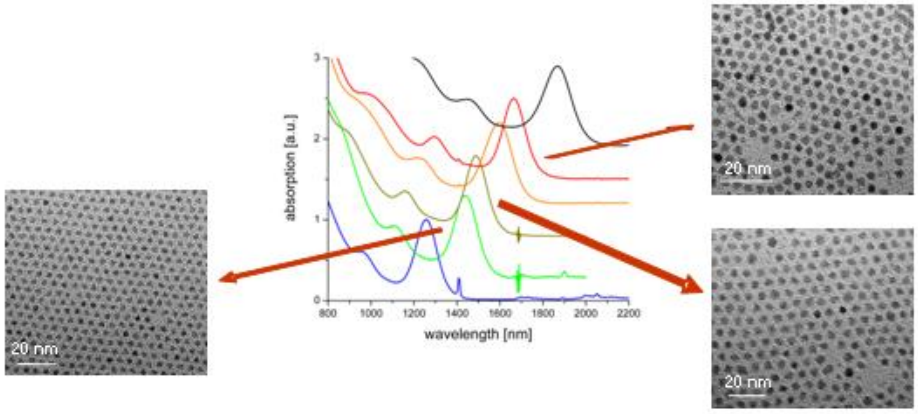

A

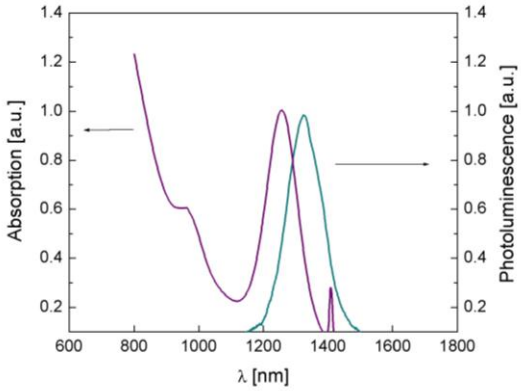

B

Figure 4-2. Optical properties of colloidal PbSe QDs: A) Size-tunable absorption spectra of PbSe QDs and their corresponding TEM images and B) typical absorption and photoluminescence spectra of PbSe QDs

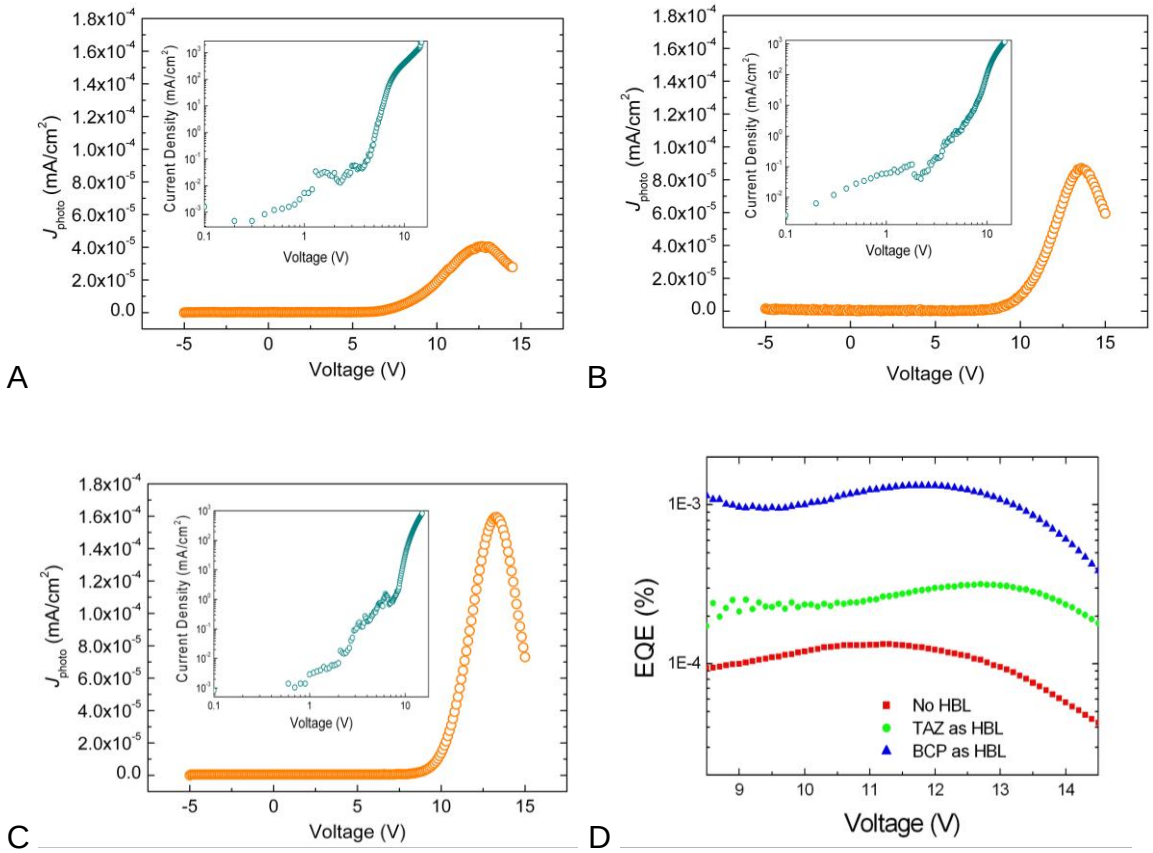

Figure 4-3. Photocurrent densities, current densities (insets) and efficiencies of multilayer hybrid LEDs: photocurrent density plots and current density plots with A) no additional hole blocking layer, B) TAZ hole blocking layer and C) BCP hole blocking layer, and D) EQE plots as a function of voltages for these three devices.

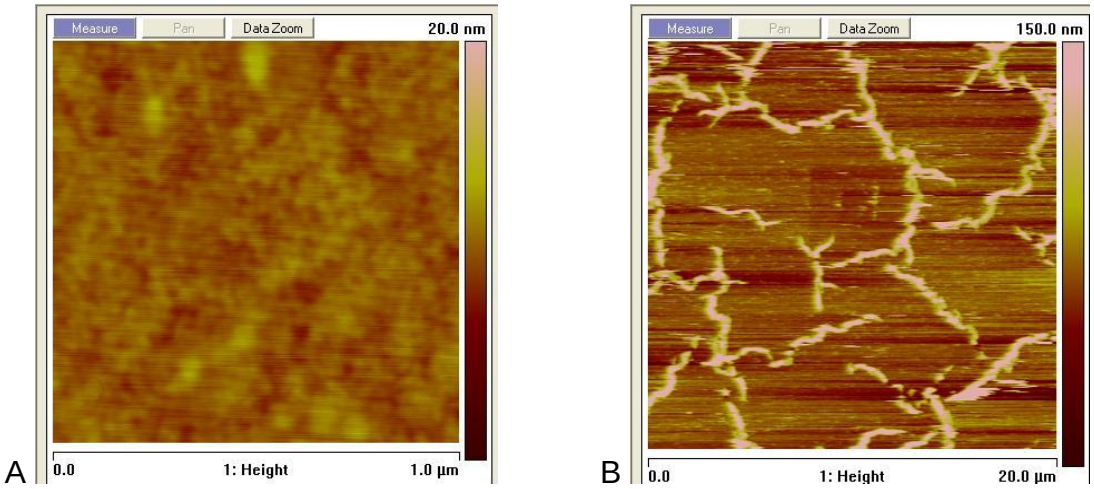

Figure 4-4. AFM images of different surface treatment on CuPc layer: A) pristine CuPc layer and B) CuPc layer after chloroform spin coating.

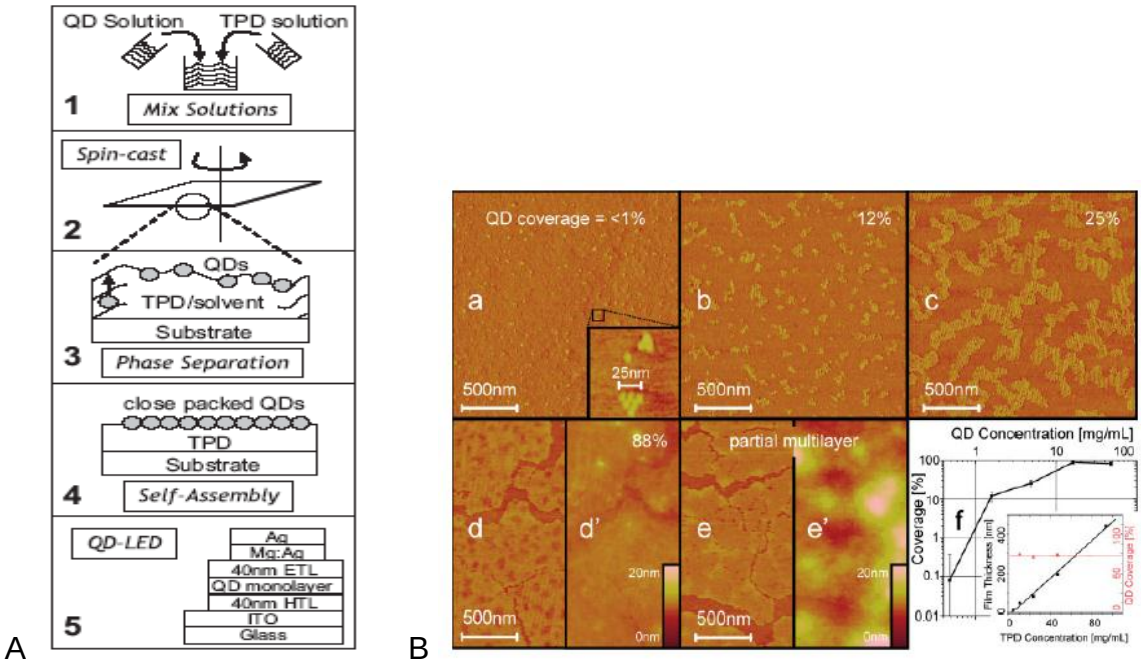

Figure 4-5. Schematic illustration of phase segregation technique and AFM images of QDs on an organic layer: A) schematic description of the fabrication of organic/QD bilayer through phase segregation during spin casting and B) AFM images of QDs on TPD surface with different QD concentrations. (0.48 – 48 mg/mL) (Adapted from [53])

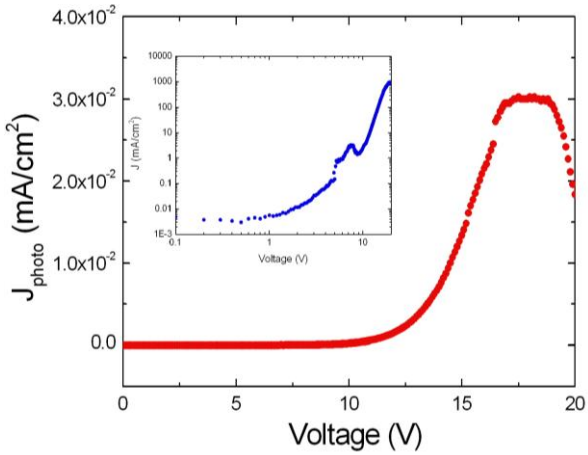

A

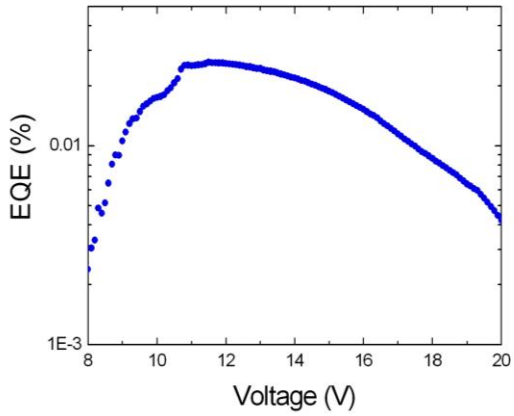

B

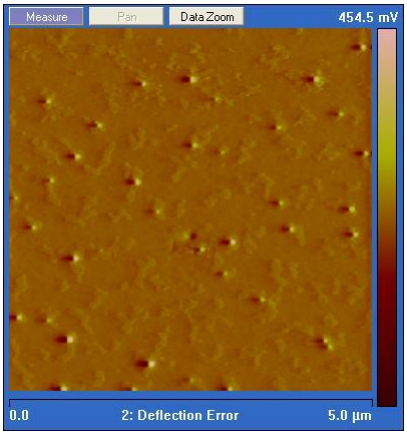

C

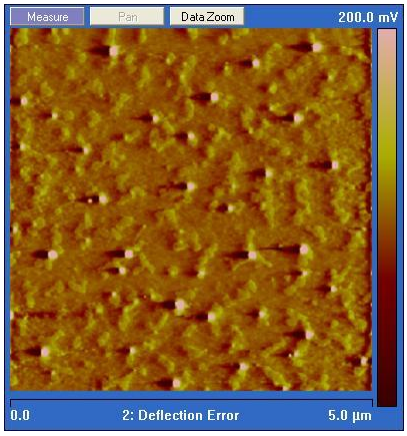

D

Figure 4-6. L-I-V chracteristics and efficiencies of multilayer hybrid LEDs by phase segregation method and AFM images of QDs on an organic layer: A) photocurrent density plots and current density plots (insets) and B) EQE plots as a function of voltage of multilayer hybrid LEDs fabricated by phase segreration technique and AFM images of the PbSe QD layer on TPD from C) 47 wt. % PbSe QDs in the mixture and D) 64 wt. % PbSe QDs in the mixture.

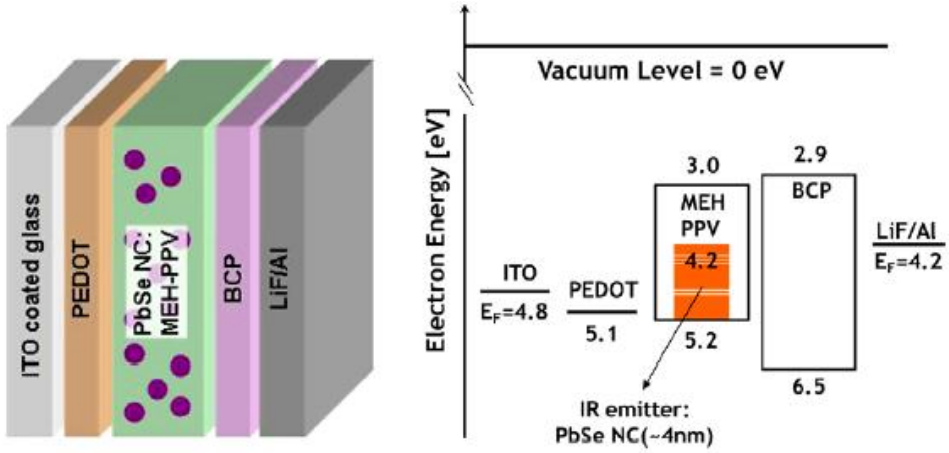

Figure 4-7. Schematic diagram of polymer-QD device structure and energy levels.

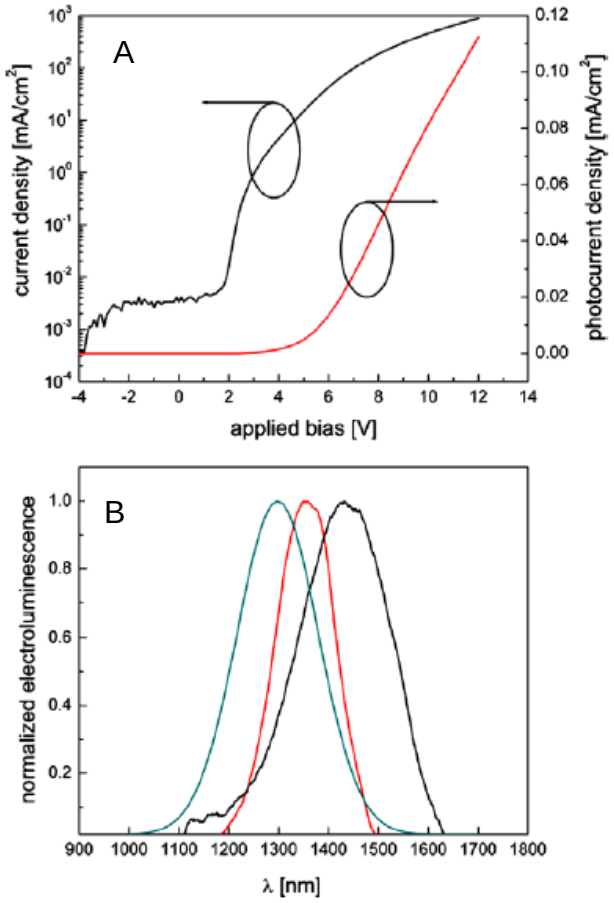

Figure 4-8. L-I-V characteristics and electroluminescence spectra: A) current-voltage-photocurrent characteristics of a device containing 1wt. % PbSe QDs and B) normalized infrared electroluminescence spectra of hybrid LEDs.

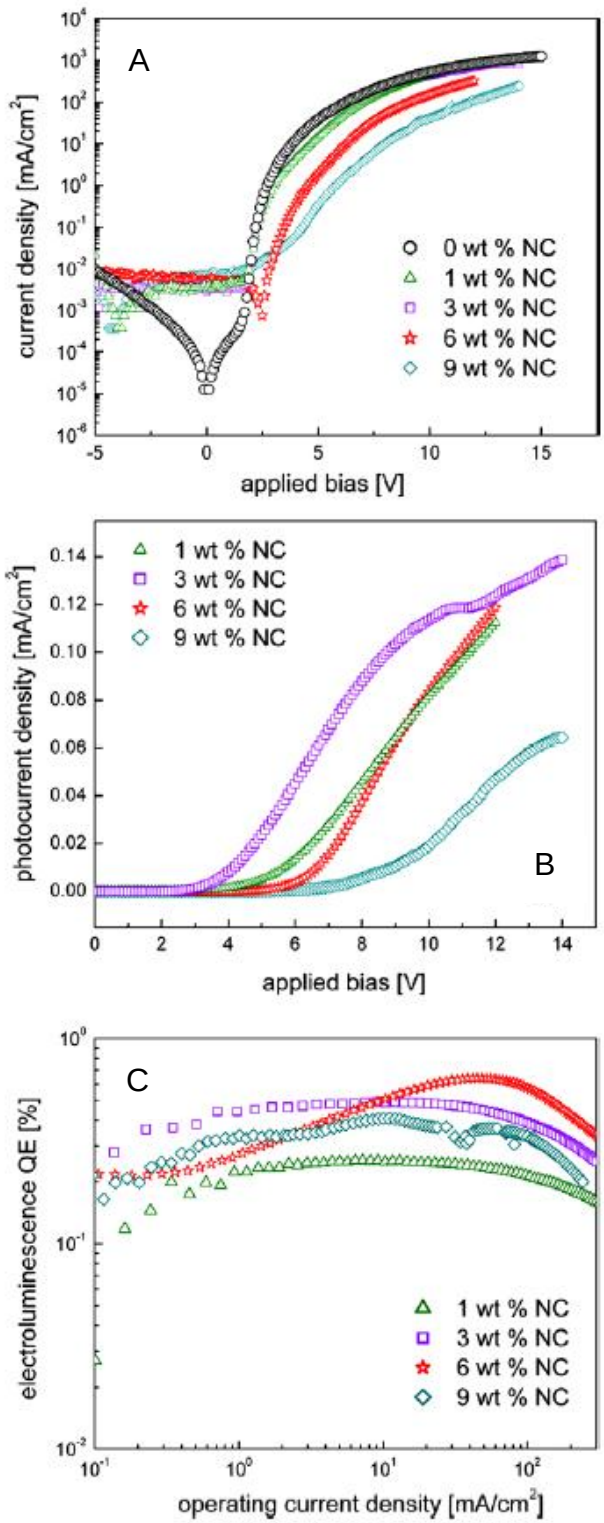

Figure 4-9. L-I-V characteristics and efficiencies of hybrid LEDs: A) current, B) photocurrent of hybrid LEDs as a function of voltage and C) external quantum efficiencies as a function of operating current density.

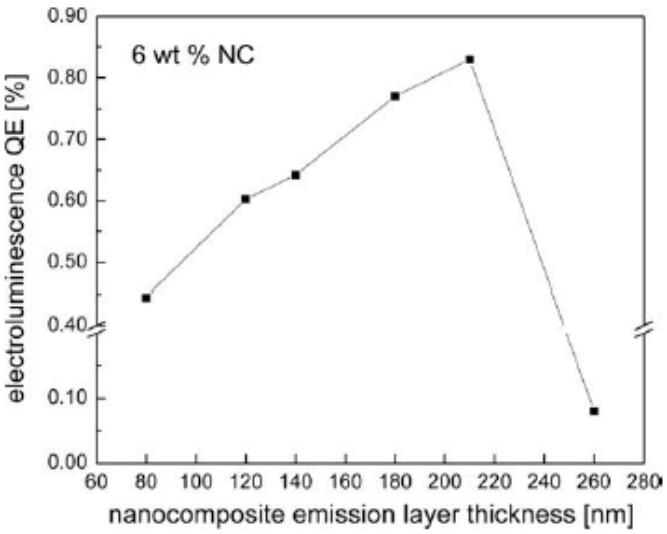

Figure 4-10. External quantum efficiency plot of hybrid LEDs containing 6wt. % PbSe QDs as a function of active layer thickness.

CHAPTER 5
NEAR INFRARED-TO-GREEN ORGANIC UP-CONVERSION DEVICES

5.1 Background and Motivation

With increasing interest in night vision and security, near-infrared (NIR) to visible up-conversion devices have attracted a great deal of research interest. Early NIR up-conversion devices were mostly based on heterojunction structures of inorganic semiconductors such as AlGaAs, InP, and GaAs[60-63]. Ban et. al. fabricated an up-conversion device consisting of an organic light-emitting diode (OLED) with a InGaAs/InP photodetector [64]. However, the photodetector portion of the device was grown by MOCVD, an epitaxial growth method that is not compatible with the large area processing of OLEDs. Contrast to the up-conversion devices based on inorganic semiconductors, all organic up-conversion devices can be fabricated on any suitable substrates, and thus some research have been performed recently. Yase et al. reported the NIR-to-blue up-conversion behavior in fluorescent OLEDs with TiOPc photosensitive hole injection layer [65, 66]. However, all of these previous up-conversion devices showed low external quantum efficiency of less than 0.05 %.

In our previous study, we demonstrated an efficient organic NIR-to-green up-conversion device integrating tin (II) phthalocyanine (SnPc):C_{60} bulk heterostructure layer as a NIR sensitizing layer and fac-tris(2-phenylpyridinato) iridium (III) ($Ir(ppy)_3$) based phosphorescent OLEDs [67]. However, due to the proximity between the work function of indium-tin oxide (ITO) and the highest occupied molecular orbital (HOMO) level of IR absorbing SnPc, hole injection from ITO starts even at low voltages, resulting in decrease of the sensitivity of the up-conversion performance.

In this work, we report the enhancement in the up-conversion performance by controlling hole injecting properties. Also, it is well known that good charge balance in OLEDs is crucial to obtain high external quantum efficiency or current efficiency, and thus the photon-to-photon conversion efficiency of the up-conversion devices is related to the charge balance in the light-emitting structure. We demonstrate the effect of electron injection on the current efficiency of the up-conversion devices in this paper.

5.2 Experimental Details

The NIR-to-green up-conversion devices were fabricated on patterned ITO substrates with a sheet resistance of 20 Ω per square. The ITO substrates were cleaned with acetone and isopropanol in an ultrasonic cleaner and subsequently rinsed with de-ionized water, blown dry with N_2 gas, and treated with UV-ozone. SnPc and C_{60} was purified three times by a train sublimation technique [68]. All layers in the up-conversion devices except a ZnO nanoparticle layer were thermally evaporated at a pressure of $1*10^{-6}$ torr. For a solution processed hole blocking layer, we used ZnO nanocrystals ranging from 3-5 nm in size, which were synthesized by a sol-gel process using precursors of zinc acetate and tetramethylammonium hydroxide (TMAH) [69]. BCP or UGH2 were also used as a small molecule hole blocking layer, and SnPc:C_{60} mixed layer was used as an infrared sensitizing layer. TAPC, CBP:$Ir(ppy)_3$ and 3TPYMB layers were used as a hole transporting layer, an emission layer, and an electron transporting layer, respectively. LiF/Al was used as a reference cathode, and Cs_2CO_3/Al or Al layer was used to study the effect of the electron injection. The area of the device is 0.04 cm^2.

Luminance-current-voltage (L-I-V) characteristics of the up-conversion devices were measured using a Keithley 2400 source meter for current voltage measurements coupled with a Keithley 6485 picoammeter connected to a calibrated Si photodiode for photocurrent measurements. A Newport LPM830-30C CW diode laser with a power density of 500 mW/cm^2 was used as the IR light source. For the measurement of optical power dependence of IR irradiation, a series of Newport FBR-ND neutral density filters were used. The data was acquired using LabView interface. The measurements were carried out at room temperature under an ambient atmosphere.

5.3 Results and Discussion

5.3.1 Control Up-Conversion Device

First, we made a control up-conversion device without any hole blocking layer, as shown in Figure 5-1A. Figure 5-1B shows the luminance-current-voltage (L-I-V) characteristics of the device with and without IR illumination. To represent the on/off characteristics of the up-conversion device, we define two parameters: the maximum operating photon-to-photon conversion efficiency and the operating regime. The maximum operating photon-to-photon conversion efficiency, defined as the ratio of the number of emitted green photons to the number of incident IR photons at the dark-current induced turn-on voltage ($V_{on/dark}$), shows the actual maximum photon-to-photon conversion efficiency with IR irradiation which can be realized from the up-conversion device at the condition without emission at dark. The operating regime is defined as the voltage range between $V_{on/dark}$ and the photocurrent induced turn-on voltage ($V_{on/photo}$), thus it is actual voltage range that we can utilize the device as an on/off switching device. This control device was turned on even at low operating voltage of 6 V at dark, resulting in low maximum operating photon-to-photon conversion efficiency of 0.06 %. It

is because the hole injection from ITO anode into light emitting structure is not well-blocked and green light comes out at low operating voltage, as indicated in Figure 5-2A. In order to reduce the hole injection from the anode and enhance the sensitivity of the up-conversion device, we designed to modify the hole injection properties between the anode and the SnPc:C_{60} IR-sensitizing layer.

5.3.2 Effect of Hole Blocking Layer

As a first step to reduce the hole injection from the ITO anode, we fabricated the up-conversion devices with different thickness of SnPc:C_{60}. Thicker IR sensitizing layer is expected to have more absorption of infrared light and less electrically injected hole transport in the layer due to the poor hole transport properties of SnPc:C_{60} mixed layer [67, 70]. As shown in Figure 5-3A, with thicker IR sensitizing layer, $V_{on/dark}$ increased, leading to better on/off characteristics. In order to assess the on/off characteristics, we compare the maximum operating photon-to-photon conversion efficiency, shown in Table 1. As the thickness of the IR sensitizing layer increased, the maximum operating photon-to-photon conversion efficiency increased. The increase in the maximum operating photon-to-photon conversion efficiency is mainly attributed to the extended operating regime resulting from suppressed hole transport from the anode because there is little difference in the photocurrent induced luminance between these devices.

To achieve the efficient hole blocking for the anode, we inserted a hole blocking layer between the ITO anode and the IR sensitizing layer in the up-conversion devices. We used bathocuproine (BCP) and p-bis(triphenylsilyl)benzene (UGH2) as hole blocking materials since these materials have been reported hole blocking properties with deep HOMO level of 6.1 and 7.2 eV, respectively [71, 72]. We also tried a ZnO nanoparticle layer with a deep valence band maximum (VBM) of 7.6 eV as a solution-

processed hole blocking layer [73]. For the comparison, we made an up-conversion device inserting a 1,4,5,8-naphthalenetetracarboxylic dianhydride (NTCDA) interlayer with deep LUMO level between the ITO anode and the IR sensitizing layer [74]. As shown in Figure 5-3B, this device did not exhibit the hole blocking behavior with NTCDA, but hole injection seemed to be improved instead. It is due to the charge generation between the NTCDA and SnPc, because the energy barrier between the LUMO level of NTCDA and the homo level of SnPc is small. The devices with BCP and UGH2 showed clear hole blocking properties, shown in Figure 5-3C. At dark, the device with 10 nm thick of UGH2 was turned on at 8.4 V. The device with 10 nm thick of BCP showed better hole blocking characteristics with $V_{on/dark}$ of 14.5 V. It is believed that the film formation of BCP can be denser than UGH2 due to the lower glass transition temperature (T_g) and smaller molecule size, even though same thickness of the blocking layer was deposited. BCP has low T_g of below 80 ^oC, which is lower than reported T_g of organosilane phosphorescent hosts (100-130^oC) like UGH2 [75, 76]. It should be noted that both hole blocking layers were deposited at very low deposition rate of 0.3 A/sec, and this condition would facilitate the crystallization of the molecules.

The operation of the up-conversion devices with a hole blocking layer was illustrated in Figure 5-2B and C. When a hole blocking layer is applied in the up-conversion devices, the hole carriers are blocked efficiently from the anode due to the deep HOMO of the hole blocking layer, and the emission of green light can be suppressed until higher applied voltages. Upon illumination of IR light, high luminance of the green light is emitted from the recombination of photogenerated holes and electrically injected electrons from the cathode. As the photocurrent induced luminance

of the devices was not reduced significantly compared to that of the control device, we obtained the higher maximum operating photon-to-photon conversion efficiency because of the extended operating regime.

We examined the effect of the thickness of the hole blocking layer on the up-conversion performance. Figure 5-3D shows the L-I-V characteristics of the devices with various thickness of the BCP hole blocking layer. Increase in the thickness of the BCP layer shifted the $V_{on/dark}$ further, resulting in expansion of the operating regime. However, the device with 10 nm thick BCP showed the highest maximum operating photon-to-photon conversion efficiency of 1.38 %. Excessively thick BCP layer reduced the luminance with IR irradiation drastically. Since the absorption of green light in BCP is negligible, the reduction in the photocurrent induced luminance is believed to result from the decrease of the voltage drop in the light-emitting structure.

5.3.3 Effect of Electron Injection Layer

To study the effect of the charge balance on the up-conversion devices, we fabricated the up-conversion devices with different electron injection layers such as LiF, Cs_2CO_3, and without electron injection layer. In order to highlight the dependence of the device operation on the amount of electron injection, we did not insert any hole blocking layer in these sets of the devices. As shown in Figure 5-4A, the devices with a better electron injection layer showed higher luminance both at dark and with IR illumination. The higher dark-current induced luminance and smaller $V_{on/dark}$ in the device with better electron injection indicates that the onset of the dark-current induced luminance is affected by the amount of electron injection, as well as the amount of hole injection. However, we observed little difference in the maximum operating photon-to-photon conversion efficiency between the devices, compared with the difference between the

devices with various hole injection properties. It means that the sensitivity of the up-conversion devices are more affected by controlling hole injection properties. In order to realize highly efficient up-conversion devices, the charged carriers need to be balanced in the device, because the photon-to-photon conversion efficiency of the up-conversion devices is correlated with the photo-generating efficiency of the IR sensitizing layer and the external quantum efficiency of the light-emitting structure. Figure 5-4B shows the current efficiency of the up-conversion devices with various electron injection properties. The device with LiF showed the best current efficiency of 80 cd/A with low roll-off, which indicates that this device has the best charge balance even until high operating voltage among these sets of the devices and LiF is an appropriate choice for the electron injection layer in the up-conversion devices.

5.3.4 Dependence of Optical Power Density

We examined the device operation with changing IR optical power. We used 10 nm BCP hole blocking layer and 1 nm thick LiF electron injection layer in the device. When we measured the device with IR laser, the current density and luminance increased continuously with increasing voltage. However, we observed saturation from certain voltages in the current density and luminance measured with reduced optical power by neutral density filters, shown in Figure 5-5A and B. It means that the number of photo-generated holes injected from IR sensitizing layer, which is limited by the illuminated optical power of infrared light, is less than the number of electrons injected from the cathode at the saturation regime. By the measurement with IR illumination of 5 mW/cm^2 optical power density, the maximum operating photon-to-photon conversion efficiency was 2.54 %, whereas it was measured as 1.00 % with IR laser of 500 mW/cm^2 optical power density.

5.4 Summary

In summary, we have demonstrated NIR-to-green organic up-conversion devices with various hole blocking structures. Both to thicken IR sensitizing layer and to insert hole blocking layer enabled the enhanced on/off characteristics due to the suppression of hole injection from the anode. The maximum operating photon-to-photon conversion efficiency is 2.54 %.

Table 5-1. Materials used in this work for hole blocking layers with their respective HOMO and LUMO energies.

Materials	HOMO (eV)	LUMO (eV)	Reference
NTCDA	-8.0	-4.0	[74]
UGH2	-7.2	-2.8	[71]
BCP	-6.1	-2.4	[72]
ZnO (QD)	-7.6	-4.4	[73]

Table 5-2. Dark-current-induced turn-on voltage and maximum operating photon-to-photon conversion efficiency with various hole injection structures (measured with 500 mW/cm^2 optical power density).

Hole blocking and IR sensitizing layers	Dark-current-induced turn-on voltage (V)	Maximum operating photon-to-photon conversion efficiency (%)
20 nm SnPc:C_{60}	6.4	0.06
40 nm SnPc:C_{60}	7.2	0.36
60 nm SnPc:C_{60}	8.9	0.66
10 nm UGH2 / 20 nm SnPc:C_{60}	8.4	0.16
10 nm BCP / 20 nm SnPc:C_{60}	14.5	1.38
35 nm ZnO (QD) / 20 nm SnPc:C_{60}	14.9	1.39
20 nm BCP / 20 nm SnPc:C_{60}	18.4	0.44

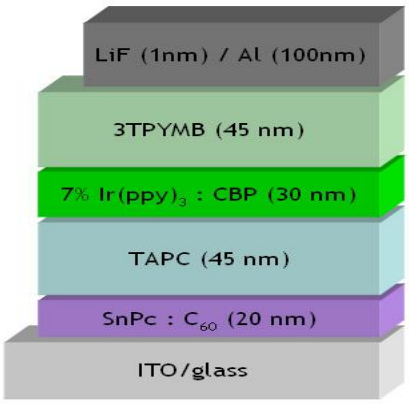

A

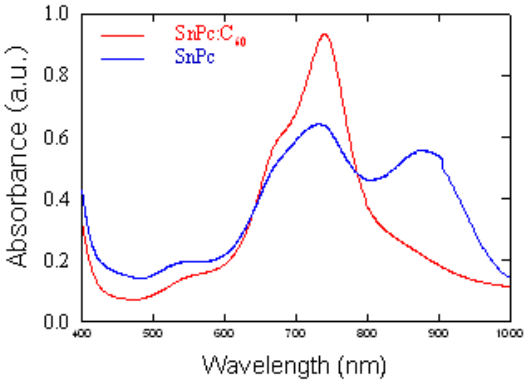

B

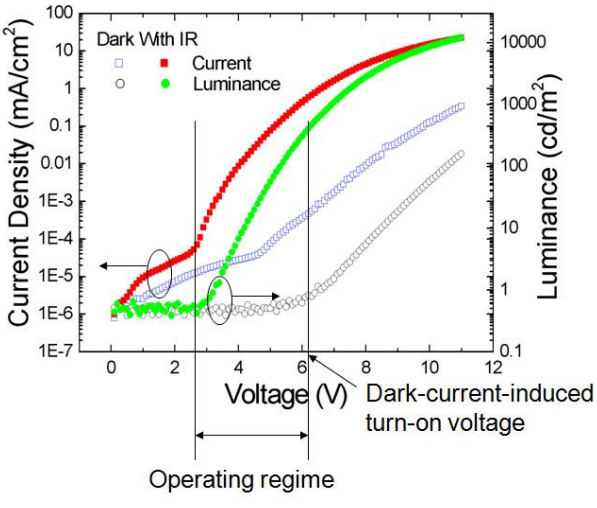

C

Figure 5-1. Schematic drawing and L-I-V characteristics of the up-conversion device and infrared absorption of SnPc and SnPc:C_{60} mixed layer: A) schematic drawing of the control up-conversion device structure, B) absorption spectra of SnPc and SnPc:C_{60} mixed layer and C) current density and luminance plots as a function of voltage of the control up-conversion device.

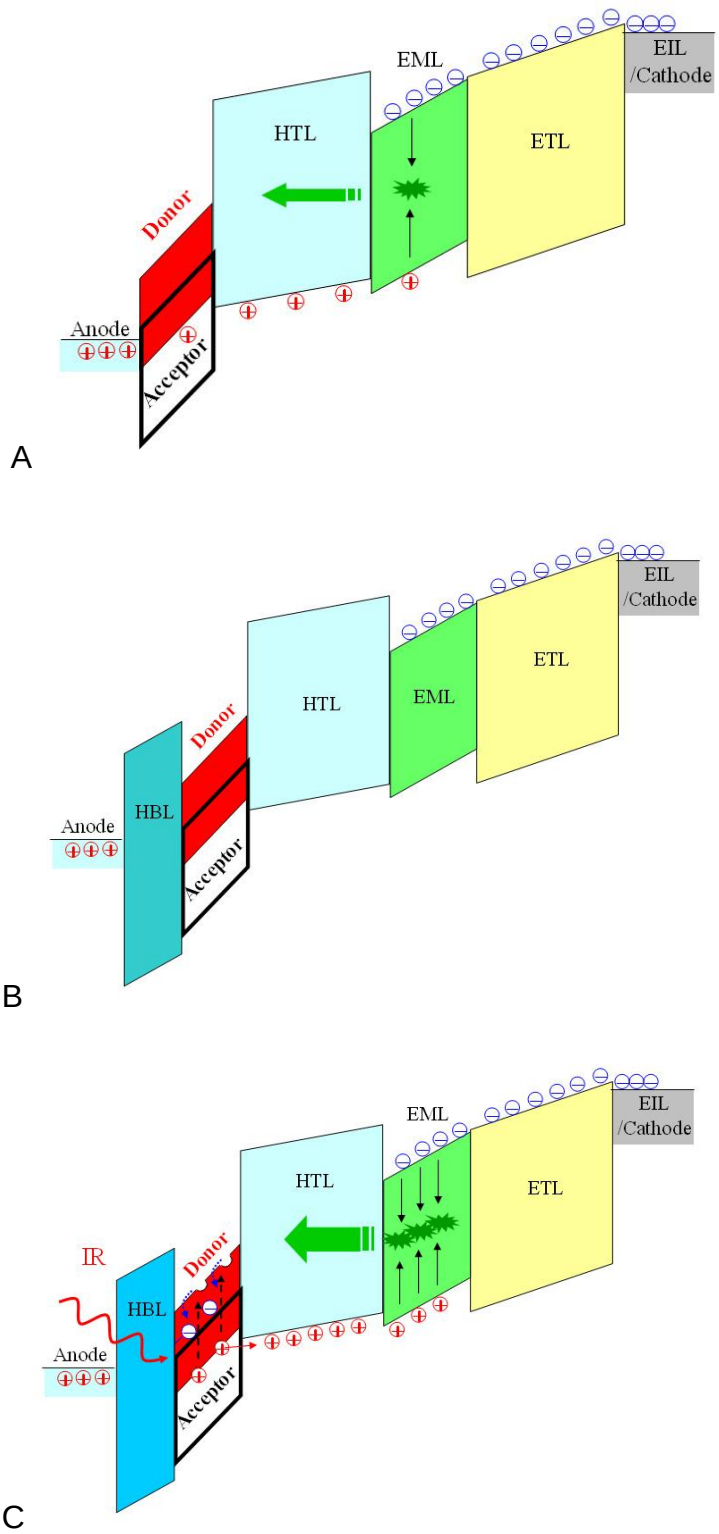

Figure 5-2. Schematic energy band diagrams of the up-conversion device under applied voltage: A) without any hole blocking layer at dark, B) with a hole blocking layer at dark and C) with IR irradiation.

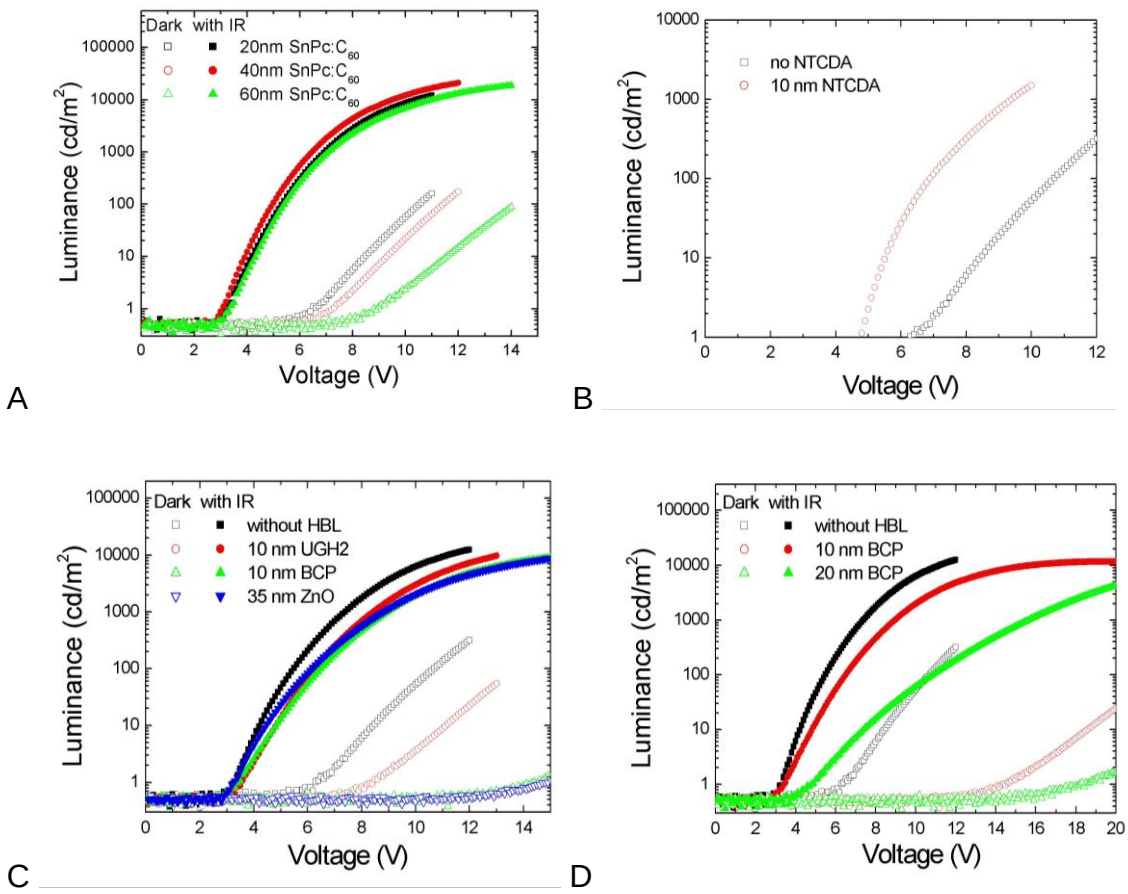

Figure 5-3. Luminance plots of up-conversion devices with various hole injection properties: A) luminance plots as a function of voltage with different thicknesses of SnPc:C_{60} layer, B) luminance plots as a function of voltage with and without NTCDA, C) luminance plots as a function of voltage with various hole blocking layers (UGH2, BCP and ZnO) and D) luminance plots as a function of voltage with different thicknesses of BCP hole blocking layer.

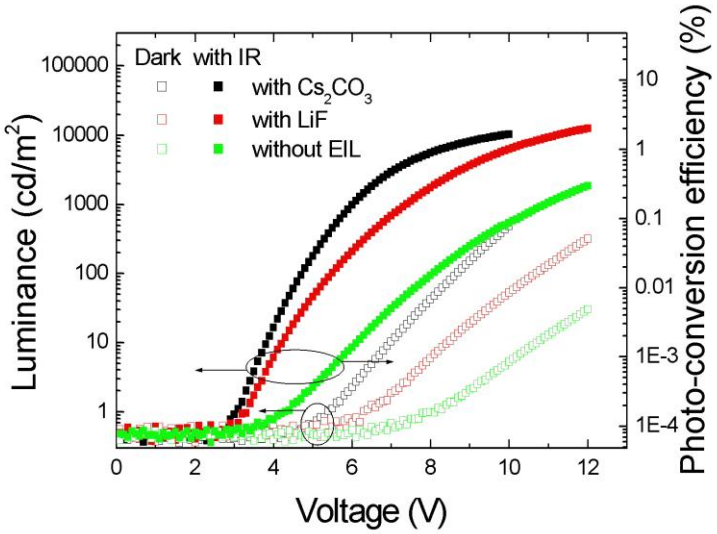

A

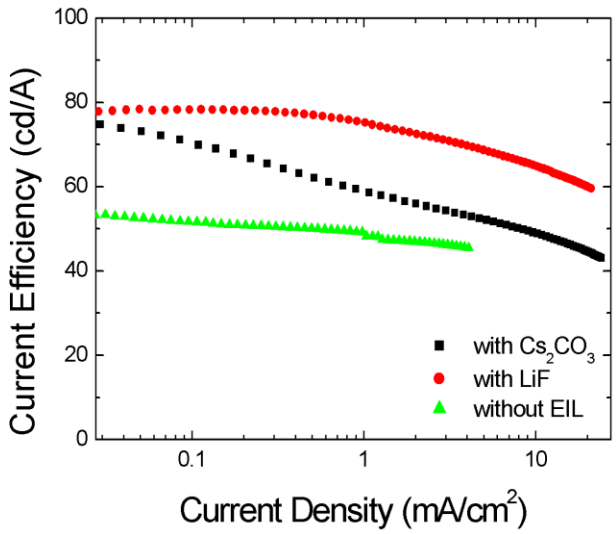

B

Figure 5-4. Luminance plots and efficiencies of up-conversion devices with various electron injection layers: A) luminance plots as a function of voltage and B) current efficiency plots as a function of current density.

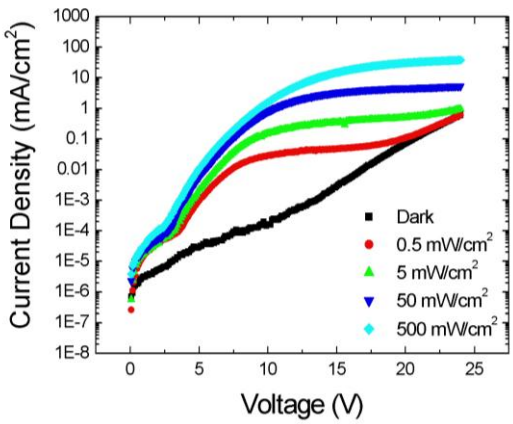

A

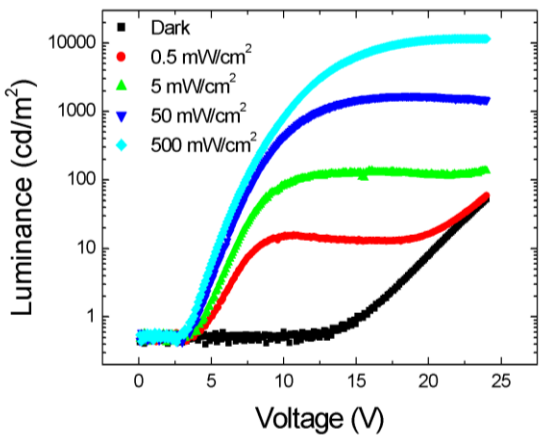

B

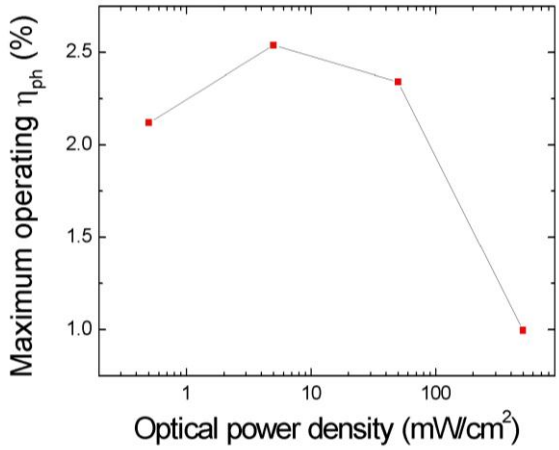

C

Figure 5-5. L-I-V characteristics and maximum operating photon-to-photon conversion efficiencies measured with different incident optical power: A) current density plots, B) luminance plots as a function of voltage with different optical IR power density and C) maximum operating photon-to-photon conversion efficiency plot as a function of power density.

A

B

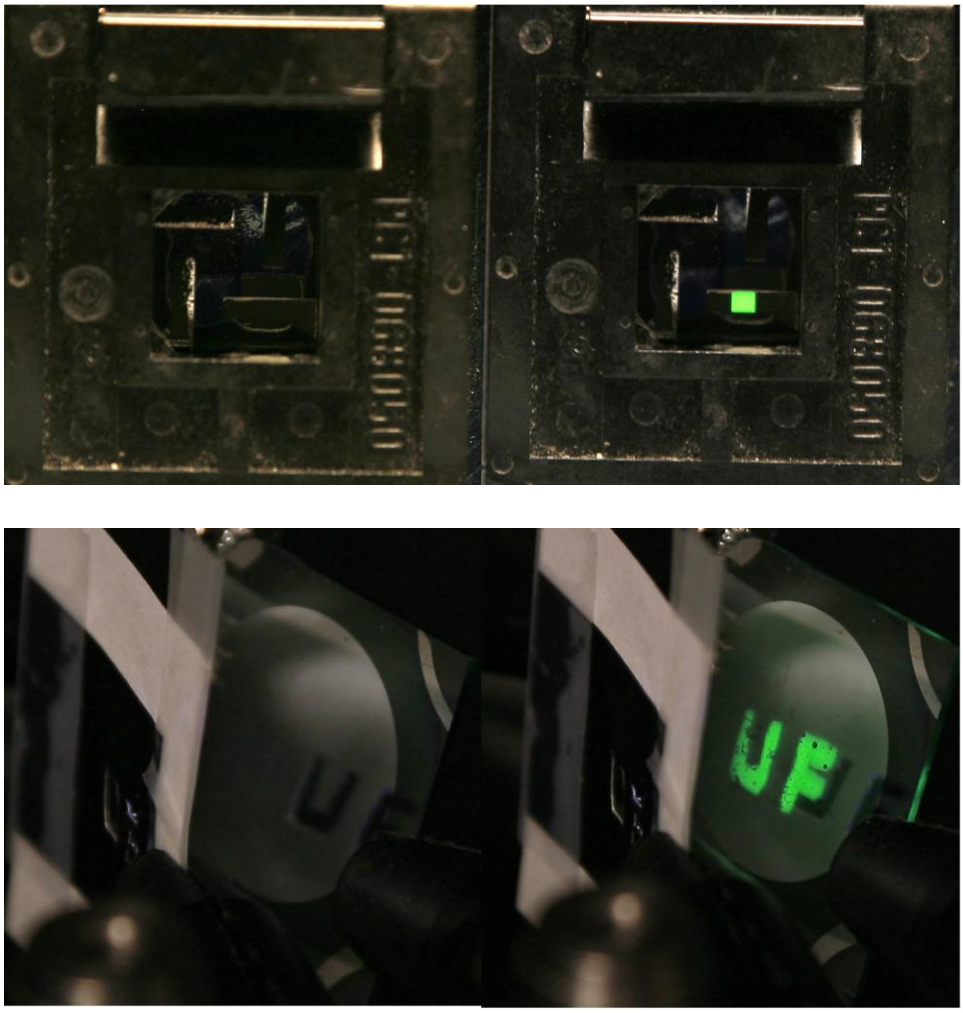

Figure 5-6. Images of device operation for up-conversion devices with different device sizes: A) images of device operation without (left) and with (right) IR laser irradiation for small area device (2X2 mm^2) and B) images of device operation without (left) and with (right) IR monochromatic irradiation through the patterned slit for large area device. (Circle with 0.75 inch diameter)

CHAPTER 6
QUANTUM DOT BASED NEAR INFRARED-TO-GREEN HYBRID UP-CONVERSION DEVICES

6.1. Background and Motivation

Up-conversion devices have attracted a great deal of interest due to their potential applications in night vision, security, range finding and semiconductor wafer inspection. Early near-infrared (NIR) up-conversion devices were made by integrating an infrared photodetector with a visible light emitting device based on inorganic compound semiconductors [60-63]. However, fabrication of infrared-to-visible up-conversion devices based on inorganic semiconductors is challenging due to the lattice mismatch between different types of semiconductor materials used for photodetectors and light emitting diodes. Because of the high costs of epitaxially-grown inorganic devices, these devices are only suitable for small area applications. Recently, optoelectronic devices based on organic materials have received a lot of attention due to their compatibility with large area manufacturing. Up-conversion devices using organic semiconductors have previously been demonstrated by Yase's group. These devices can be realized by integrating an organic light emitting diode (OLED) with an organic photodetector [65, 66]. However, the devices showed very low photon-to-photon conversion efficiencies, typically less than 0.05 %. These low conversion efficiencies were due to the low efficiencies of OLEDs and organic photodetectors. More recently, we have reported improved all-organic up-conversion devices by integrating a fac-tris(2-phenylpyridinato)iridium-(III) ($Ir(ppy)_3$) phosphorescent OLED and a tin phthalocyanine (SnPc):C_{60} bulk heterostructure NIR photodetector [67]. Compared to the earlier devices, these devices showed a significantly higher photon-to-photon conversion efficiency of

2.7 % due to the efficient light emission in phosphorescent OLEDs and efficient dissociation of photo-generated carriers in the NIR photodetecting layer.

While there was progress made in device performance, these all-organic up-conversion devices have no infrared sensitivity beyond 1 μm. Detecting photons at long wavelengths requires narrow bandgap inorganic semiconductors. Ban et al. reported a hybrid organic/inorganic up-conversion device by integrating an OLED with an InGaAs/InP photodetector with sensitivity up to 1.5 μm [64]. However, the photon-to-photon conversion efficiency of the device was only 0.25 %. In addition to low efficiencies, the hybrid up-conversion devices are expensive to fabricate because the device fabrication is only compatible with small size wafer processing.

In this work, we demonstrated a low-cost up-conversion device with infrared sensitivity up to 1.5 μm using inorganic colloidal PbSe quantum dots as a NIR sensitizer [77]. PbSe QDs were chosen because their optical absorption can be tuned from 0.7 to 2.0 μm [78-80].

6.2. Experimental Details

The structure of our NIR-to-visible light up-conversion device is schematically shown in Figure 6-4A. Up-conversion devices were fabricated on patterned ITO substrates with a sheet resistance of 20 Ω per square. The ITO substrates were first cleaned with acetone and isopropanol in an ultrasonic cleaner and subsequently rinsed with deionized water, blown dry with N_2 gas, and treated with UV ozone. Following this, a 60 nm layer of ZnO QDs was spin-coated on top of the ITO substrate and then annealed at 90 ^{o}C for 15 min in the ambient. The substrate was subsequently introduced into a nitrogen glovebox, and a 50 nm PbSe QD layer was spin-coated. The

PbSe QD layer was then treated with a benzenedithiol (BDT) solution to improve electronic coupling between individual QDs. This treatment renders the PbSe film insoluble. For the OLED part of the device, a 45 nm thick 1,1-bis[(di-4-tolylamino)phenyl]cyclohexane (TAPC) layer was used as a hole transporting layer (HTL), a 30 nm thick 4,4-N,N-dicarbazole-biphenyl (CBP) layer doped with $Irppy_3$ was used as an emitting layer, and tris[3-(3-pyridyl)-mesityl]borane (3TPYBM) (45 nm) was used as a hole blocker/electron transporting layer (ETL). LiF/Al (1 nm/100 nm) was used as the cathode. All layers in the up-conversion devices were vacuum deposited at a pressure of $1X10^{-6}$ torr. The deposition rates were 0.5 and 1 A/s for organic materials and aluminum, respectively. The area of the device is 0.04 cm^2. The ZnO nanocrystals were synthesized by a sol-gel process using precursors of zinc acetate and tetramethylammonium hydroxide (TMAH) [69]. The PbSe QDs were synthesized by decomposition of organometallic precursors as reported previously [81]. The PbSe QDs were washed by precipitation and redispersion three times. Subsequently, the original long-chain oleate ligands on the QD surface were exchanged with octylamine, which is a shorter capping group. The surface-exchanged QDs were washed and redispersed in chloroform. All QD and polymer solutions were filtered using a 0.45 μm filter. Luminance-current-voltage (L-I-V) characteristics of the light up-conversion devices were measured using a Keithley 4200 semiconductor characterization system connected to a calibrated Si photodiode for photocurrent measurements. A 150 W ozone-free xenon arc lamp combined with 1.5G air mass filter, which produces the characteristic Class A spectrum, is coupled with the monochromator as an IR light source to produce a monochromatic light in the wavelength range from 200 to 2800 nm.

The devices were not encapsulated, and the measurements were carried out at room temperature under an ambient atmosphere.

6.3. Results and Discussion

Figure 6-2 shows the absorbance spectra of different PbSe QDs in solution. The absorption peak varies from 1150 nm for 3 nm size QDs to 1750 nm for 6 nm size QDs. The absorption spectra of PbSe QD films show similar absorbance spectra of PbSe QDs in solution near the absorption peaks. The absorption coefficient at the peak wavelengths of PbSe QD films used in this study is about of $2.5X10^4$ cm^{-1}. As-synthesized PbSe QDs have poor carrier transporting properties due to the insulating nature of the long oleic acid capping group. To use PbSe QDs in the up-conversion devices, the oleic acid capping group needs to be replaced by a shorter capping group. Recently, we have demonstrated that the carrier transporting properties can be significantly enhanced if the long capping group is replaced by a shorter benzenedithiol (BDT) group which is done by chemically treating the PbSe films in BDT, as illustrated in Figure 6-1 [80, 81]. In this work, BDT treatment was used in all PbSe QDs films to fabricate the devices.

The control up-conversion devices as shown in Figure 6-3A are basically conventional OLEDs with a PbSe QDs IR sensitizing layer. For an OLED functioning as an up-conversion device, the key is to keep the device off when there is no NIR irradiation. To keep the device off when it is not under NIR irradiation, hole injection from the ITO anode should be suppressed under forward bias. In an OLED with a PbSe sensitizing layer under forward bias, holes are readily injected into the device from the ITO electrode through the PbSe layer. These injected holes turn on the OLED without incident NIR light. Figure 6-3B shows the luminance-current-voltage (L-I-V)

characteristics of the PbSe QD up-conversion device with and without IR illumination. Since hole injection from ITO anode was not suppressed effectively, almost no difference in current densities and luminances was observed. It indicates that the device without the ZnO layer does not demonstrate any up-conversion effects.

To keep the device off while the device is under forward bias, our strategy is to block hole injection from the ITO anode. Here, we used colloidal ZnO nanoparticles to form a hole-blocking layer (HBL) between the ITO anode and the PbSe layer. The ZnO HBL blocks hole injection from the ITO anode under forward bias due to its large band gap (3.4 eV) and deep valence band edge (7.6 eV). Upon photoexcitation, the photogenerated holes in the PbSe NIR sensitizing layer are injected through the HTL and into the emitting layer of the OLED and recombine with electrons injected from the cathode to give off visible light as illustrated in Figure 6-4C.

Figure 6-4B shows the dark L-I-V characteristics of the PbSe QD up-conversion devices with and without the ZnO HBL. The dark current densities of the up-conversion device with the ZnO HBL under forward bias are roughly 2 orders of magnitude lower than that of the device without the ZnO HBL, as shown in Figure 6-3B. These data show that the ZnO layer blocks hole injection from the ITO anode effectively. Low dark current densities are important because they contribute to noise in an up-conversion device. In the absence of IR excitation, the devices without the ZnO HBL behave like normal OLEDs with a high turn-on voltage. The luminance turn-on voltage of the device in the dark is 6 V. The PbSe QD layer increases the turn-on voltage of the device, but it is not sufficient to keep the device off under a strong bias.

On the other hand, the L-V characteristics of the device with the ZnO HBL are measured under different incident NIR illuminations with different power densities at different wavelengths, as shown in Figure 6-4D. Without IR excitation, there is no light emission at voltages up to 17 V, indicating that the ZnO HBL blocks hole injection from the ITO electrode effectively. Upon excitation with IR light, the device turned on at voltages between 7 and 8 V along with an onset of green light emission, and the luminance increases with increasing voltage, saturating at high voltages. Under IR illumination, the current through the device is basically limited by injection of photogenerated holes. As the device is illuminated with IR light, photogenerated holes are injected into the OLED resulting in light emission and the number of photogenerated holes depends on the power density of the incident NIR light. The saturation in luminance is due to the maximum hole generation at a given illumination power density. Increasing the illumination power density increases the luminance output of the device. Excitation at 1.5 μm gives the lowest luminance because of the low absorption coefficient of PbSe QDs at this wavelength and the irradiation at 1.3 μm wavelength gives the highest photoresponse because of the absorption maximum. We should also note that the saturation voltage increases with increasing photoresponse of the device. Since the absorption maximum of the PbSe nanocrystals is at 1.3 μm, the photogenerated hole density is the highest resulting in a higher saturation voltage and a higher luminance maximum. As the illumination wavelength deviates from the maximum, both the saturation voltages and the luminance maxima decrease. These data further confirm that increasing the photogenerated hole density requires higher fields for injection and transport.

The photoresponse is linear over 2 orders of magnitudes of power intensities, shown in Figure 6-5. The IR-to-visible photon-to-photon conversion efficiency (η_{con}) can be calculated by using the equation,

$$\eta_{con}(\%) = \frac{\int \frac{I(\lambda)}{R(\lambda)hc/\lambda} d\lambda}{\frac{P_{IR}}{hc/\lambda}} \times 100$$

where h is Planck's constant, c is the speed of light, λ is the wavelength of the emitted light, I(λ) is the photocurrent measured by the photodetector used for the measurements, R(λ) is the responsivity of the photodetector, λ_{IR} is the wavelength of the incident infrared light, and P_{IR} is the incident infrared power.

Figure 6-6A and B show the overall photon-to-photon (P-P) conversion efficiency at 1.3 μm IR illumination until the voltage reached 17 V. At voltages beyond 17 V, hole injection is due to photogenerated hole injection and dark hole injection from ITO anode through ZnO HBL. The maximum photon-to-photon conversion efficiency is 1.3 % at 17 V as shown in Figure 6-6. P-P conversion efficiency has a strong bias dependence due to efficient P-E conversion in the PbSe NIR sensitizing layer. At low bias like 10 V, shown in Figure 6-6A, green emission is limited by electron injection as photogenerated hole injection from QD layer is sufficient. However, as the voltage increased, shown in Figure 6-6B, P-P conversion efficiency starts to saturate as the amount of electron injection is balanced with hole injection.

Both the photon-to-electron (P-E) and electron-to-photon (E-P) conversion efficiencies are shown in Figure 6-6C. Here, the device dark current has been subtracted to calculate the P-E conversion efficiency. As shown in Figure 6-6C, the P-E efficiency increases sublinearly with increasing voltage. The increase of the P-E

conversion efficiency under low bias (<13 V) is due to increase of injection rate of photogenerated holes into the light emitting layer, and the more rapid increase of the P-E conversion efficiency under higher bias (>16 V) is due to photoconductive gain [82, 83]. On the other hand, the E-P conversion efficiency increases with increasing voltage initially, becomes saturated at voltages between 13.5 and 15.5 V, and finally decreases with increasing voltage. The initial increase in the E-P efficiency with voltage is due to the increase in electron injection and improvement in charge balance, resulting in higher quantum efficiency in light emission. At high voltages, while the injection of photogenerated holes becomes saturated, more electrons are injected from the cathode at higher voltages, resulting in a more charge-imbalanced device and hence a lower E-P conversion efficiency.

Figure 6-7 shows the spectral P-P conversion efficiency as a function of applied voltages. The P-P conversion efficiency spectra are similar to the absorption spectrum of PbSe film as shown in Figure 6-2. The peak wavelength in conversion efficiency spectra is 1.3 μm and the maximum P-P conversion efficiency at the peak wavelength is 1.3 % at 17 V. The low P-P conversion efficiency is due to low absorption coefficients of the PbSe QD film. The absorption coefficient at the peak wavelength of 1.3 μm is $2.4X10^4$ cm^{-1} as shown in Figure 6-2, and the penetration depth of the 1.3 μm NIR light is calculated to 417 nm, indicating that the 50 nm thick PbSe QD film used in this device is not thick enough to absorb all the NIR photons. Further optimization with thicker PbSe QD film and better carrier transporting properties between QDs is expected to improve the photon-to-photon efficiency. Figure 6-8 shows the images of the up-conversion

device at 15 V with and without 1.3 μm NIR illumination. The switching effect of green light emitting by NIR light irradiation was clearly observed.

6.4. Summary

In summary, we have demonstrated low-cost hybrid up-conversion devices with infrared sensitivity to 1.5 μm by incorporating a colloidal PbSe QD NIR sensitizing layer with green phosphorescent OLEDs. To keep the device off in the absence of IR excitation, a ZnO nanocrystal hole blocking layer is incorporated in the OLEDs. The maximum photon-to-photon conversion efficiency of an optimized device at peak wavelength of 1.3 μm is 1.3 %.

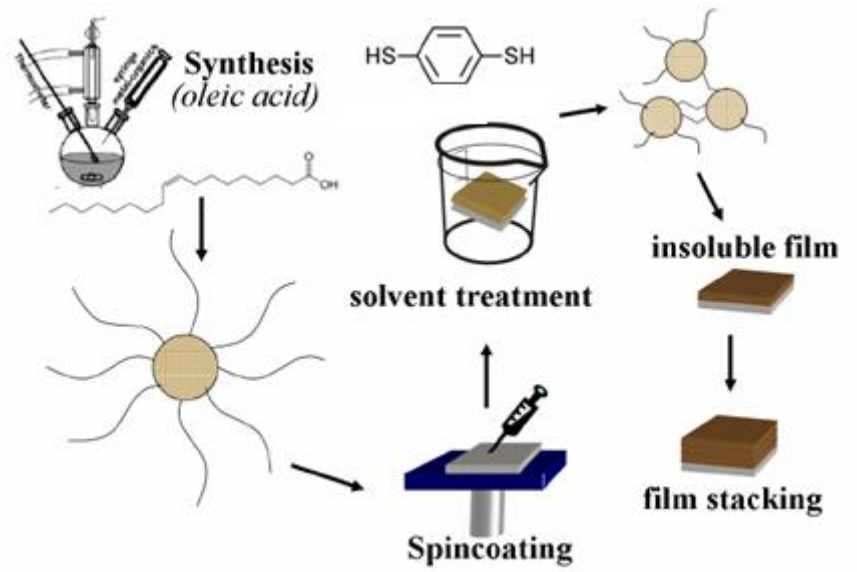

Figure 6-1. Schematic drawing of the process of BDT treatment on QD films. (Adapted from [81])

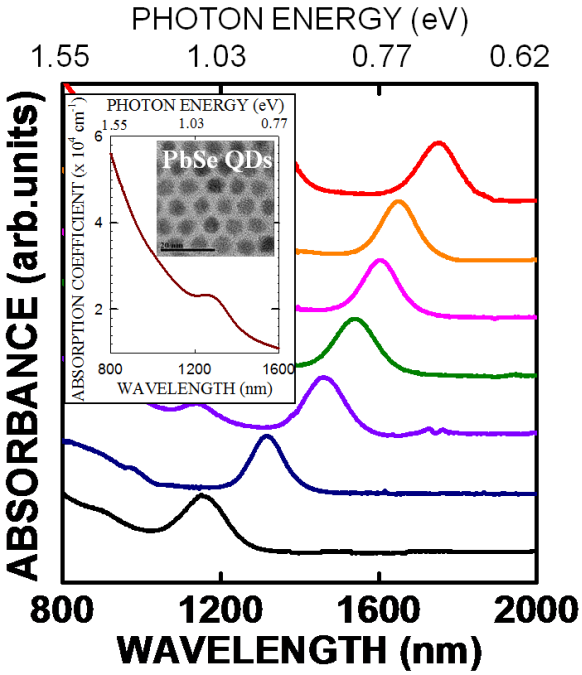

Figure 6-2. Absorption spectra of PbSe QDs with various sizes. (Inset: Absorption coefficient spectrum and TEM image of 50 nm thick PbSe QD film with 1.3 μm peak wavelength)

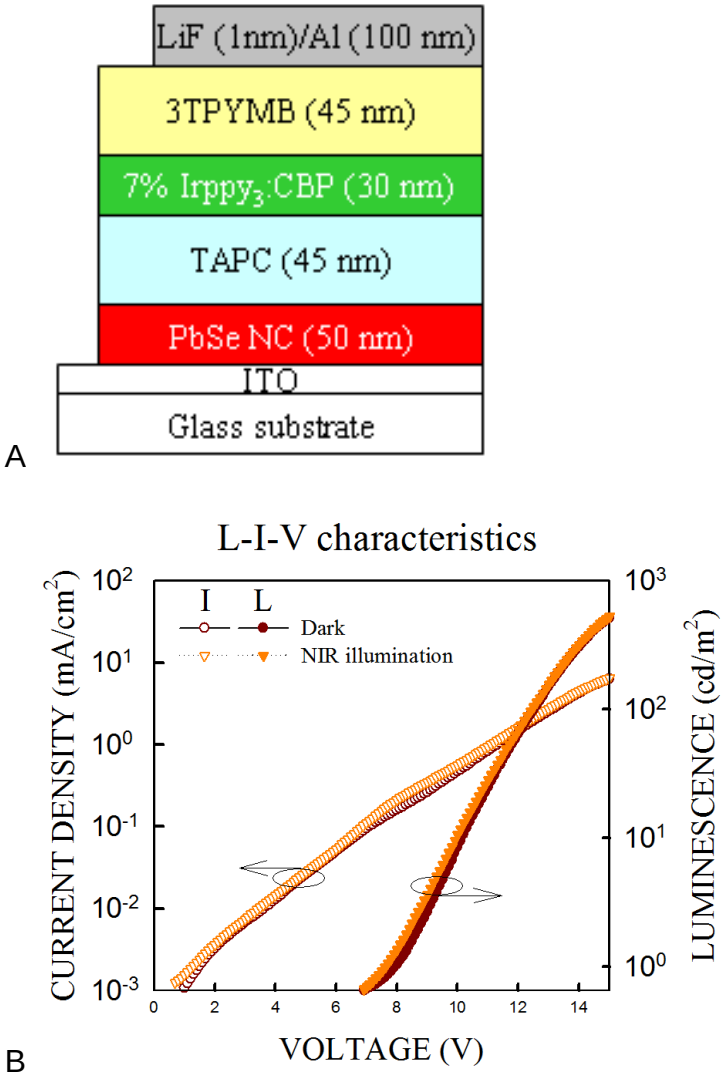

Figure 6-3. Device structure and L-I-V characteristics of PbSe QD up-conversion device without a hole blocking layer: A) schematic diagram of a PbSe QD infrared-to-green up-conversion device, B) current density and luminance plots under dark and with IR illumination as a function of voltage.

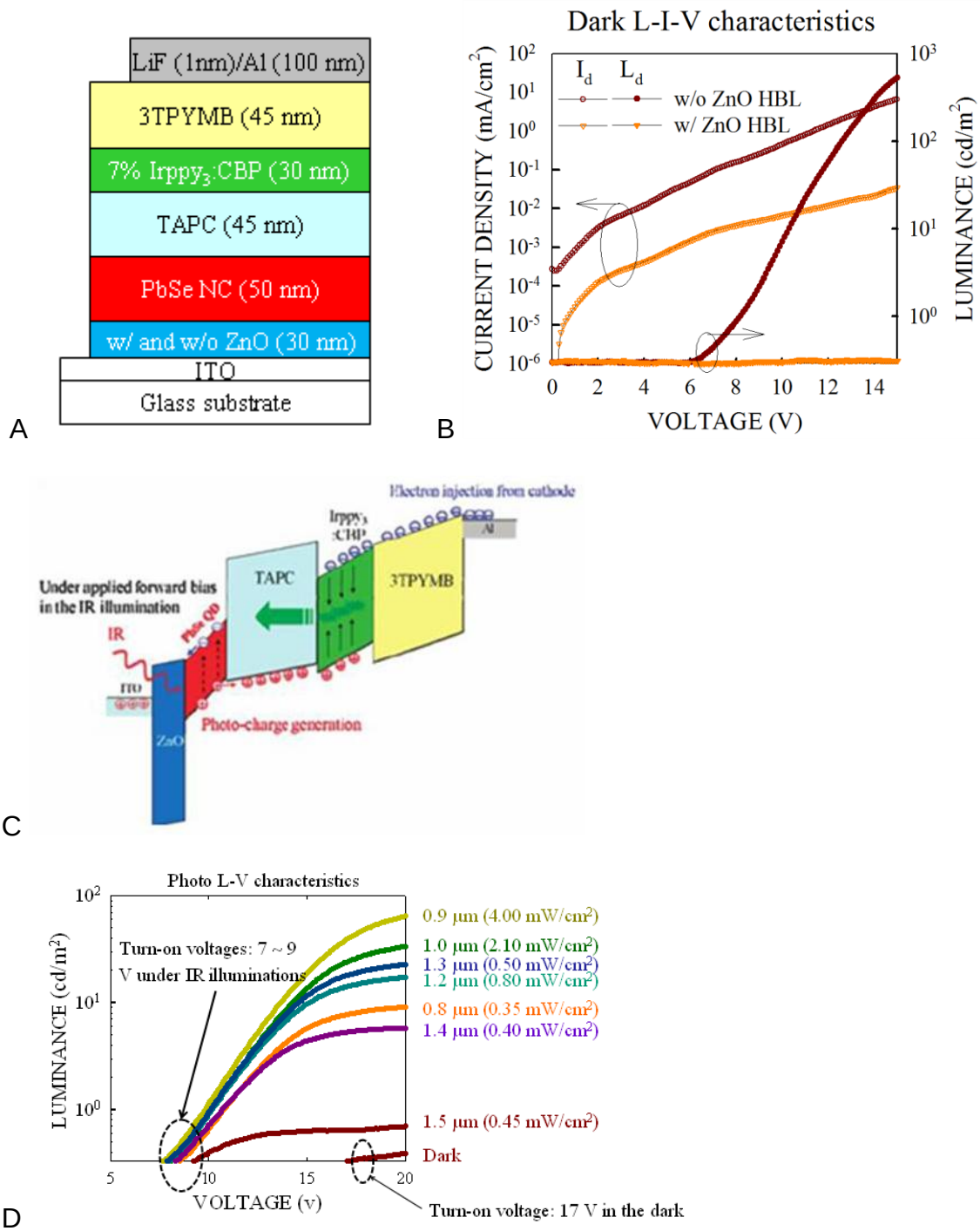

Figure 6-4. Device structure and L-I-V characteristics of PbSe QD up-conversion device with a hole blocking layer: A) schematic diagram of the up-conversion device with and without ZnO hole blocking layer, B) current density and luminance plots under dark as a function of voltage, C) schematic energy band diagram of the up-conversion device with hole blocking layer operating in IR illumination, and D) luminance plots under IR illumination with various wavelengths.

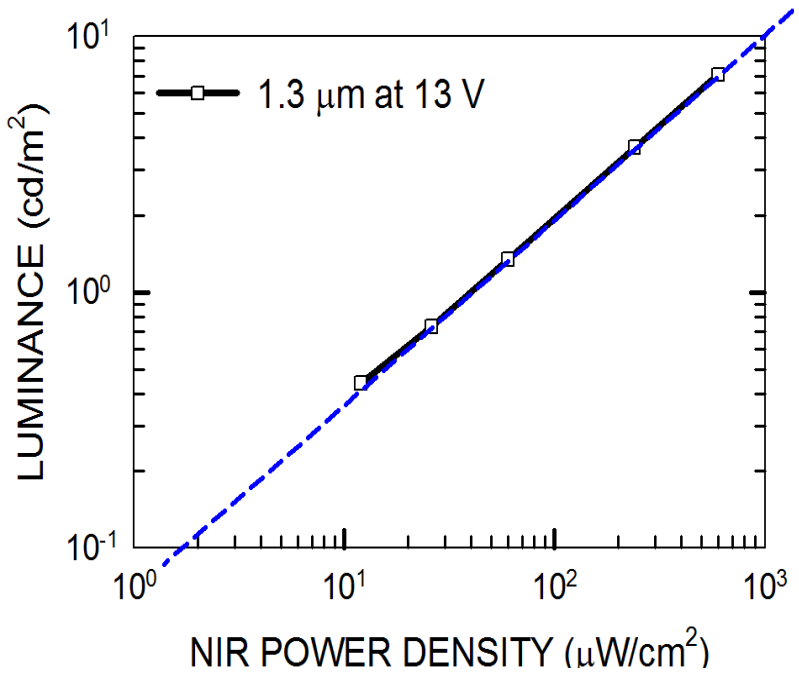

Figure 6-5. Luminance at 13 V with a linear dependence on the NIR power densities.

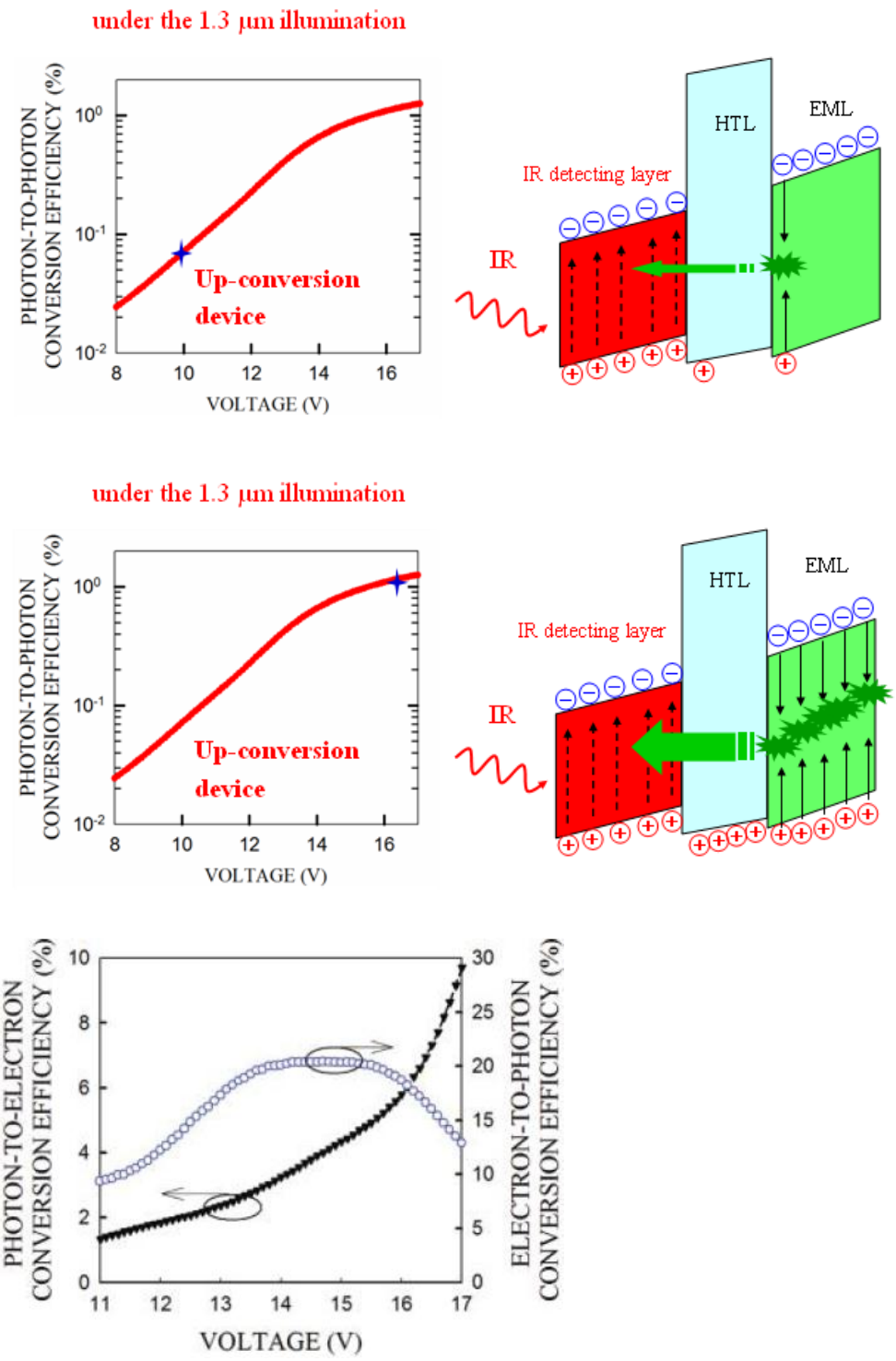

Figure 6-6. P-P conversion efficiency as a function of voltage with schematic drawing of up-conversion operation and P-E and E-P conversion efficiencies: photon-to-photon conversion efficiency at A) 10 V and B) 16 V, and C) photon-to-electron and electron-to-photon conversion efficiencies as a function of voltage.

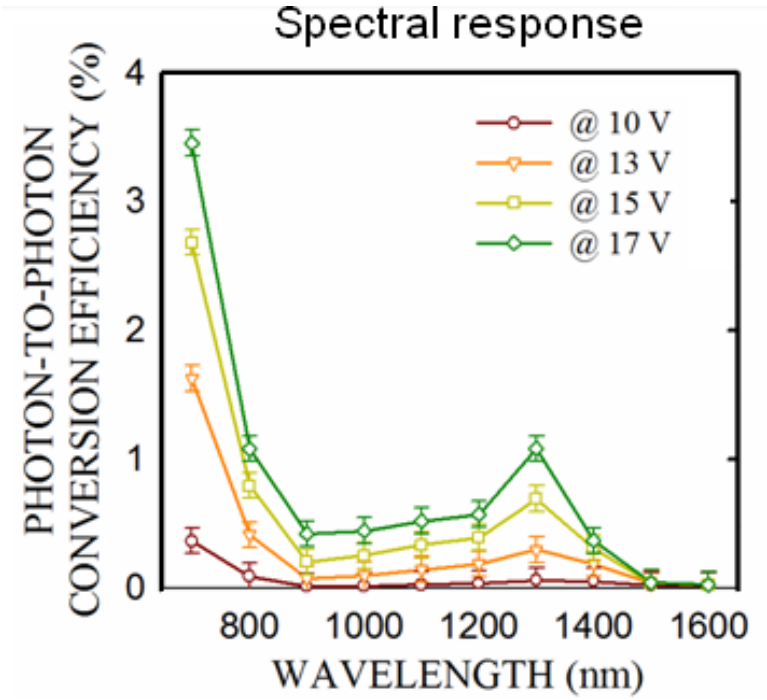

Figure 6-7. Spectral photon-to-photon conversion efficiency of PbSe QD up-conversion device as a function of wavelength under different applied voltages.

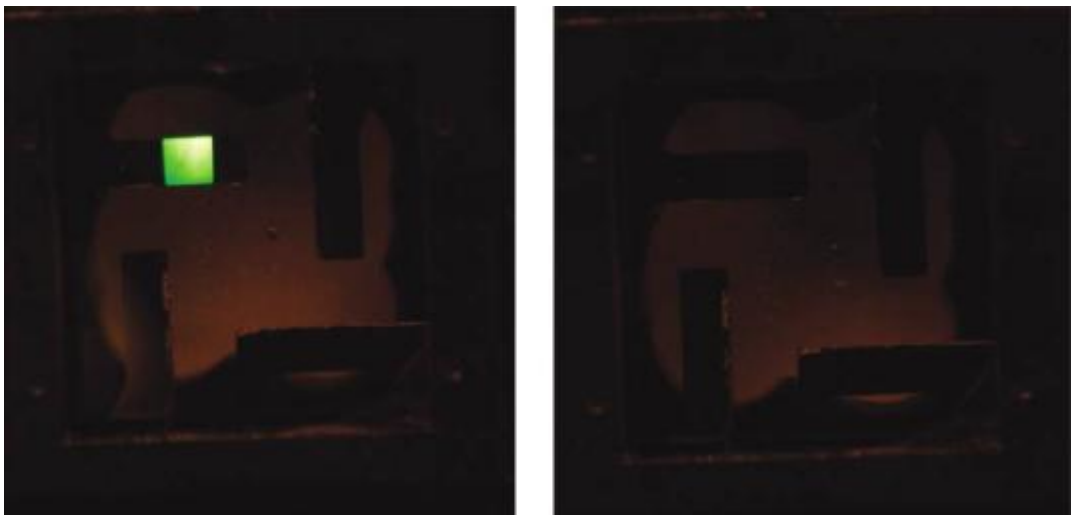

Figure 6-8. Images of an up-conversion device with (left) and without (right) 1.3 mm NIR illumination under 15 V.

CHAPTER 7
CONCLUSION

This dissertation has focused on studying the white and green stacked organic light-emitting diodes, colloidal quantum dot based hybrid infrared light-emitting devices and infrared-to-green organic and hybrid up-conversion devices.

In the study of organic light-emitting diodes, first, we study on the emission mechanism in white OLEDs. We fabricated double, triple, and quadruple emissive layer WOLEDs, focusing the color balance by controlling the doping concentrations and the distance between the emissive layer and main exciton generation interface. The emission mechanism in WOLEDs was studied from simple EL measurements with changing device configurations. In the triple emissive layer white OLEDs, we found that red emission is attributed to direct exciton generation from hole trapping on the red dopant and electron transporting through Firpic in mCP, and green emission is attributed to energy transfer from TPBi host to $Ir(ppy)_3$ guest. The understanding of the emission mechanism helps us to design efficient WOLEDs with the peak power efficiency of 30 lm/W and high CRI of 82.5.

We also investigated the charge generation mechanism in stacked OLEDs. For the first part, we found that overall current generated from the charge generation units is significantly dependent on the electron flow through steep energy barrier of n-doped ETL, which is affected by doping concentration, if efficient electron accepting materials are used. For the second part, we fabricated green phosphorescent stacked OLEDs, and found that efficient electron accepting materials and trap-free hole transporting materials like NPB are needed to obtain effective charge generation.

In the study of hybrid light-emitting devices, we demonstrated hybrid infrared LEDs based on PbSe colloidal quantum dots and MEH-PPV polymer. Through the study and optimization of the devices, we obtained the maximum external quantum efficiency of 0.83 % at the peak wavelength of 1280 nm. This work exhibited a significant enhancement in device efficiencies compared to previously reported QD based IR LEDs. However, further improvement is expected with the optimization of materials and device architecture.

In the study of organic up-conversion devices, we demonstrated NIR-to-green organic up-conversion devices with various hole blocking structures. Both to thicken IR sensitizing layer and to insert hole blocking layer enabled the enhanced on/off characteristics due to the suppression of hole injection from the anode. The maximum operating photon-to-photon conversion efficiency is 2.54 %.

In the study of hybrid up-conversion devices, we have demonstrated low-cost hybrid up-conversion devices with infrared sensitivity to 1.5 μm by incorporating a colloidal PbSe nanocrystal NIR sensitizing layer with green phosphorescent OLEDs. To keep the device off in the absence of IR excitation, a ZnO nanocrystal hole blocking layer is incorporated in the OLEDs. The maximum photon-to-photon conversion efficiency of an optimized device at peak wavelength of 1.3 μm is 1.3 %.

APPENDIX
MOLECULAR STRUCTURES OF ORGANIC MATERIALS USED IN THIS DISSERTATION

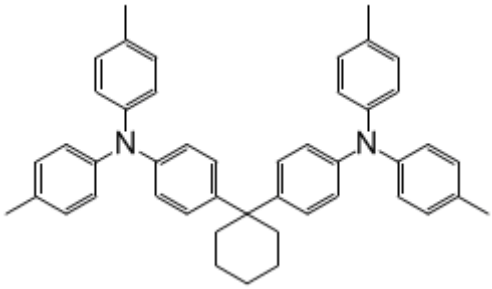

TAPC

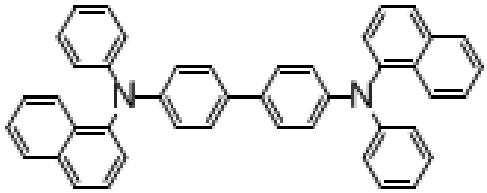

NPB

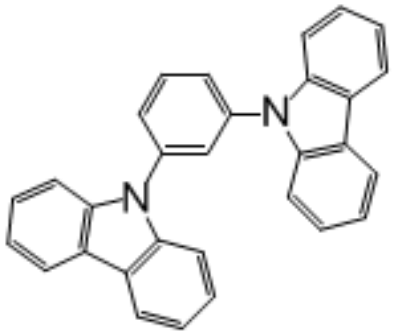

mCP

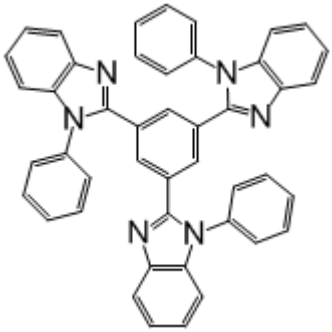

TPBi

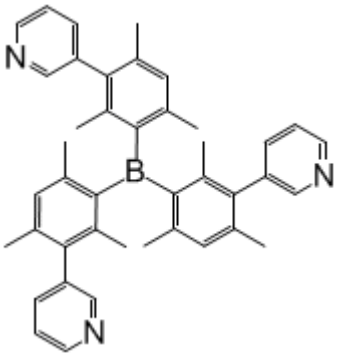

3TPYMB

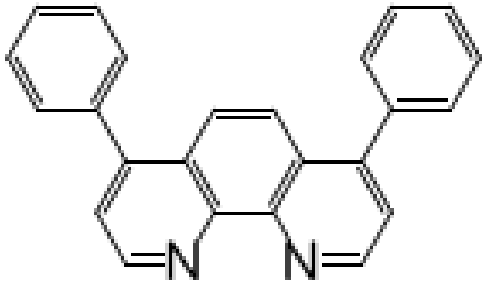

BPhen

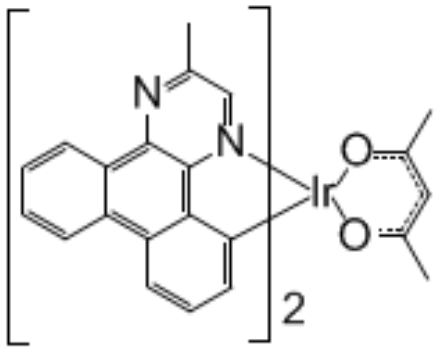

$Ir(MDQ)_2(acac)$

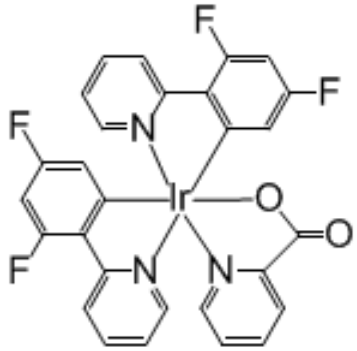

Firpic

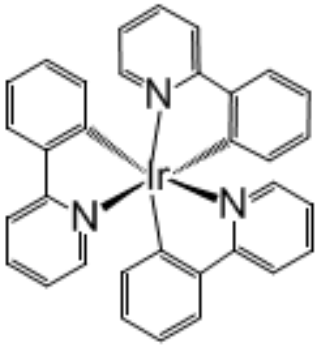

$Ir(ppy)_3$

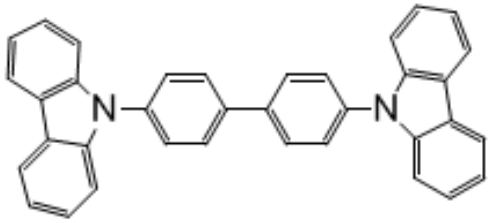

CBP

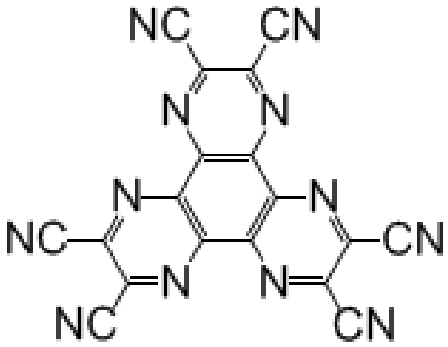

HAT-CN

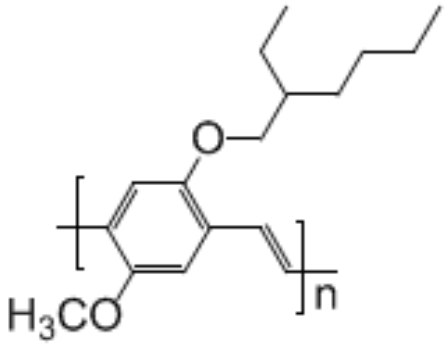

MEH-PPV

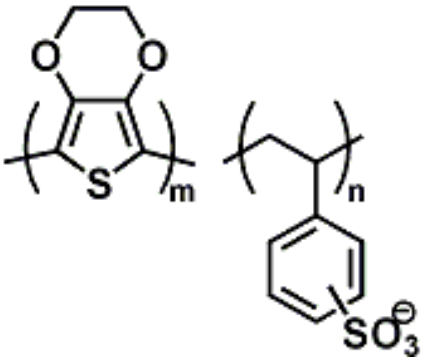

PEDOT:PSS

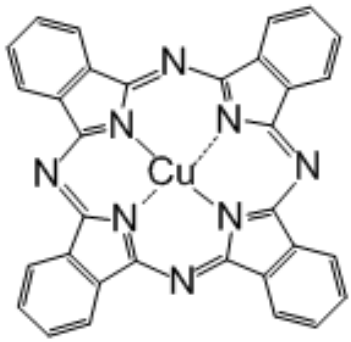

CuPc

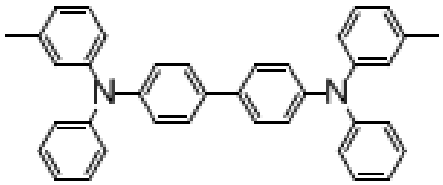

TPD

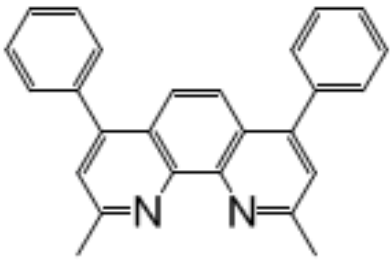

BCP

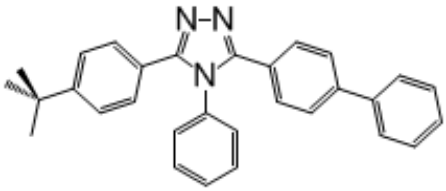

TAZ

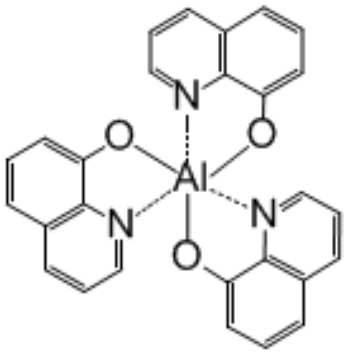

Alq_3

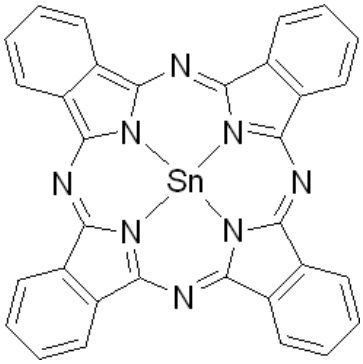

SnPc

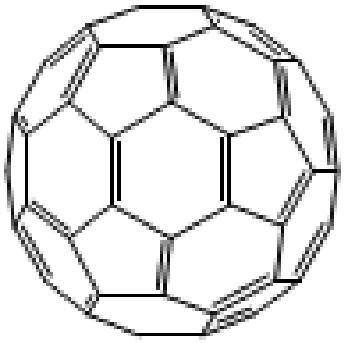

C_{60}

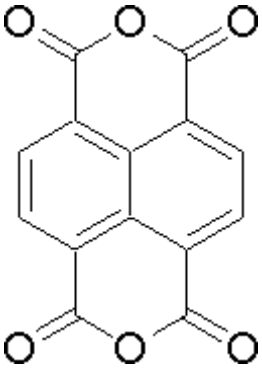

NTCDA

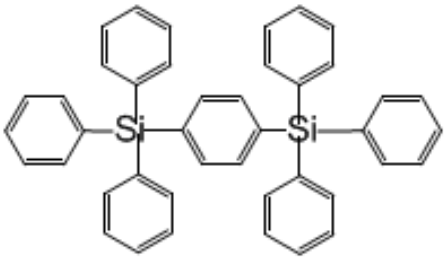

UGH2

LIST OF REFERENCES

[1] C. W. Tang and S. A. VanSlyke, Appl. Phys. Lett. 51 (1987) 913.

[2] DisplaySearch, www.displaysearch.com.

[3] U.S. Department of Energy, “Volume 1: National Lighting Inventory and Energy Consumption Estimate” (2002).

[4] M. C. Gather, A. Kohnen and K. Meerholz, Adv. Mater. 23 (2011) 233.

[5] J. Kido, K. Hongawa, K. Okuyama and K. Nagai, Appl. Phys. Lett. 64 (1994) 815.

[6] N. Ide, T. Komoda and J. Kido, Proc. SPIE-Int. Soc. Opt. Eng. 6333 (2006) 63330M.

[7] B. W. D’Andrade, J. Esler, C. Lin, V. Adamovich, S. Xia, M. S. Weaver, R. Kwong and J. J. Brown, Proc. SPIE-Int. Soc. Opt. Eng. 7051 (2008) 70510Q.

[8] S. Reineke, F. Lindner, G. Schwartz, N. Seidler, K. Walzer, B. Lussern and K. Leo, Nature 459 (2009) 234.

[9] E. F. Schubert, “Light-Emitting Diodes” (2003).

[10] V. L. Colvin, M. C. Schlamp and A. P. Alivisatos, Nature 370 (1994) 354.

[11] H. Mattoussi, L. H. Radzilowski, B. O. Dabbousi, E. L. Thomas, M. G. Bawendi and M. F. Rubner, J. Appl. Phys. 83 (1998) 7965.

[12] S. Coe-Sullivan, W.-K. Woo, M. Bawendi and V. Bulovic, Nature 420 (2002) 800.

[13] Q. Sun, Y. A. Wang, L. S. Li, D. Wang, T. Zhu, J. Xu, C. Yang and Y. Li, Nat. Photon. 1 (2007) 717.

[14] P. O. Anikeeva, J. E. Halpert, M. G. Bawendi and V. Bulovic, Nano Lett. 7 (2007) 2196.

[15] N. Tessler, V. Medvedev, M. Kazes, S. H. Kan and U. Vanin, Science 295 (2002) 1506.

[16] D. S. Koktysh, N. Gaponik, M. Reufer, J. Crewett, U. Scherf, A. Eychmuller, J. M. Lupton, A. L. Rogach and J. Feldmann, ChemPhysChem 5 (2004) 1435.

[17] J. S. Steckel, S. Coe-Sullivan, V. Bulovic and M. G. Bawendi, Adv. Mater. 15 (2003) 1862.

[18] C. B. Murray, C. R. Kagan and M. G. Bawendi, Annu. Rev. Mater. Sci. 30 (2000) 545.

[19] V. K. La Mer, and R. H. Dinegar, J. Am. Chem. Soc. 72 (1950) 4847.

[20] P. Peumans, V. Bulovic and S. Forrest, Appl. Phys. Lett. 76 (2000) 3855.

[21] J. Xue and S. Forrest, J. Appl. Phys. 95 (2004) 1869.

[22] J. Y. Kim, N. E. Coates, D. Moses, T. Nguyen, M. Dante, K. Lee and A. J. Heeger, Science 317 (2007) 222.

[23] X. Gong, M. H. Tong, Y. J. Xia, W. Z. Cai, J. S. Moon, Y. Cao, G. Yu, C. L. Shieh, B. Nilsson and A. J. Heeger, Science 325 (2009) 1665.

[24] J. D. Zimmerman, E. K. Yu, V. V. Diev, K. Hanson, M. E. Thompson and S. R. Forrest, Org. Electron. 12 (2011) 869.

[25] G. Konstantatos, I. Howard, A. Fischer, S. Hoogland, J. Clifford, E. Klem, L. Levina and E. H. Sargent, Nature 442 (2006) 180.

[26] G. Konstantatos and E. H. Sargent, Appl. Phys. Lett. 91 (2007) 173505.

[27] G. Konstantatos, L. Levina, A. Fischer and E. H. Sargent, Nano Lett. 8 (2008) 1446.

[28] J. D. K. Ethan, S. Harnik, H. Sean, D. M. Dean, L. Larissa and H. S. Edward, Appl. Phys. Lett. 92 (2008) 212105.

[29] J. P. Clifford, G. Konstantatos, K. W. Johnston, S. Hoogland, L. Levina and E. H. Sargent, Nat. Nanotechnol. 4 (2009) 40.

[30] E. H. Sargent, Adv. Mater. 20 (2008) 3958.

[31] K. Szendrei, F. Cordella, M. V. Kovalenko, M. Boberl, G. Hesser, M. Yorema, D. Jarzab, O. V. Mikhnenko, A. Gocalinska, M. Saba, F. Quochi, A. Mura, G. Bongiovanni, P. W. M. Blom, W. G. Heiss and M. A. Loi, Adv. Mater. 21 (2009) 683.

[32] K. R. Choudhury, Y. Sahoo, T. Y. Ohulchanskyy and P. N. Prasad, Appl. Phys. Lett. 87 (2005) 073110.

[33] S. A. McDonald, P. W. Cyr, L. Levina and E. H. Sargent, Appl. Phys. Lett. 85 (2004) 2089.

[34] B. E. A. Saleh and M. C. Teich, “Fundamental of Photonics” (1991).

[35] Q. Wang, J. Ding, D. Ma, Y. Cheng, L. Wang, X. Jing and F. Wang, Adv. Funct. Mater. 19 (2009) 84.

[36] T. Matsumoto, T. Nakada, J. Endo, K. Mori, N. Kavamura, A. Yokoi and J. Kido, “Society for Information Display International Symposium Digest of Technical Papers”, (2003).

[37] L. S. Liao, K. P. Klubek and C. W. Tang, Appl. Phys. Lett. 84 (2004) 167.

[38] T.-Y. Cho, C.-L. Lin and C.-C. Wu, Appl. Phys. Lett. 88 (2006) 111106.

[39] M. K. Fung, K. M. Lau, S. L. Lai, C. W. Law, M. Y. Chan, C. S. Lee and S. T. Lee, J. Appl. Phys. 104 (2008) 034509.

[40] X. D. Gao, J. Zhou, Z. T. Xie, B. F. Ding, Y. C. Qian, X. M. Ding and X. Y. Hou, Appl. Phys. Lett. 93 (2008) 083304.

[41] C.-W. Chen, Y.-J. Lu, C.-C. Wu, E. H.-E. Wu, C.-W. Chu and Y. Yang, Appl. Phys. Lett. 87 (2005) 241121.

[42] M.-Y. Chan, S.-L. Lai, K.-M. Lau, M.-K. Fung, C.-S. Lee and S.-T. Lee, Adv. Funct. Mater. 17 (2007) 2509.

[43] F. Wei and L. Fang, J. Mater.Sci: Mater. Electron. 19 (2008) 1202.

[44] L. S. Liao and K. P. Klubek, Appl. Phys. Lett. 92 (2008) 223311.

[45] L.-S. Liao, W. K. Slusalek, T. K Hatwar, M. L. Ricks and D. L. Comfort, Adv. Mater. 20 (2008) 324.

[46] T. Tsutsui and M. Terai, Appl. Phys. Lett. 84 (2004) 440.

[47] J. Meyer, M. Kroger, S. Hamwi, F. Gnam, T. Riedl, W. Kowalsky and A. Kahn, Appl. Phys. Lett. 96 (2010) 193302.

[48] S. Hamwi, J. Meyer, M. Kroger, T. Winkler, M. Witte, T. Riedl, A. Kahn and W. Kowalsky, Adv. Funct. Mater. 20 (2010) 1762.

[49] Y. Cai, H. X. Wei, J. Li, Q. Y. Bao, X. Zhao, S. T. Lee, Y. Q. Li and J. X. Tang, Appl. Phys. Lett. 98 (2011) 113304.

[50] F. So, “Organic Electronics: Materials, Processing, Devices and Applications” (2010).

[51] K. R. Choudhury, D. W. Song and F. So, Org. Electron. 11 (2010) 23.

[52] J. S. Steckel, B. K. H. Yen, D. C. Oertel and M. G. Bawendi, J. Am. Chem. Soc. 128 (2006) 13032.

[53] S. Coe-Sullivan, J. S. Steckel, W.-K. Woo, M. G. Bawendi and V. Bulovic, Adv. Funct. Mater. 15 (2005) 1117.

[54] C. A. Leatherdale, C. R. Kagan, N. Y. Morgan, S. A. Empedocles, M. A. Kastner and M. Bawendi, Phys. Rev. B 62 (2000) 2699.

[55] G. Konstantatos, C. Huang, L. Levina, Z. Lu and E. H. Sargent, Adv. Funct. Mater. 15 (2005) 1865.

[56] K. Tada and M. Onoda, Jpn. J. Appl. Phys. 44 (2005) 4165.

[57] Y. Xu, X. Zhang, J. Peng, Q. Niu and Y. Cao, Semicond. Sci. Technol. 21 (2006) 1373.

[58] A. Badia, L. Cuccia, L. Demers, F. Morin and R. B. Lennox, J. Am. Chem. Soc. 119 (1997) 2682.

[59] T. F. Chang, S. Musikhin, L. Bakueva, L. Levina, M. A. Hines, P. A. Cyr and E. H. Sargent, Appl. Phys. Lett. 84 (1997) 4295.

[60] K. J. Russell, I. Appelbaum, H. Temkin, C. H. Perry, V. Narayanamurti, M. P. Hanson and A. C. Gossard, Appl. Phys. Lett. 82 (2003) 2960.

[61] J. S. Sandhu, A. P. Heberle, B. W. Alphenaar and J. R. A. Cleaver, Appl. Phys. Lett. 76 (2000) 1507.

[62] H. C. Liu, M. Gao and P. J. Poole, Electron. Lett. 36 (2000) 1300.

[63] Y. Yang, W. Z. Shen, H. C. Liu, S. R. Laframboise, S. Wicaksono, S. F. Yoon and K. H. Tan, Appl. Phys. Lett. 94 (2009) 093504.

[64] D. Ban, S. Han, Z. H. Luo, T. Oogarah, A. J. SpringThorpe and H. C. Liu, Appl. Phys. Lett. 90 (2007) 093108.

[65] J. Ni, T. Tano, Y. Ichino, T. Hanada, T. Kamata, N. Takada and K. Yase, Jpn. J. Appl. Phys. 40 (2001) L948.

[66] M. Chikamatsu, Y. Ichino, N. Takada, M. Yoshida, T. Kamata and K. Yase, Appl. Phys. Lett. 81 (2002) 769.

[67] D. Y. Kim, D. W. Song, N. Chopra, P. D. Somer and F. So, Adv. Mater. 22 (2010) 2260.

[68] R. A. Laudise, C. Kloc, P. G. Simpkins and T. Siegrist, J. Cryst. Growth 187 (1998) 449.

[69] G. Sarasqueta, K. R. Choudhury, J. Subbiah and F. So, Adv. Func. Mater. 21 (2011) 167.

[70] B. P. Rand, J. Xue, F. Yang and S. R. Forrest, Appl. Phys. Lett. 87 (2005) 233508.

[71] Y. Kijima, N. Asai and S. Tamura, Jpn. J. Appl. Phys. 38 (1999) 5274.

[72] R. J. Holmes, B. W. D'Andrade, S. R. Forrest, X. Ren, J. Li and M. E. Thompson, Appl. Phys. Lett. 83 (2003) 3818.

[73] F. Verbakel, S. C. J. Meskers and R. A. J. Janssen, Appl. Phys. Lett. 89 (2006) 102103.

[74] S. P. Singh, P. Sonar, A. Sellinger and A. Dodabalapur, Appl. Phys. Lett. 94 (2009) 013308.

[75] K. S. Yook, S. O. Jeon, O. Y. Kim and J. Y. Lee, Electrochem. Solid-State. Lett. 14 (2011) B59.

[76] J-J. Lin, W.-S. Liao, H.-J. Huang, F-I. Wu and C.-H. Cheng, Adv. Funct. Mater. 18 (2008) 485.

[77] D. Y. Kim, K. R. Choudhury, J. W. Lee, D. W. Song, G. Sarasqueta and F. So, Nano Lett. 11 (2011) 2109.

[78] V. Sukhovatkin, S. Musikhin, I. Gorelikov, S. Cauchi, L. Bakueva, E. Kumacheva and E. H. Sargent, Opt. Lett. 30 (2005) 171.

[79] E. H. Sargent, Nat. Photonics 3 (2009) 325.

[80] G. Sarasqueta, K. R. Choudhury and F. So, Chem. Mater. 22 (2010) 3496.

[81] G. Sarasqueta, K. R. Choudhury, J. Subbiah and F. So, Adv. Funct. Mater. 21 (2010) 167.

[82] M. Hiramoto, T. Imahigashi and M. Yokohama, Appl. Phys. Lett. 64 (1993) 187.

[83] H. Chen, M. K. F. Lo, G. Yang, H. G. Monbouquette and Y. Yang, Nat. Nanotechnol. 3 (2008) 543.

BIOGRAPHICAL SKETCH

Dong Woo Song was born in Seoul, Republic of Korea. Since he wanted to be a person who contributes his talent to society, he decided to become a scientist and received intensified education for a variety of science fields at Seoul Science High School. He majored in Materials Science and Engineering for his B.S. degree (1997-2004) and M.S. degree (2004-2006) with a specialty in III-nitrides epitaxial growth for light-emitting diode (LED) applications at Seoul National University.

After graduation with the M.S. degree, he joined the Department of Materials Science and Engineering at University of Florida, and completed his Ph.D. dissertation on organic light-emitting diodes (OLEDs) and related hybrid light-emitting devices in 2011.